AWARD NUMBER: **W81XWH-14-1-0358**

TITLE: **Musculoskeletal Complications and Bone Metastases in Breast Cancer Patients Undergoing Estrogen Deprivation Therapy**

PRINCIPAL INVESTIGATOR: **Laura E. Wright, Ph.D.**

CONTRACTING ORGANIZATION: **Indiana University**
Indianapolis, IN 46202

REPORT DATE: **October 2015**

TYPE OF REPORT: **Annual**

PREPARED FOR: **U.S. Army Medical Research and Materiel Command**
Fort Detrick, Maryland 21702-5012

REPORT DOCUMENTATION PAGE

Form Approved
OMB No. 0704-0188

1. REPORT DATE	2. REPORT TYPE	3. DATES COVERED
October 2015	Annual	30 Sep 2014 - 29 Sep 2015

4. TITLE AND SUBTITLE

Musculoskeletal Complications and Bone Metastases in Breast Cancer Patients Undergoing Estrogen Deprivation Therapy

5a. CONTRACT NUMBER

5b. GRANT NUMBER
W81XWH-14-1-0358

5c. PROGRAM ELEMENT NUMBER

6. AUTHOR(S)

Laura E. Wright, Ph.D.

E-Mail: laewrig@iu.edu

5d. PROJECT NUMBER

5e. TASK NUMBER

5f. WORK UNIT NUMBER

7. PERFORMING ORGANIZATION NAME(S) AND ADDRESS(ES)

Indiana University School of Medicine
980 West Walnut Street R3 Room C132
Indianapolis, IN 46202

8. PERFORMING ORGANIZATION REPORT NUMBER

9. SPONSORING / MONITORING AGENCY NAME(S) AND ADDRESS(ES)

U.S. Army Medical Research and Materiel Command
Fort Detrick, Maryland 21702-5012

10. SPONSOR/MONITOR'S ACRONYM(S)

11. SPONSOR/MONITOR'S REPORT NUMBER(S)

12. DISTRIBUTION / AVAILABILITY STATEMENT

Approved for Public Release; Distribution Unlimited

13. SUPPLEMENTARY NOTES

14. ABSTRACT

Adjuvant endocrine therapy using an aromatase inhibitor (AI) is a standard treatment for postmenopausal women with ER-positive breast cancer. Unfortunately, up to 50% of women treated with an AI develop muscle weakness, bone loss and joint pain that result in treatment discontinuation. I hypothesized that estrogen deprivation and subsequent bone loss could alter the bone microenvironment in ways that accelerate the progression of breast cancer growth in bone and exacerbate muscle weakness systemically. Four-week female athymic nude mice underwent OVX or sham surgery and were treated daily with vehicle or AI (10μg/day; n=20/group). Three weeks after surgery and onset of treatment, serum levels of 17β-estradiol in OVX-AI mice were reduced by 56% ($p<0.01$) and trabecular bone volume fraction at the proximal tibia was reduced by 67% relative to vehicle-sham ($p<0.001$). After confirming estrogen deficiency and bone loss, the same animals were inoculated with ER-negative MDA-MB-231 human breast cancer cells into the left cardiac ventricle and followed for cancer progression in bone. Five weeks after inoculation, osteolytic lesion area increased by 110% ($p<0.01$) and tumor burden in bone was increased by 87% in OVX-AI mice relative to sham-vehicle ($p<0.01$). Furthermore, *ex vivo* maximal contractile force of the extensor digitorum longus (EDL) muscle was significantly reduced in OVX-AI mice (-12%, $p<0.001$) relative to sham-vehicle. These studies confirmed that AI treatment induces bone loss and skeletal muscle weakness, recapitulating effects reported in cancer patients. As hypothesized, severe bone loss resulting from AI-induced estrogen depletion may prime the bone microenvironment for the development of breast cancer metastases to bone and potentiate muscle weakness. Ongoing studies will evaluate whether protection of bone with bisphosphonates can prevent AI-induced musculoskeletal complications in my model of breast cancer bone metastases.

15. SUBJECT TERMS

Breast cancer; bone metastases; estrogen; endocrine therapy; aromatase inhibitors; letrozole; selective estrogen receptor modulators; tamoxifen; bone loss; TGFβ; skeletal muscle; ryanodine receptor; myocyte.

16. SECURITY CLASSIFICATION OF:			17. LIMITATION OF ABSTRACT	18. NUMBER OF PAGES	19a. NAME OF RESPONSIBLE PERSON
					USAMRMC
a. REPORT	b. ABSTRACT	c. THIS PAGE	Unclassified	74	19b. TELEPHONE NUMBER *(include area code)*
Unclassified	Unclassified	Unclassified			

TABLE OF CONTENTS

1. INTRODUCTION

Adjuvant endocrine therapy using an aromatase inhibitor (AI), which drastically depletes peripheral 17β-estradiol (E2) concentrations, is a standard treatment for postmenopausal women with estrogen receptor (ER)-positive breast cancer. Unlike selective estrogen receptor modulators (SERMs), which spare bone, AI treatment leads to severe bone loss and musculoskeletal complications that result in low patient compliance for life-prolonging AI therapy. The mechanism of AI-induced muscular dysfunction has not been identified, however, E2-deprivation is characterized by inflammation and release of systemic factors during bone resorption, which together have been demonstrated in other disease models to modify the ryanodine receptor (RyR1), a critical calcium channel required for skeletal muscle contraction. What is more, a state of high bone turnover resulting from AI-induced E2 depletion could alter the bone microenvironment by releasing matrix-derived growth factors (e.g., TGF-β) that prime the pre-metastatic niche and increase breast cancer progression in bone; preliminary data that I have obtained support this postulate. This proposal was therefore designed to evaluate the effects of AI therapy on the musculoskeletal system in the context of breast cancer by determining 1) how AI-induced E2 depletion impairs muscle function, 2) whether AI-induced E2 depletion increases breast cancer bone metastases and 3) the relative contribution of bone loss in each case.

2. KEYWORDS

Breast cancer; bone metastases; estrogen; endocrine therapy; aromatase inhibitors; letrozole; selective estrogen receptor modulators; tamoxifen; bone loss; TGFβ; skeletal muscle; ryanodine receptor; myocyte.

3. ACCOMPLISHMENTS

Major scientific goals

Task 1. *Determine effects of the aromatase inhibitor (AI) letrozole and the selective estrogen receptor modulator (SERM) tamoxifen on skeletal muscle function in vivo.* **[50% complete]**

- **a.** *Complete training in confocal microscopy, micro-dissection, and muscle force measurement in the Marks Laboratory.*
  - **All necessary training for the muscle biochemical analyses and isolated whole muscle contractility has been completed under the supervision of my co-mentor Dr. Andrew Marks and his laboratory personnel at Columbia University. I am now able to perform the muscle physiology measurements necessary to complete the project independently in my laboratory at Indiana University.**

- ***b.*** *Conduct in vivo study comparing effects of OVX alone and with or without AI treatment (letrozole; 5mg/kg/d; i.p., for two months) or SERM treatment (tamoxifen; 50mg/kg/d; i.p., for two months) relative to E2-replete sham-operated animals with endpoints to include serum levels of 17β-estradiol and inflammatory cytokines by Bio-Plex assay, body composition by DXA, grip strength, ex vivo muscle specific force production and fatigability of the extensor digitorum longus (EDL) and soleus muscles.*
  - **As planned, C56Bl/6 mice were ovariectomized (OVX) and followed prospectively for changes in body composition (Figure 1A), bone mineral density (BMD; Figure 1B), grip strength (Figure 1C), and bone volume fraction (BV/TV; Figure 2) and compared to sham-operated E2-replete animals. After eight weeks of ovarian E2 deprivation, I measured *ex vivo* muscle contractility of the extensor digitorum longus (EDL) muscle (Figure 3). In line with my hypothesis, I found that bone loss associated with estrogen deprivation (Figure 1B, Figure 2) was associated with reduced grip strength (Figure 1C), muscle weakness, and increased fatigability in mice (Figure 3). The second phase of this task is ongoing and includes the proposed anti-E2 drugs (AI and SERM). Results will be included in the next reporting period. Once all treatment groups are complete, serum 17β-estradiol and inflammatory cytokines will be assayed at the same time in order to avoid intra-assay variability.**

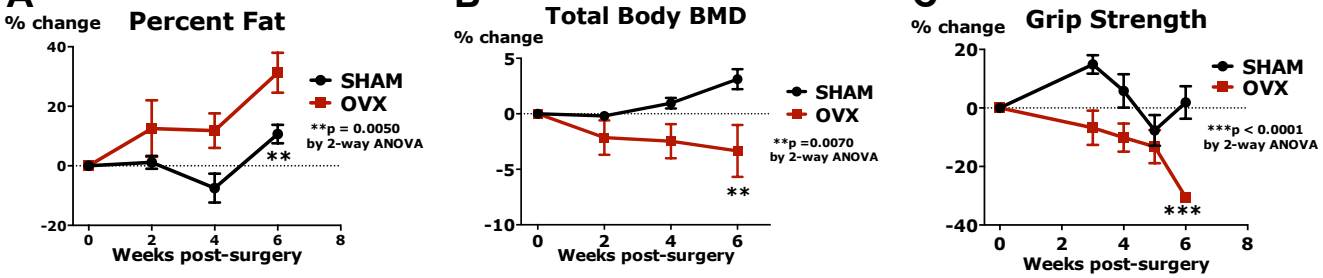

Figure 1. Estrogen deprivation by ovariectomy (OVX) results in **A.** increased body fat percentage as assessed by DXA, **B.** decreased bone mineral density (BMD) as assessed by DXA, and **C.** reduced forelimb grip strength in C57Bl/6 mice.

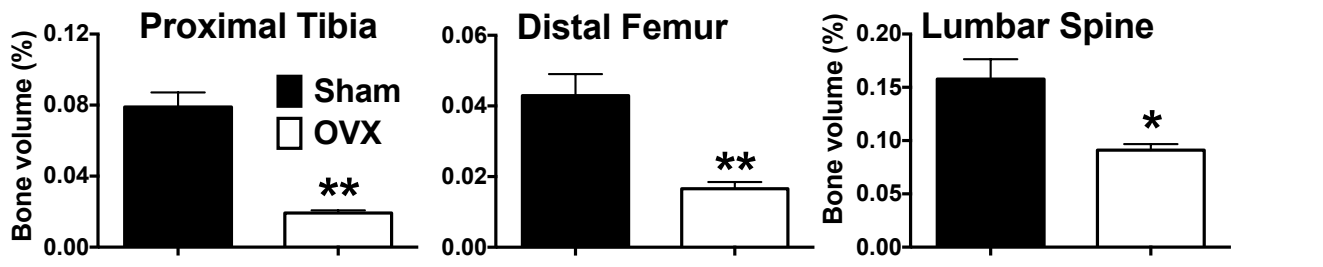

Figure 2. Estrogen deprivation by ovariectomy (OVX) results in decreased bone volume fraction of trabecular bone in the tibia, femur, and spine in C57Bl/6 mice as assessed by bone microCT.

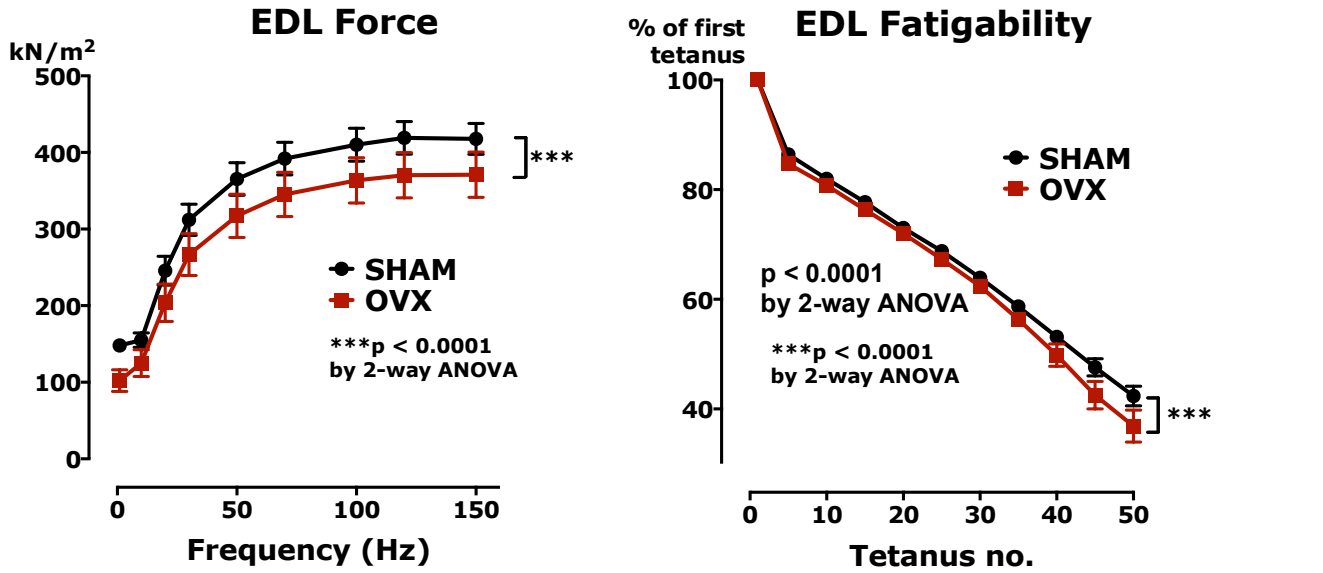

Figure 3. Estrogen deprivation by ovariectomy (OVX) resulted in reduced isolated whole muscle contractility in the extensor digitorum longus muscle (EDL) and reduced time to fatigue in C57Bl/6 mice.

- **Studies conducted during the next project period will examine whether these effects are exacerbated by the addition of an AI or SERM in non-tumor bearing C57Bl/6 mice. Addition of these two drug treatment groups will complete Task 1.**

Task 2. *Evaluate biochemical changes in skeletal muscle resulting from estrogen (E2) deprivation therapy.* **[20% complete]**

a. *Using frozen muscle samples saved from Task 1, nitrosylation and oxidation of RyR1 as well as assessment of calstabin1 depletion from RyR1 will be evaluated by co-immunoprecipitation in tissues from E2-replete sham-operated mice, OVX mice, OVX + AI-treated mice and OVX + SERM-treated mice.*

- **Using muscle collected from OVX and sham-operated mice in Task 1, whole muscle lysates were immunoprecipitated for co-expression of RyR1 and calstabin1. While a trend was present, I did not find a statistical difference in calstabin1:RyR1 levels in OVX mice relative to sham-control mice (Figure 4), indicating that muscle dysfunction observed in E2 deprived mice (Figure 3) may not be caused by RyR1 dissociation from calstabin1.**

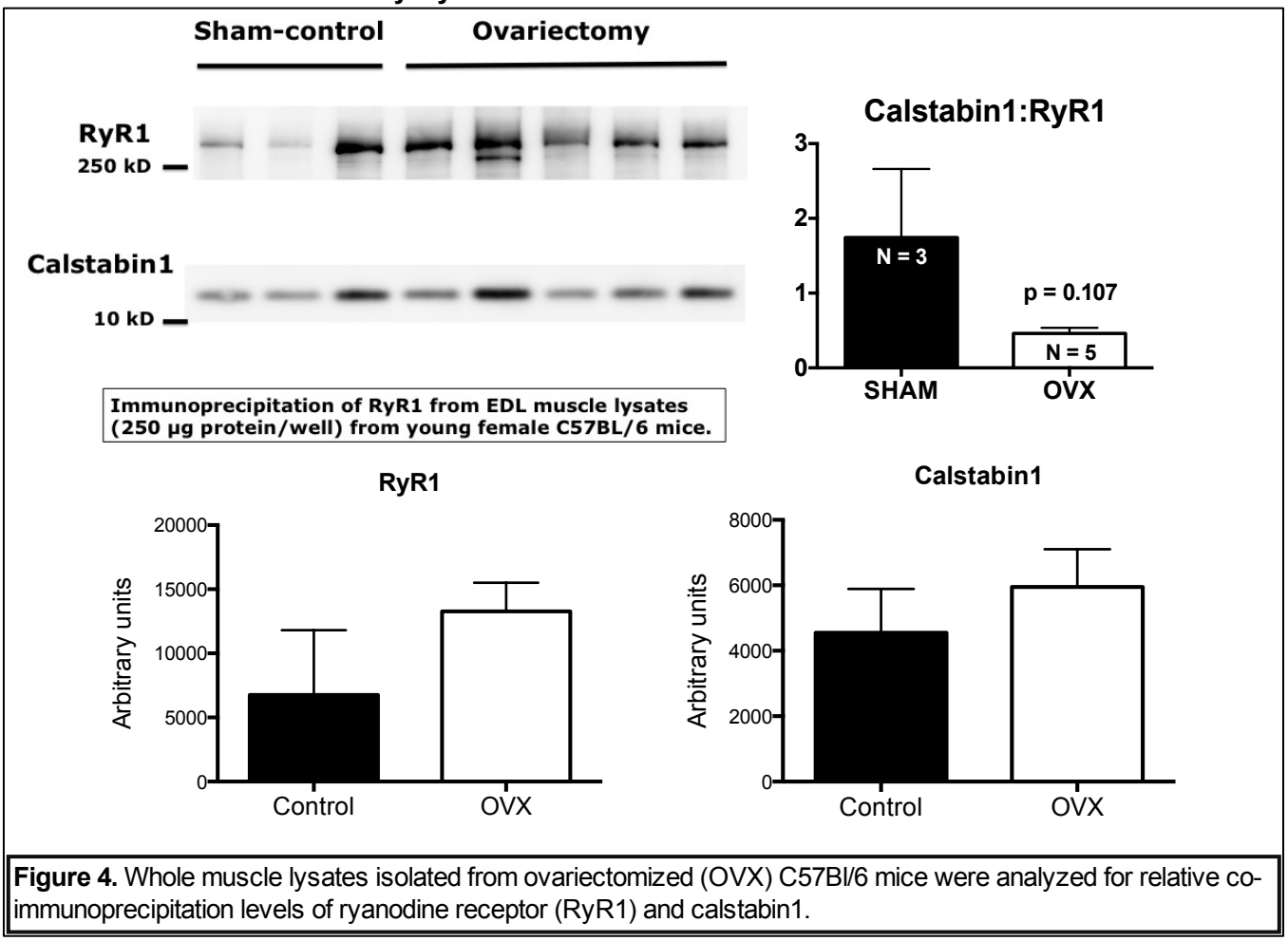

Figure 4. Whole muscle lysates isolated from ovariectomized (OVX) C57Bl/6 mice were analyzed for relative co-immunoprecipitation levels of ryanodine receptor (RyR1) and calstabin1.

- **During the next reporting period, I will assess oxidation and nitrosylation of RyR1 in these lysates as well as in lysates collected from AI- and SERM-treated muscle. New *in vitro* studies are underway to determine what other cellular and molecular mechanisms may contribute to muscle weakness in our model (see *Changes/Problems*).**

Task 3. *Evaluate whether the degree of AI- and SERM-induced muscle weakness correlates with treatment-induced bone loss.* **[50% complete]**

a. *Using the DXA and µCT scans acquired during Task 1, changes in bone mineral density (BMD; whole body, proximal tibia, distal femur and spine), trabecular bone microarchitectural properties (BV/TV, Tb.N. Tb.Sp, Tb.Th, Conn-D, SMI) and cortical bone properties (BA/TA, CortThick, medullary area) will be quantified at baseline and at the final endpoint in E2-replete sham-operated mice, OVX mice, OVX + AI-treated mice and OVX + SERM-treated mice. Regression analyses and ANOVA will be utilized to assess the relationship between bone loss and muscle*

weakness in our model. Representative µCT images will be reconstructed and saved for future presentations and publication.

- **All DXA and µCT scans acquired during Task 1 have been analyzed and body composition and BMD results are expressed as percent change relative to baseline (Figure 1A,B). Bone micorarchitectural parameters assessed by µCT (Figure 5) revealed significant differences in OVX mice relative to sham control mice in respect to BV/TV, connectivity density, and structure model index (SMI). Representative reconstructions of the high-resolution µCT scans are presented in Figure 6 and will be included in future publications.**

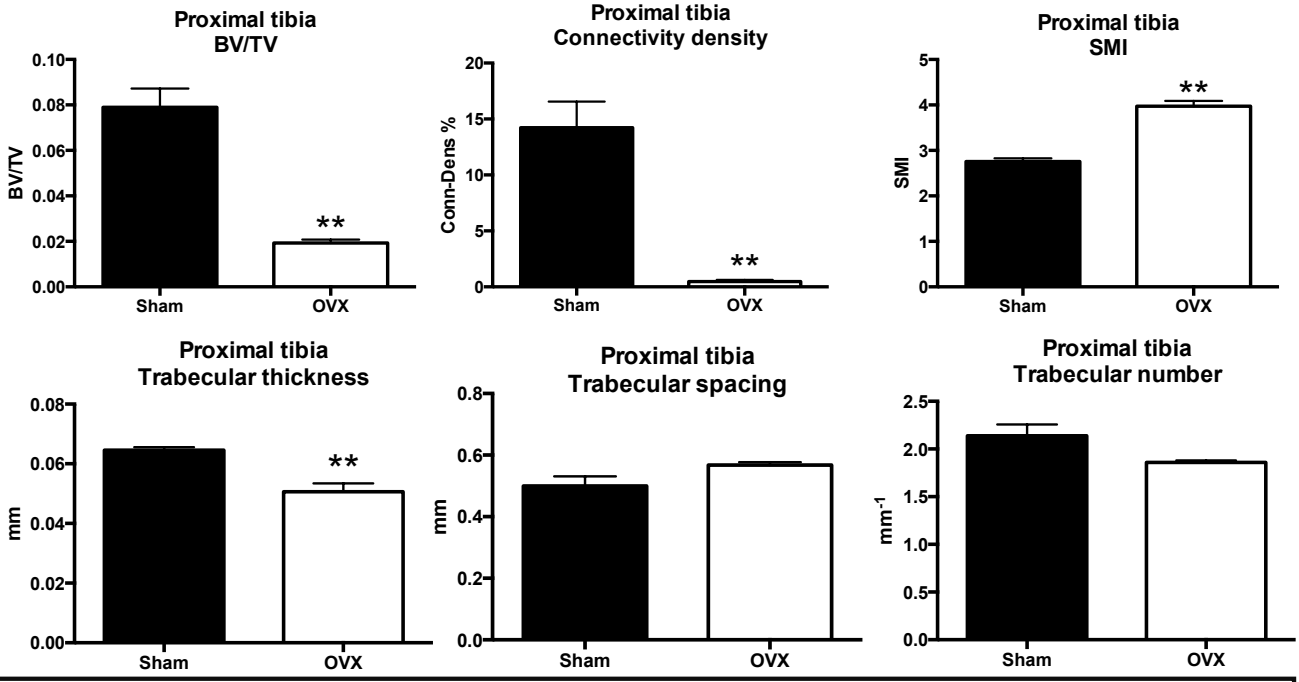

Figure 5. Estrogen deprivation by ovariectomy (OVX) resulted in reduced bone volume fraction (BV/TV), connectivity density, and increased structure model index (SMI) in C57Bl/6 mice in trabecular bone of the proximal tibia as assessed by µCT.

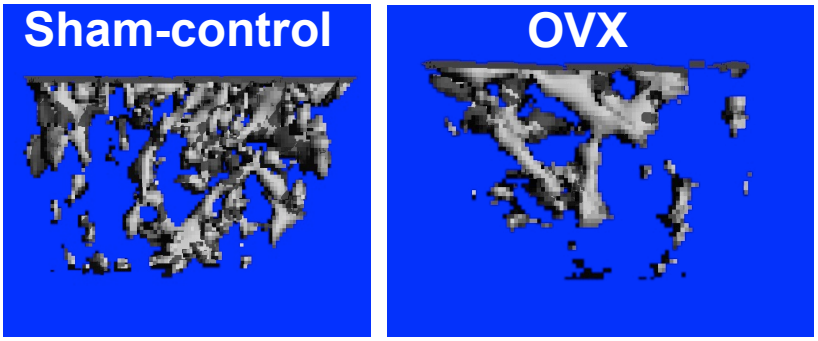

Figure 6. High-resolution bone µCT reconstructions demonstrate profound trabecular bone loss in estrogen-deprived ovariectomized (OVX) mice relative to sham-operated mice.

- **In the next reporting period, non-tumor-bearing AI and SERM-treated mice will likewise be evaluated for changes in body composition and bone-specific parameters by DXA and µCT. The complete data set will then be analyzed using regression analyses in order to determine the relationship between bone loss and muscle weakness in my model. Representative µCT reconstructions of all groups will be compiled and included in future reports and publications.**

Task 4. Determine whether prevention of osteoclastic bone resorption can ameliorate muscle weakness associated with E2 deprivation *in vivo*. **[0% complete]**

Task 5. Test the effects of pharmacological stabilization of RyR1 on muscle specific force production during E2 deprivation therapy treatment *in vivo*. **[0% complete]**

- **Because we have yet to find evidence for RyR1 channel instability *in vivo* in non-tumor bearing mice (Figure 4), I will postpone the testing of the novel pharmacological stabilizing agent rycal S107 until we can confirm a mechanistic justification for its use.**

Task 6. Determine whether estrogen deprivation therapy and breast cancer bone metastases are associated with maladaptive modifications to RyR1 in human tissue samples. **[0% complete]**

Task 7. Prepare manuscript containing novel findings from Tasks 1-6. **[0% complete]**

Task 8. Determine whether the E2 deprivation therapies letrozole (AI) or tamoxifen (SERM) accelerate the progression of breast cancer bone metastases *in vivo*. **[80% complete]**

a. *Conduct in vivo study comparing effects of OVX alone with or without AI treatment (letrozole; 5mg/kg/d; i.p., for two months) or SERM treatment (tamoxifen; 50mg/kg/d; i.p., for two months) relative to E2-replete sham-operated animals on bone metastases in athymic nude mice inoculated with MDA-MB-231 cells. After tumor cell inoculation, animals will be followed prospectively for six weeks for the development of bone metastases. Endpoints will include body composition by DXA, osteolytic lesion area by X-ray, changes in bone by μCT, serum levels of 17β-estradiol and inflammatory cytokines by Bio-Plex assay and grip strength.*

- **As planned, four-week female athymic nude mice underwent OVX or sham surgery and were treated daily with vehicle or AI (10μg/day; n=20/group). Three weeks after surgery and onset of treatment, serum levels of 17β-estradiol in OVX-AI mice were reduced by 56% (Figure 7A, $p<0.01$; Calbiotech ELISA) and trabecular bone volume fraction at the proximal tibia was reduced by 67% (Figure 8, $p<0.001$; SCANCO viva40CT) relative to vehicle-sham. After confirming estrogen deficiency and bone loss (Figures 7,8), the same animals were inoculated with ER-negative MDA-MB-231 human breast cancer cells into the left cardiac ventricle and followed for cancer progression in bone. Since MDA-MB-231 cells are ER-negative, effects of estrogen deprivation on the tumor should be indirect and attributed to the microenvironment.**

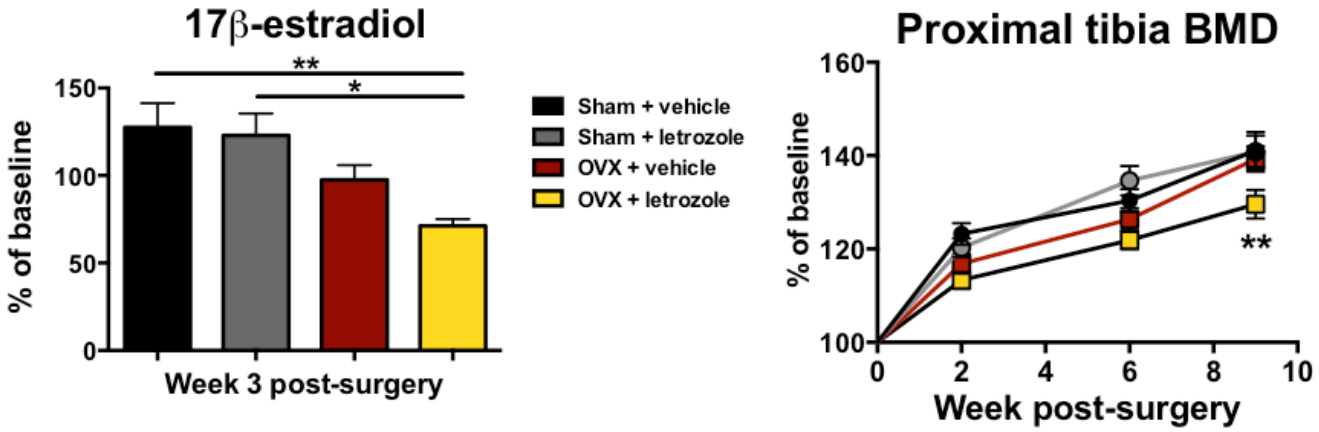

Figure 7. Three weeks post-surgery, serum 17β-estradiol levels were reduced as assessed by ELISA and bone mineral density (BMD) was reduced over time in OVX + letrozole-treated mice.

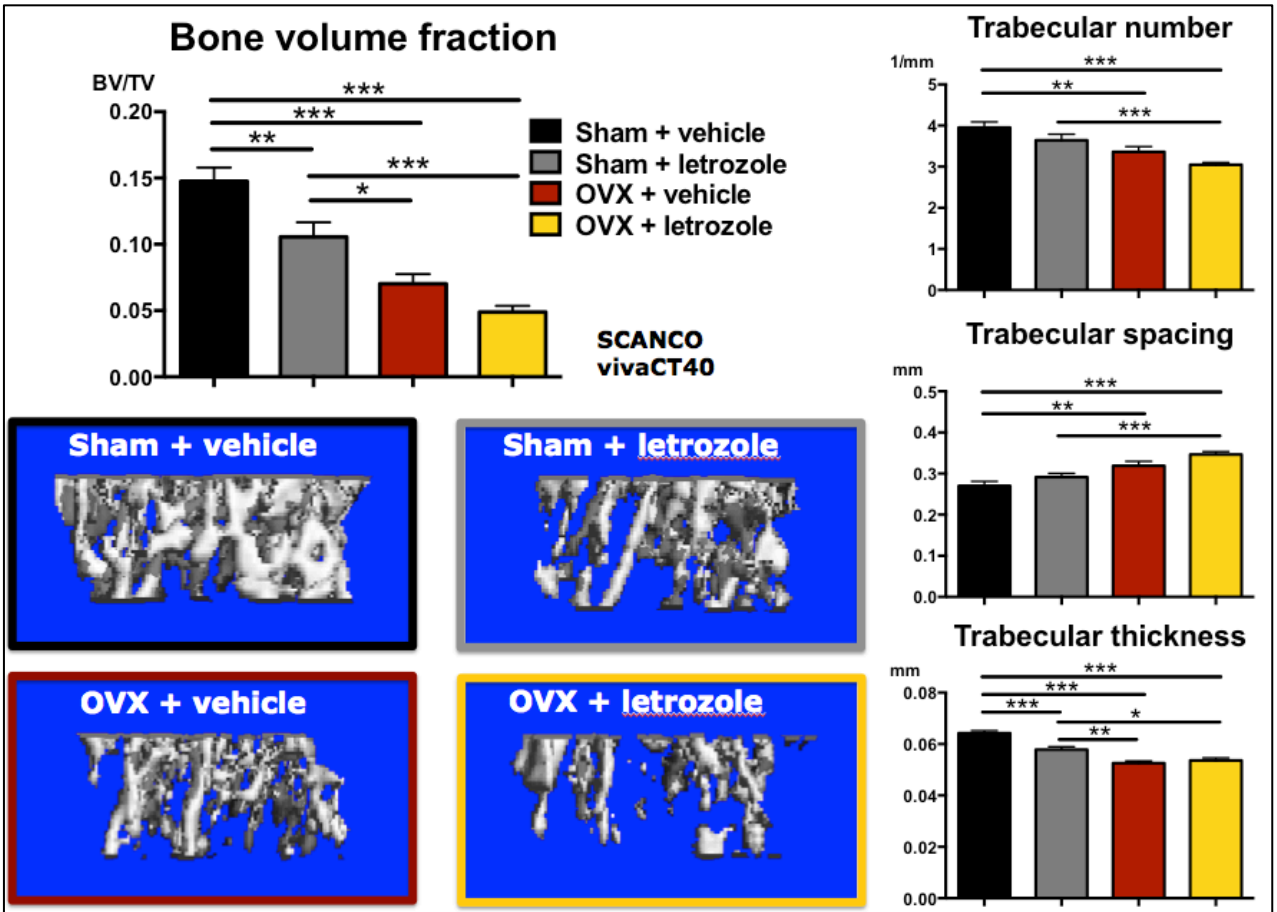

Figure 8. Three weeks post-surgery, bone volume fraction and bone microarchitectural parameters were compromised in OVX + letrozole-treated mice.

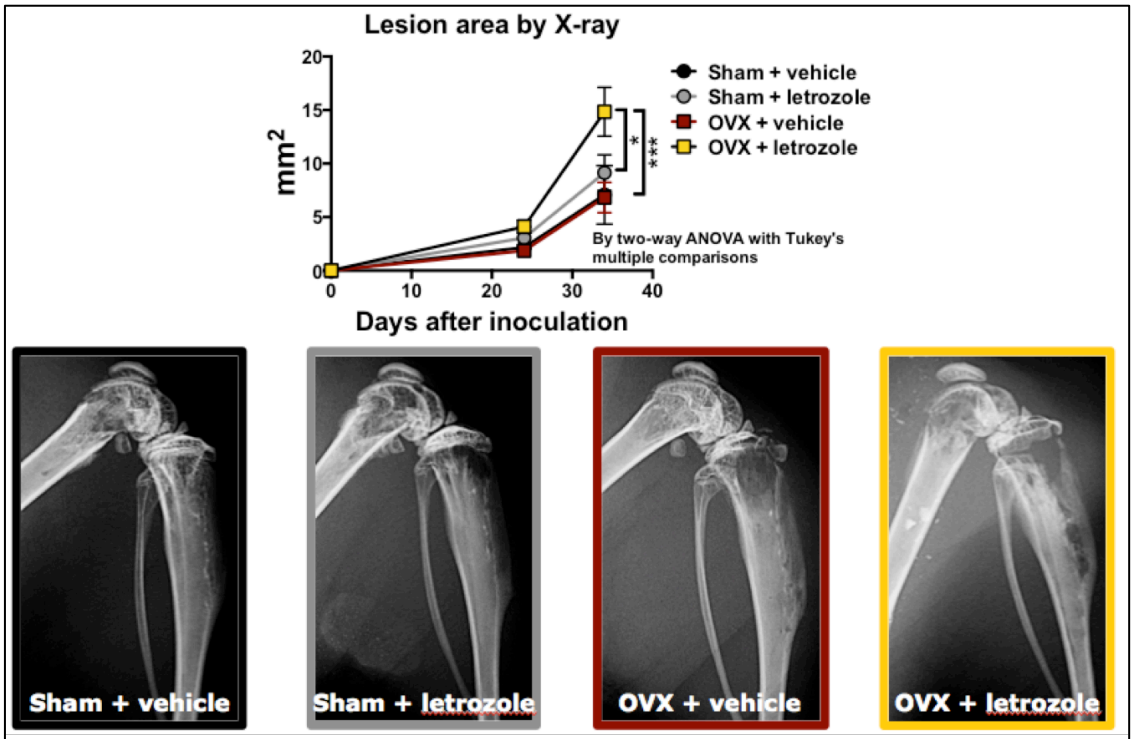

Figure 9. Five weeks after MDA-MB-231 cell inoculation, osteolytic lesion area was increased in OVX + letrozole-treated mice relative to all groups, as assessed by X-ray.

b. *Analyze bone tissue sections by histomorphometry for tumor burden, osteoclast#/mm bone-tumor interface, osteoclast#/mm^2 and osteoblast #/mm^2.*

- **Five weeks after inoculation, osteolytic lesion area increased by 110% (Figure 9, p<0.01, X-Ray) and tumor burden in bone assessed by histology was increased by 87% (Figure 10, p<0.01) in OVX-AI mice relative to sham-vehicle. Furthermore, ex vivo maximal contractile force of the extensor digitorum longus muscle was significantly reduced in OVX-AI mice (Figure 11, -12%, p<0.001) relative to sham-vehicle.**

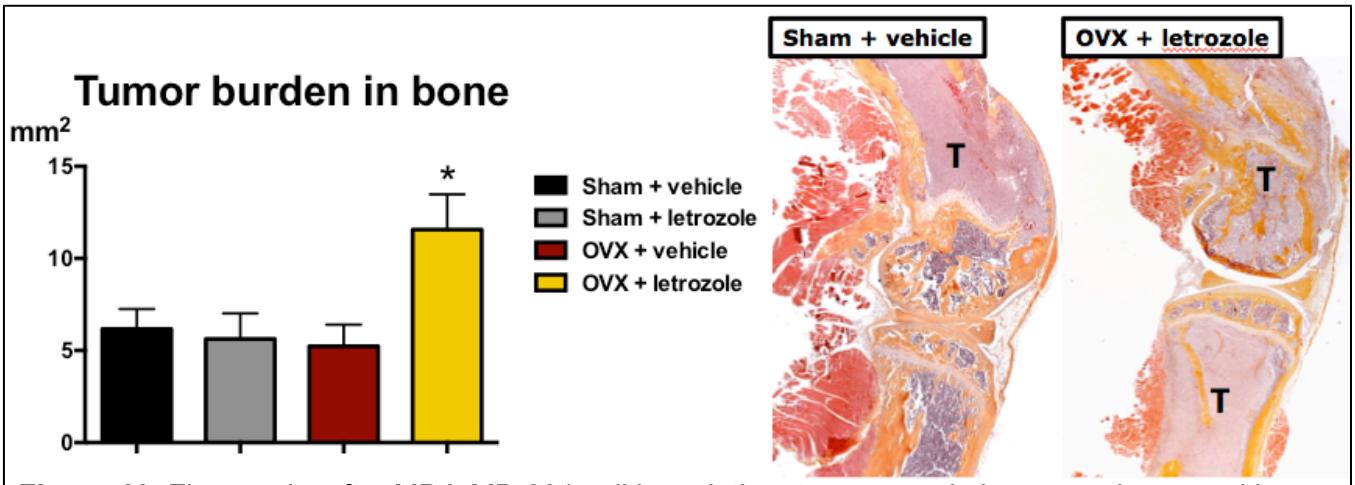

Figure 10. Five weeks after MDA-MB-231 cell inoculation, tumor area in bone was increased in OVX + letrozole-treated mice relative to all groups.

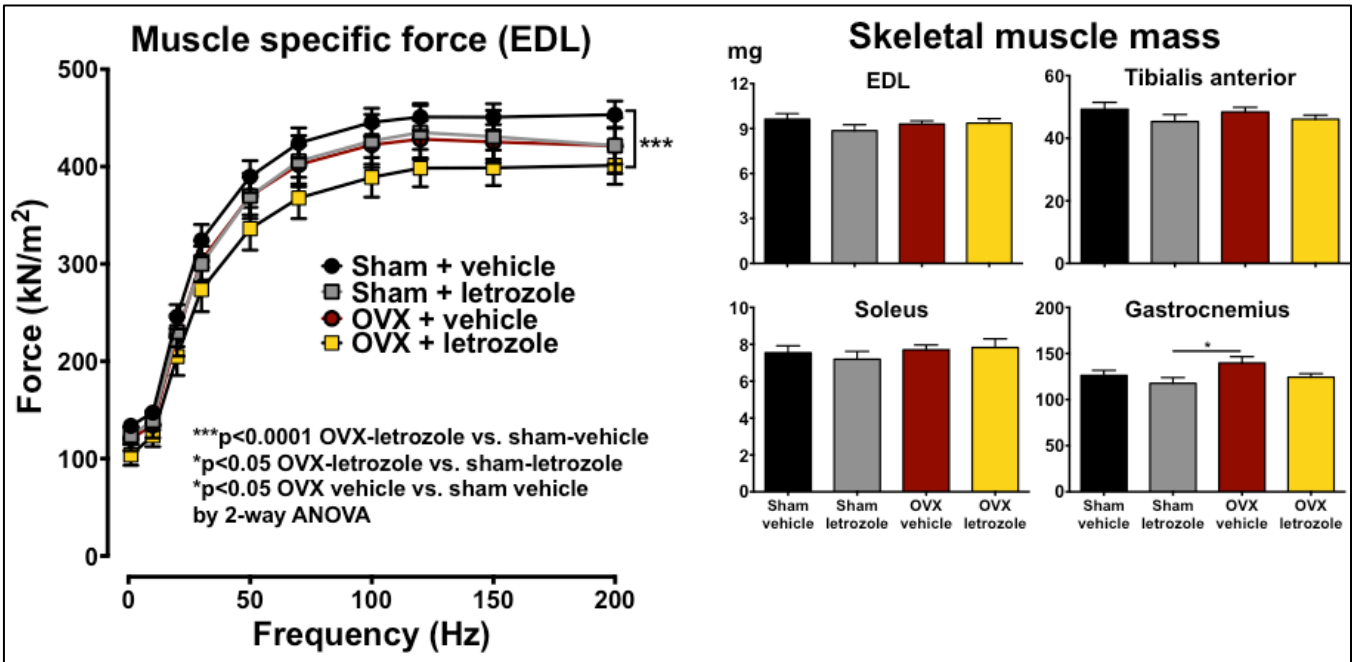

Figure 11. Five weeks after MDA-MB-231 cell inoculation, isolated whole muscle contractility was reduced in OVX mice treated with letrozole despite no change in muscle mass.

- **My studies in Task 8 confirmed that AI treatment induced bone loss and skeletal muscle weakness, recapitulating effects in cancer patients. As hypothesized, the severe bone loss resulting from AI-induced estrogen depletion may prime the bone microenvironment for the development of breast cancer metastases to bone**

and potentiate muscle weakness. This model serves as an excellent tool to study the mechanisms of underlying musculoskeletal defects in cancer patients and to assess potential therapeutics. Studies in Task 9 will evaluate whether protection of bone with bisphosphonates can prevent AI-induced musculoskeletal complications in my model of breast cancer bone metastases.

- **The only remaining work in Task 8 involves quantitating the osteoclast numbers in TRAcP-stained histology slides (in preparation) as well as the addition of one more treatment group (SERM), which I anticipate performing during the next reporting period.**

Task 9. Determine whether prevention of E2 deprivation-induced bone loss can reduce the progression of breast cancer bone metastases *in vivo*. **[95% complete]**

a. *Using the same in vivo model of breast cancer bone metastases described in Task 8, OVX mice treated with AI (letrozole; 5mg/kg/d; i.p., for two months) will be treated with the bisphosphonate zoledronic acid (ZA; 0.5 mg/kg/d), and monitored for changes in bone. After two months, mice will be inoculated with MDA-MB-231 cells and followed for six weeks for the development of bone metastases. Endpoints will include body composition by DXA, osteolytic lesion area by X-ray, changes in bone by μCT, serum levels of 17β-estradiol and inflammatory cytokines by Bio-Plex assay and grip strength.*

- **As planned, OVX mice treated with AI (letrozole; 5mg/kg/d; i.p.) were also treated with the bisphosphonate zoledronic acid (ZA; 0.5 mg/kg/d), and monitored for changes in bone. As anticipated, AI-treated OVX mice lost bone relative to sham-controls, however, bisphosphonate treatment drastically reversed these deleterious effects in bone (Figure 12).**

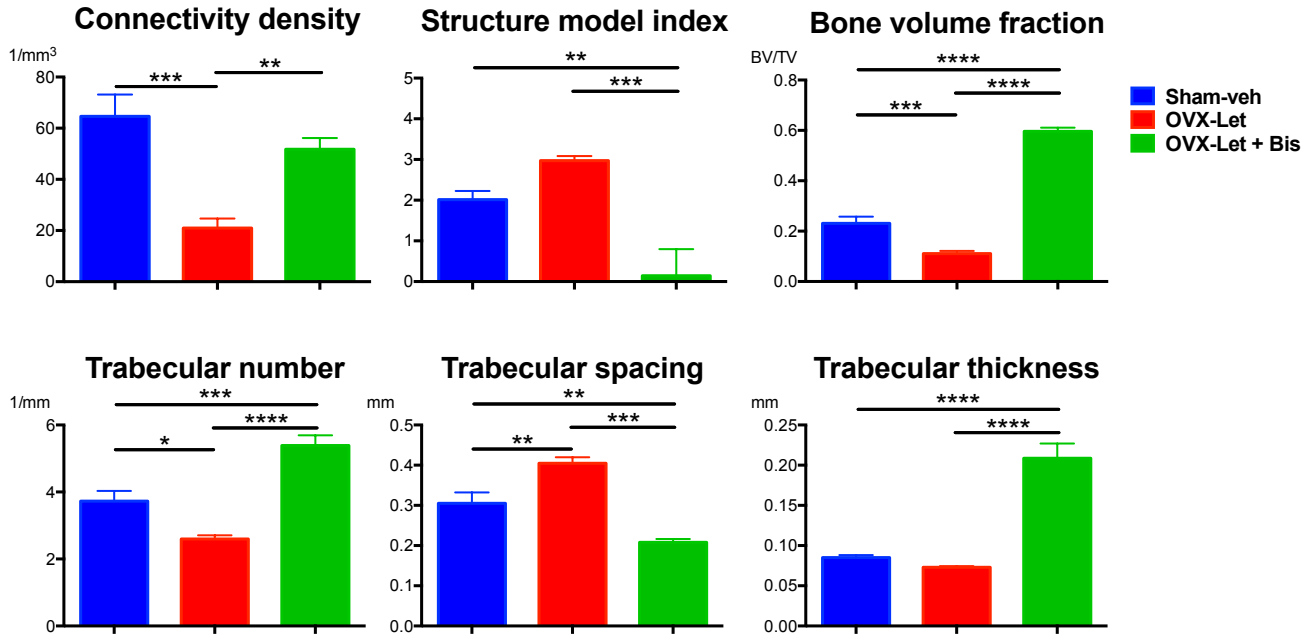

Figure 12. Three weeks post-surgery, bone volume fraction and bone microarchitectural parameters were compromised in OVX + letrozole-treated mice, and these effects were reversed by bisphosphonates.

- **After bone loss was confirmed in OVX-letrozole treated mice, MDA-MB-231 cells were inoculated into the left cardiac ventricle and mice were followed prospectively for changes in body weight and grip strength (Figure 13).**

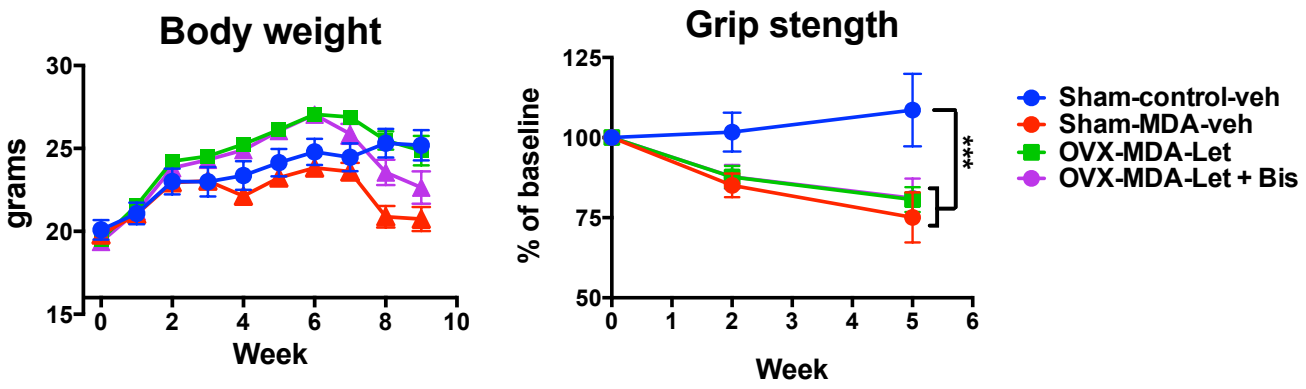

Figure 13. Following inoculation with breast cancer cells, weight and grip strength declined in cancer-bearing mice and these effects were not reversed by bisphosphonate treatment.

- **Despite no change in body weight or grip strength in bisphosphonate-treated mice, osteolytic lesion area was reduced relative to OVX-letrozole-treated mice and sham-vehicle-treated mice (Figure 14).**

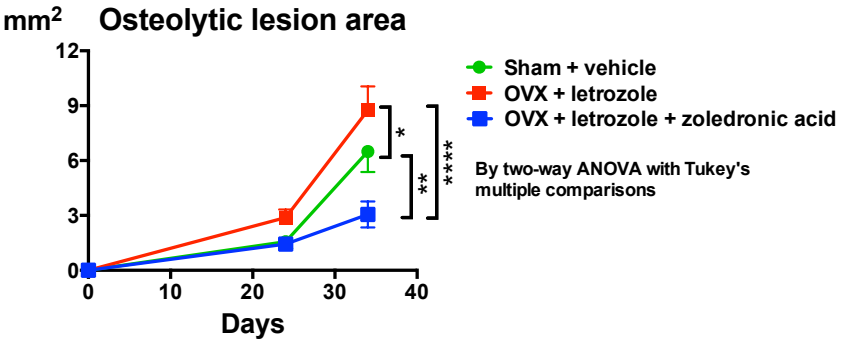

Figure 14. Osteolytic lesion area was increased in estrogen-deprived mice (OVX + letrozole) relative to sham + vehicle treated mice and this effect was reversed by the addition of bisphosphonates.

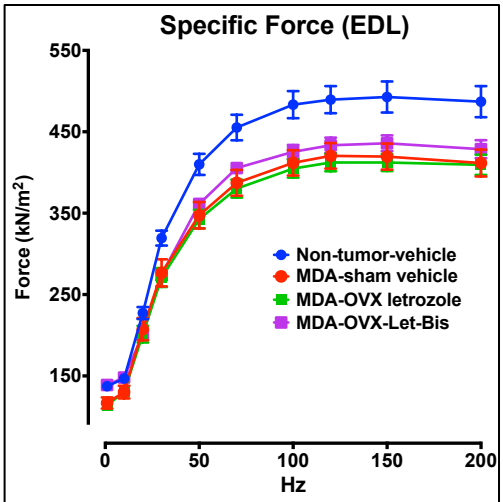

Figure 15. Five weeks after MDA-MB-231 cell inoculation, isolated whole muscle contractility was reduced in all cancer-bearing mice relative to non-tumor bearing control mice. Bisphosphonate-treated mice had slightly increased muscle specific force relative to other cancer-bearing groups.

- **At the time of sacrifice, *ex vivo* whole muscle contractility of the EDL was recorded in all treatment groups and cancer-bearing mice with bone metastases had reduced muscle specific force relative to non-tumor control (Figure 15). Bisphosphonates improved muscle contractility slightly, however, this trend did not reach statistical significance.**
- **Histological assessment of tumor in bone and quantitation of osteoclast cells by histology (slides are in preparation) will be performed during the next reporting period. All serum samples have been collected and 17β-estradiol levels will be assessed at baseline, week 3, and week 9 such that changes in sex steroids can be monitored over time.**
- **Data obtained in Task 9 support the hypothesis that a state of high bone turnover can prime the bone microenvironment to increase the progression of breast cancer growth in bone.**

Task 10. Test the effects of pharmacological stabilization of RyR1 on muscle specific force production during E2 deprivation therapy treatment in cancer-bearing mice with bone metastases. **[10% complete]**

- **In order to confirm that RyR1 dissociation from its stabilizing subunit calstabin1 contributes to muscle weakness with anti-E2 therapy, the amount of calstabin1 bound to RyR1 was determined by immunoprecipitation of RyR1 followed by immunoblotting for RyR1 and calstabin1. I also assessed oxidation (DNP) and nitrosylation (Cys NO) of RyR1 in order to determine whether maladaptive modifications to RyR1 could be contributing to its instability. Calstabin1 binding to RyR1 was reduced only in OVX-vehicle-treated muscle while all OVX muscle lysates (both vehicle and letrozole treated) had increased oxidation and nitrosylation relative to sham-operated animals (Figure 16).**

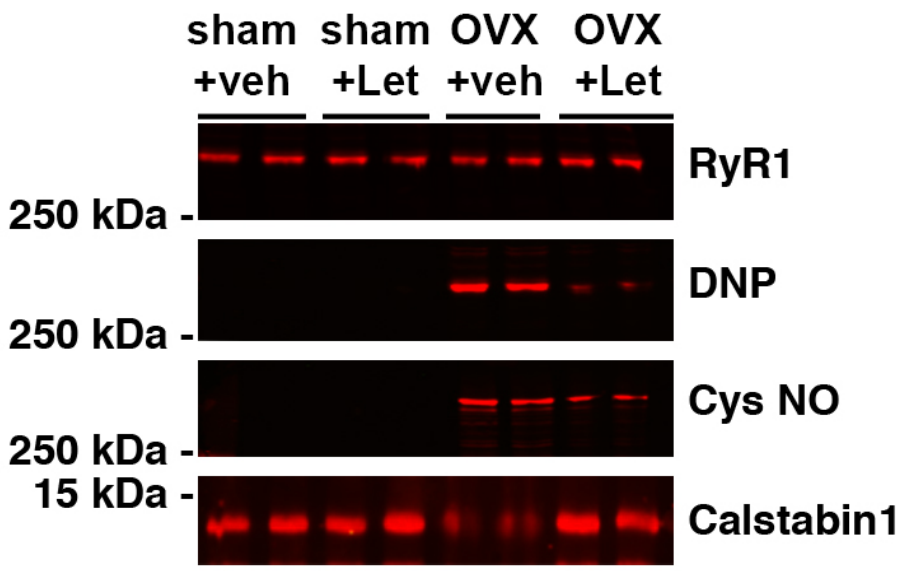

Figure 16. Immunoprecipitation of RyR1 from EDL muscle lysates (250µg protein/well) from cancer-bearing mice revealed no significant change in calstabin1 binding; however, oxidation (DNP) and nitrosylation (Cys NO) of the channel were detected in both OVX groups.

- **Because I have yet to definitively confirm that RyR1 channel instability in tumor-bearing OVX and letrozole-treated mice contributes to muscle weakness (Figure 16), I will postpone the testing of the novel pharmacological stabilizing agent rycal S107 until we can confirm a mechanistic justification for its use. On the other hand, oxidative stress and maladaptive nitrosylation of the channel appears to play a role in muscle weakness associated with ovarian estrogen depletion (OVX), and may represent an alternative mechanism for muscle weakness in this case.**

Task 11. Prepare manuscript containing novel findings from Tasks 8-10. **[0% complete]**

Training & professional development accomplishments

A major component to this postdoctoral grant involves scientific and professional training in order for me to reach my primary career objective of becoming an independent cancer investigator.

- During this award period, I learned the following laboratory techniques, which are required for the successful completion of the aims of this grant:
  1) micro-dissection of skeletal whole muscles from the hindlimbs of mice
  2) isolated whole muscle contractility measurement of the EDL and soleus muscles
  3) hormone and cytokine assays by ELISA
  4) grip strength measurement in mice
  5) subcutaneous injection of drugs in mice
  6) immunoprecipitation of proteins from muscle lysates

- In addition to technical training, I attended career development workshops at both the American Society for Bone and Mineral Research (ASBMR) conference in September 2014 and the Orthopedic Research Society (ORS) conference in August 2015.
- In the summer of 2015, I was selected as a scientific mentor for an undergraduate student through the National Institutes of Health (NIH) Bridges to Baccalaureate Program here at Indiana University. This opportunity was my first chance to serve as a scientific mentor to an up-and-coming scientist. The Bridges to the Baccalaureate program is a collaborative project between Indiana University-Purdue University Indianapolis (IUPUI) and Ivy Tech Community College of Central Indiana. This NIH-sponsored research program provides underrepresented minority students with experience in sciences within a research community and opens doors for those considering a career in research-related fields. During the eight-week program (June – August 2015), I trained the student in laboratory research techniques, aided in scientific writing, taught the student basic statistical concepts, and provided general college and career guidance.

Dissemination of results
Results for these studies were presented to peers and thought-leaders in the fields of oncology and bone biology at the American Society for Bone and Mineral Research (ASBMR) conference in September 2014 and the Orthopedic Research Society (ORS) conference in August 2015 (see full abstracts in the appendices).

Anticipated activities for the next reporting period (09/2015 – 09/2016)
Scientific goals:
◆ In brief, all non-tumor bearing studies using the immune competent C57Bl/6 mice (**Tasks 1-5**) will be completed during the next reporting period. Specifically, I will be examining the effects of AI and SERM treatment on C57Bl/6 mice and also examining the bone-protective effects of bisphosphonates on skeletal muscle function. In addition to being important to the field of cancer, the effects of bisphosphonate treatment on muscle is an emerging interest to the osteoporosis community, and thus my work during the next reporting period will be of interest to endocrinologists even *outside* of the field of oncology.

◆ A manuscript detailing the effects of AI treatment (letrozole) and subsequent E2 deprivation on breast cancer bone metastases and muscle function in mice (**Tasks 8**) will be prepared for publication in a top tier breast cancer journal. Results demonstrating that the protection of bone and muscle with the addition of bisphosphonates will also be included in this particular manuscript (**Task 9**).

◆ Head-to-head comparison of anti-E2 therapy-induced musculoskeletal toxicities will be conducted with AIs and SERMs in tumor-bearing mice (**Tasks 1 and Task 8**).

Professional development goals
◆ During the next reporting period, I will be applying for the American Society for Bone and Mineral Research (ASBMR) John Yaddad Young Investigator Award to attend the Advances in Mineral Metabolism (AIMM) Meeting, March 27-March 31, 2016 in Snowmass, Colorado. Awardees receive travel support and the opportunity to present their research, as well as interact with senior investigators and leaders in the field.

◆ The head of the Endocrinology Section in the Department of Medicine has nominated me for a promotion to junior faculty at Indiana University. If the nomination is awarded, the promotion would contribute to my career development in terms of access to faculty resources and privileges (e.g., human tissue bank, seminars, conferences, eligibility for faculty awards, etc.,), which I foresee having an overall positive impact on this DoD project, and certainly on my progression toward becoming an independent cancer researcher.

4. IMPACT

Impact of accomplishments on breast cancer field
Results obtained during this reporting period were significant for the field of breast cancer metastasis in that they support the concept that a state of high bone turnover can alter the bone

microenvironment to increase the progression of tumor growth at this site. The greater implications for the field are that any treatment or environmental factor that leads to bone loss (e.g., glucocorticoids, GnRH inhibitors, radiation, fracture, osteoporosis, etc.) could increase the homing of dormant disseminated cancer cells to the skeleton. Clinicians thus need to be mindful of bone health in breast cancer patients and survivors.

Impact of accomplishments on progress of the project

The project was significantly advanced during this first reporting period. All muscle physiology techniques have been mastered such that I am able to perform my studies independently of my co-mentor Dr. Andrew Marks at Columbia University. The animal studies performed (**Tasks 1-3,8,9**) were sizable and results up to this point support the hypothesis that bone loss associated with E2 deprivation can increase the progression of bone metastases. Further work will be necessary to determine the relative contribution of RyR1 channel instability in muscle weakness, and new aims and ideas have emerged in the first reporting period that will guide studies in the following reporting periods (see Changes/Problems).

Impact on society and public health

Next to nothing is known about the impact that hormone therapies have on muscle function at the cellular and molecular level, despite clinical reports of muscle weakness in patients undergoing AI treatment. Work from this first reporting period investigating this common yet understudied complication of breast cancer treatment revealed that oxidation and nitrosylation of calcium channels in skeletal muscle might be associated with muscle weakness. If this can be confirmed in future reporting periods, antioxidants may be a viable therapeutic in the prevention or treatment of muscle weakness with AI therapy.

Finally, cancer mortality is typically not caused by growth of the primary tumor, but rather is the result of complications associated with tumor cell metastasis to secondary organ sites including bone. Information obtained from my studies could help guide the selection of therapeutics for breast cancer patients and survivors, with emphasis on the importance of maintaining bone health in order to reduce patient risk of deadly breast cancer bone metastases. The studies presented here address important unanswered clinical questions that have the potential to improve the quality and longevity of life for breast cancer patients.

5. CHANGES/PROBLEMS

Changes in approach and reasoning

Initially I hypothesized that E2 deprivation therapy-induced muscle weakness was caused by dissociation of the RyR1-calstabin complex; however, co-immunoprecipitation of RyR1 and calstabin1 from muscle lysates of aromatase inhibitor-treated mice revealed little change in relative expression levels of this key calcium handling complex (**Figure 4, Figure 16**). I therefore will be pursuing new potential molecular targets in skeletal muscle in order to explain the functional defect observed in skeletal muscle contraction in mice treated with aromatase inhibitors. New studies will be initiated using an *in vitro* muscle culture system. Specifically, I will examine the direct effects of bisphosphonates (zoledronic acid; 0.001-10μg/mL), aromatase inhibitors (letrozole; 0.001-10μg/mL), and selective estrogen receptor modulators (SERM; tamoxifen, 0.001-10μg/mL) on C2C12 myotube cultures. In these new studies, I will perform dose-response assays on differentiated myotubes and examine (in addition to RyR1 and calstabin1) the following new endpoints in order to more fully characterize drug treatment-induced changes in skeletal muscle:

1. oxidation of RyR1 and SERCA1
2. nitrosylation of RyR1 and SERCA1
3. relative SERCA1 expression levels
4. muscle cell proliferation and death by MTT and LDH assays, respectively
5. ubiquitin ligase expression
6. phosphorylated and un-phosphorylated myosin heavy chain expression
7. phosphorylated and un-phosphorylated myosin light chain expression
8. changes muscle fiber morphology

This new *in vitro* aim will help me accomplish one of my primary objectives, which is to determine the mechanism(s) of anti-E2 therapy-induced muscle weakness. Should any of these new targets be altered by drug treatment in cell culture, I will corroborate the findings by following up with *in vivo* muscle studies.

Because we have yet to find evidence for RyR1 channel instability *in vivo* (**Figure 4, Figure 16**), I will postpone the testing of the novel pharmacological stabilizing agent rycal S107 as proposed in Tasks 5 & 10 until we can confirm a mechanistic justification for its use.

Anticipated problems or delays
Nothing to report

Changes that had a significant impact on expenditures
Nothing to report

Changes in use or care of vertebrate animals
During the course of the *in vivo* study outlined in Task 8, the Indiana University Laboratory Animal Research Care (LARC) facility staff members made a faulty batch of xylezine/ketamine anesthesia mix. As a result, eight of my mice were lost on the day of tumor inoculation. In response to this error, my mentor Theresa Guise M.D. requested that the LARC facility reimburse me for the lost time and animals. Furthermore, Dr. Guise has since been granted a Drug Enforcement Administration (DEA) controlled substances license and approval from the Institutional Animal Care and Use Committee such that we may now prepare the anesthesia in our own laboratory. No anesthesia-related mouse fatalities have since been reported.

6. PRODUCTS—*see appendices for full details*

Awards:

1. National Institutes of Health (NIH) Clinical Loan Repayment Program (LRP) through the National Cancer Institute (NCI) $33,568 – *no salary or research supply support*
2. American Society for Bone and Mineral Research (ASBMR) Harold M. Frost Young Investigator Travel Award $1,500 – *no salary or research supply support*

Invited seminar:

Orthopedic Research Society (ORS) Sun Valley Workshop on Musculoskeletal Biology, Featured Young Investigator, Sun Valley, ID, August 3rd, 2015.
Title: Bone Loss Due to Complete Estrogen Deprivation Causes Muscle Weakness and Increased Progression of ER-Negative Breast Cancer in Bone

Poster presentation:

Wright LE, Harhash AA, Waning DL, Chiechi A, Mohammad KS, Marks AR, Guise TA. Letrozole and ovariectomy cause bone loss, muscle weakness and increased breast cancer bone metastases in mice. American Society for Bone and Mineral Research (ASBMR) Annual Meeting, Houston, TX, September 2014.

Peer-reviewed publications:

1. **Wright LE**, Ottewell PD, Rucci N, Peyruchaud O, Pagnotti GM, Chiechi A, Buijs JT, Sterling JA. Murine models of breast cancer bone metastases. *Bonekey Rep*. 2015 (under review).
   This methods review article 1) identifies the most commonly utilized breast cancer cell lines that elicit osteolytic, osteoblastic, or mixed phenotypes in bone, 2) provides protocols for tumor cell inoculation routes that model metastatic breast cancer in the skeleton, and 3) explores methods for the post-inoculation monitoring of cancer progression in bone.

2. Waning DL, Mohammad KS, Reiken SR, Wenjun X, Anderssen DC, John S, Chiechi A, **Wright LE**, Umanskaya A, Niewolna M, Trivedi T, Charkhzarrin S, Khatiwada P, Wronska A, Haynes A, Benassi MS, Witzmann FA, Zhen G, Wang X, Cao Z, Roodman GD, Marks AR, Guise TA. TGFβ mediates muscle weakness associated with bone metastases. *Nature Med*. 2015 Oct 12. doi: 10.1038/nm.3961. [Epub ahead of print].

7. PARTICIPANTS & OTHER COLLABORATING ORGANIZATIONS

Primary investigator (PI): Laura E. Wright, Ph.D. – *no change*.

8. SPECIAL REPORTING REQUIREMENTS

Nothing to report

9. APPENDICES

See attached documents

LAURA E. WRIGHT

Curriculum Vitae

Postdoctoral Research Fellow
Indiana University School of Medicine
Department of Medicine, Division of Endocrinology
980 West Walnut Street
Walther Hall R3, Room #C122
Indianapolis, IN 46202

Laboratory: 317.278.7785
FAX: 317.278.2912
Mobile: 425.802.7377
Laewrig@iu.edu

EDUCATION

- Executive Certificate in the Business of Life Sciences, Kelley School of Business, Indiana University, Bloomington IN – 2015
- Ph.D., Physiological Sciences, University of Arizona, Tucson, AZ – 2012
- M.S., Physiological Sciences, University of Arizona, Tucson, AZ – 2007
- B.S., Human Biology, Biola University, La Mirada, CA – 2005

OBJECTIVE

My long-term objective is to become an independent musculoskeletal investigator at a top-tiered academic institution where I am able to make meaningful contributions not only in research, but also in leadership, mentorship, and administrative roles.

PROFILE

During my doctoral studies, I conducted basic and translational research focused on endocrine regulation of bone during ovarian senescence using chemical and surgical models of menopause. After firmly establishing an interest in endocrinology and metabolic bone disease, I obtained a National Institutes of Health (NIH) Research and Service Award (NRSA) to fund my pre-doctoral training. During this period, I worked to elucidate the bone-protective effects of a natural product-derived drug compound in models of osteoporosis and breast cancer bone metastasis. These pre-doctoral efforts resulted in five first author peer-reviewed publications. Cancer therapy-induced musculoskeletal complications emerged as a primary research interest; I therefore accepted a postdoctoral fellowship in the laboratory of Dr. Theresa Guise at Indiana University, a preeminent multidisciplinary research group that specializes in the study of solid tumor metastasis to bone. During my time at Indiana University, I have published three first author peer-reviewed manuscripts, including primary research findings detailing the cellular mechanisms of radiation-induced bone loss. Importantly, I obtained three years of funding from the Department of Defense (DoD), which supports my current investigative work focusing on the molecular mechanisms of musculoskeletal toxicities associated with anti-estrogen therapy in breast cancer patients. Multidisciplinary training, a strong commitment to research, and exceptional mentorship uniquely equip me to make a significant impact in the fields of endocrinology, oncology, and musculoskeletal disease.

POSITIONS

2012 – present	Postdoctoral Research Fellow, Department of Medicine, Division of Endocrinology, Indiana University-Purdue University, Indianapolis, IN
2006 – 2012	Graduate Research Associate, Department of Medicine, Endocrinology Section, University of Arizona, Tucson, AZ
2007 – 2008	Lecturer, Anatomy and Physiology, Cortiva Institute, Tucson, AZ
2005 – 2006	Graduate Research Assistant, McKnight Brain Institute, Neural Systems, Memory and Aging (NSMA), Department of Psychology, University of Arizona, Tucson, AZ
2005 – 2011	Graduate Teaching Assistant, Department of Physiology, University of Arizona, Tucson, AZ

EXPERIENCE AND PROFESSIONAL MEMBERSHIPS

2015 – present	Mentor, National Institutes of Health (NIH) Bridges to Baccalaureate Program, IUPUI, Indianapolis, IN

2013 – present	Member, American Medical Writers Association, Indiana Chapter
2012 – present	Member, The International Bone and Mineral Society
2007 – present	Member, The American Society for Bone and Mineral Research
2007 – present	Member, The Endocrine Society
2010 – 2012	Member, The Arizona Physiological Society
2009 – 2010	Member, Graduate Student Library Advisory Council Committee, University of Arizona
2008 – 2009	Member, Recruitment & Admission Committee, University of Arizona, Graduate Interdisciplinary Program in Physiological Sciences
2007 – 2011	Member, The American Society of Pharmacognosy

SEMINARS

08/03/15	Orthopedic Research Society (ORS) Sun Valley Workshop on Musculoskeletal Biology, Featured Young Investigator, Sun Valley, ID
11/1/13	Indiana University, Tumor Biology Microenvironment Program Seminar Series, Indianapolis, IN
08/14/12	The National Institutes of Allergy and Infectious Diseases (NIAID) Medical Countermeasures Against Radiological Threats (MCART) site visit to Indiana University, invited seminar, Indianapolis, IN
12/12/11	Indiana University, Tumor Biology Microenvironment Program Seminar Series, Indianapolis, IN
12/07/11	Veterans Affairs Medical Center/University of California-San Francisco, Bone Imaging Core, Endocrine Research Unit, San Francisco, CA
07/31/11	The American Society of Pharmacognosy Annual Meeting, Mechanism of Action Series, San Diego, CA
03/07, 11/08, 11/10	Physiological Sciences Student Forum Series Speaker, Arizona Health Sciences Center, University of Arizona, Tucson, AZ
11/04/10	Arizona Physiological Society, Featured Graduate Student Free Communication Lecturer, Midwestern University, Glendale, AZ

TEACHING EXPERIENCE

2009	University of Arizona Undergraduate Department of Physiology, Graduate Teaching Assistant, PSIO 480 “Human Physiology,” Discussion Section Lecturer
2005 – 2007	University of Arizona Undergraduate Department of Physiology, Graduate Teaching Assistant, PSIO 201 and PSIO 202 “Human Anatomy and Physiology,” Laboratory Instructor
2007	Cortiva Institute, Tucson, AZ, ANP 223 “Anatomy and Physiology IV CORE,” Lecturer

HONORS AND AWARDS

2015	National Institutes of Health (NIH) Clinical Loan Repayment Program (LRP) through the National Cancer Institute (NCI)
2015	American Society for Bone and Mineral Research (ASBMR) Harold M. Frost Young Investigator Award
2014	Department of Defense (DoD) – Breast Cancer Research Program Postdoctoral Fellowship Award (BC134025)
2012	Department of Defense (DoD) – Prostate Cancer Research Program Postdoctoral Fellowship Award (PC101890)
2013	Endocrine Fellows Foundation (EFF)/ASBMR Fellows Forum on Metabolic Bone Diseases award recipient, Baltimore, MD
2013	ASBMR President’s Poster Competition award recipient, Baltimore, MD
2011	National Institutes of Health (NIH) National Graduate Student Research Conference (NGSRC) award recipient, Bethesda, MD
2011	University of California-San Francisco (UCSF), Postdoctoral Bootcamp award recipient

2011 Women in Science and Engineering (WISE) Stipend Award Recipient, University of Arizona, Tucson, AZ
2009 North American Research Conference on Complementary & Integrative Medicine Trainee Travel Award recipient, Minneapolis, MN
2009 American Society of Pharmacognosy Student Travel Award Recipient, Honolulu, HI
2008 Ruth L. Kirschstein National Research Service Award (NRSA) for Individual Predoctoral Fellowship Training (F31, NIH/NCCAM)
2008 Trainee Award Recipient for the Endocrine Society Annual Meeting, Basic Sciences
2008 Herb Society of America Inc. Research Award Recipient
2008 1st Place Award Recipient—Best Abstract, Natural Supplements: An Evidence-Based Update Conference, Scripps Institute, San Diego, CA
2008, 2010 Herbert E. Carter Travel Award recipient, Graduate Interdisciplinary Programs, University of Arizona, Tucson, AZ

RESEARCH HIGHLIGHTS

Peer-Reviewed Publications

1. **Wright LE**, Ottewell PD, Rucci N, Peyruchaud O, Pagnotti GM, Chiechi A, Buijs JT, Sterling JA. Murine models of breast cancer bone metastases. *Bonekey Rep*. 2015 (in press).
2. Waning DL, Mohammad KS, Reiken SR, Wenjun X, Anderssen DC, John S, Chiechi A, **Wright LE**, Umanskaya A, Niewolna M, Trivedi T, Charkhzarrin S, Khatiwada P, Wronska A, Haynes A, Benassi MS, Witzmann FA, Zhen G, Wang X, Cao Z, Roodman GD, Marks AR, Guise TA. TGFβ mediates muscle weakness associated with bone metastases. *Nature Med*. 2015 Oct 12. doi: 10.1038/nm.3961. [Epub ahead of print].
3. **Wright LE**, Buijs JT, Kim HS, Coats LE, Scheidler AM, John SK, She Y, Murthy SM, Ma N, Chin-Sinex HJ, Bellido TM, Bateman TA, Mendonca MS, Mohammad KS, Guise TA. Single-limb irradiation induces local and systemic bone loss in a murine model. *J Bone Miner Res.* 2015, 30(7):1268-79.
4. **Wright LE**, Guise TA. The role of PTHrP in skeletal metastases and hypercalcemia of malignancy. *Clin Rev Bone Miner Metab*. 2014, 12(3):119-29.
5. **Wright LE**, Guise TA. The microenvironment matters: estrogen deficiency fuels cancer bone metastases. *Clin Cancer Res*. 2014, 20(11):2817-9.
6. **Wright LE**, Frye JB, Gorti B, Timmermann BN, Funk JL. Bioactivity of turmeric-derived curcuminoids and related metabolites in breast cancer. *Current Pharma Design*. 2013, 19(34):6218-25.
7. **Wright LE**, Frye JB, Timmermann BN, Mohammad KS, Guise TA, Funk JL. Curcuminoids block TGF-β signaling in human breast cancer cells and limit osteolysis in a murine model of breast cancer bone metastasis. *J Nat Prod.* 2013, 76(3):316-21.
8. Frye JB, Lukefahr AL, **Wright LE**, Marion SL, Hoyer PB, Funk JL. Modeling perimenopause in Sprague-Dawley rats by chemical manipulation of the transition to ovarian failure. *Comp Med*. 2012, 62(3):193-202.
9. Lukefahr AL, Frye JB, **Wright LE**, Marion SL, Hoyer PB, Funk JL. Decreased BMD in rats rendered follicle deplete by an ovotoxic chemical correlates with changes in follicle-simulating hormone and inhibin A. *Calcif Tissue Int*. 2012, 90(3):239-49.
10. **Wright LE**, Frye JB, Lukefahr AL, Marion SL, Hoyer PB, Besselsen DG, Funk JL. 4-vinylcyclohexene diepoxide (VCD) inhibits mammary epithelial differentiation and induces fibroadenoma formation in female Sprague Dawley rats. *Reprod Toxicol*. 2011, 32(1):26-32.
11. **Wright LE**, Frye JB, Timmermann BN, Funk JL. Protection of trabecular bone in ovariectomized rats by turmeric is dependent on extract composition. *J Agric and Food Chem*. 2010, 58(17):9498-504.
12. **Wright LE**, Christian PJ, Rivera Z, Van Alstine WG, Funk JL, Bouxsein ML, Hoyer PB. Comparison of skeletal effects of ovariectomy versus chemically-induced ovarian failure in mice. *J Bone Miner Res*. 2008, 23(8):1296-303.

Abstracts (Presented):

1. **Wright LE**, Harhash AA, Waning DL, Chiechi A, Mohammad KS, Marks AR, Guise TA. Letrozole and ovariectomy cause bone loss, muscle weakness and increased breast cancer bone metastases in mice. American Society for Bone and Mineral Research Annual Meeting, Houston, TX, September 2014.

2. **Wright LE**, Harhash AA, Waning DL, Chiechi A, Mohammad KS, Marks AR, Guise TA. Ovariectomy combined with aromatase inhibitor treatment cause bone loss, muscle weakness and increased breast cancer metastases in mice. International Bone & Mineral Society's 13th International Conference on Cancer-Induced Bone Disease, Miami, FL, November 2013.
3. **Wright LE**, Joseph D, Harhash A, Waning D, John S, Mohammad KS, Marks AR, Guise TA. Effects of sex steroid deprivation on skeletal muscle function and ryanodine receptor (RyR1) modulation. American Society for Bone and Mineral Research Annual Meeting, Baltimore, MD, October 2013.
4. **Wright LE**, Buijs JT, John S, Peng Z, Harhash A, Waning D, Mohammad KS, Mendonca M, Chua HL, Wolfe H, Marks A, Orschell C, Guise TA. Ionizing radiation induced both direct and systemic bone loss in murine models. International Bone & Mineral Society's 12th International Conference on Cancer-Induced Bone Disease, Lyon, France, November 2012.
5. **Wright LE**, Guise TA, Mohammad KS, Funk JL. Curcuminoids decrease osteolytic breast cancer bone metastases. The Endocrine Society Annual Meeting, Boston, MA, June 2011.
6. **Wright LE**, Lukefahr AL, Frye JB, Hoyer PB, Besselsen DG, Funk JL. 4-Vinylcyclohexene Diepoxide (VCD)-induced fibroadenomas: a novel rat model of mammary tumorigenesis. The Endocrine Society Annual Meeting, San Diego, CA, June 2010.
7. **Wright LE**, Beischel Frye J, Timmermann BN, Funk JL. Curcuminoid-containing turmeric protects bone mass and microarchitecture in ovariectomized rats. American Society for Bone and Mineral Research Annual Meeting, Denver, CO, September 2009.
8. **Wright LE**, Timmermann BN, Funk JL. Differential effects of medicinal Zingiberaceae on the prevention of bone loss. American Society of Pharmacognosy Annual Meeting, Honolulu, HI, June 2009.
9. **Wright LE**, Beischel Frye J, Timmermann BN, Funk JL. Effects of medicinal Zingiberaceae on bone loss in musculoskeletal disease. North American Research Conference on Complementary & Integrative Medicine, Minneapolis, MN, May 2009.
10. **Wright LE**, Beischel Frye J, Timmermann BN, Funk JL. Medicinal Zingiberaceae in the prevention of menopausal bone loss. Planta Medica. 74:1174, 2008.
11. **Wright LE**, Christian PJ, Rivera Z, Funk JL, Bouxsein ML, Hoyer PB. Skeletal deterioration in an ovary-intact mouse model of menopause. The Endocrine Society Annual Meeting, San Francisco, CA, June 2008.

RESEARCH SUPPORT

Ongoing Research Support

- BC134025 — Wright (PI) — 9/2014 – 9/2017
  Department of Defense (DoD) – Breast Cancer Research Program — $438,833
  Musculoskeletal complications and bone metastases in breast cancer patients undergoing estrogen deprivation therapy

  The objective of this grant is to evaluate the effects of aromatase inhibitor therapy on the musculoskeletal system by determining how estrogen depletion impairs muscle function and whether estrogen deprivation-induced bone loss can prime the bone microenvironment in ways that increase the progression of breast cancer bone metastases.

Completed Research Support

- IU Health Strategic Research Initiative in Oncology — Wright & Waning (co-PI's) — 11/2013 – 10/2014
  Melvin and Bren Simon Cancer Center, Bio-Plex Core Pilot Project Grant — $17,820
  Systemic factors responsible for cancer- and cancer therapy-induced ryanodine receptor 1 remodeling and muscle weakness

  The goal of this project was to identify systemic factors and signaling molecules responsible for maladaptive biochemical modifications to a critical calcium channel in skeletal muscle (RyR1), which leads to muscle weakness during cancer therapy-induced bone loss.

- PC101890 — Wright (PI) — 6/2012 – 5/2014
  Department of Defense (DoD) – Prostate Cancer Research Program — $123,463
  Mechanisms of radiation-induced bone loss and effects on prostate cancer bone metastases

The main objective of this study was to elucidate the mechanisms of radiation-induced bone loss and to determine how radiation exposure alters the bone microenvironment to increase the progression of prostate cancer bone metastases.

- F31 AT004875-04 Wright (PI) 9/2008 – 5/2012
  National Institutes of Health (NIH) $146,588
  National Center for Complementary and Alternative Medicine (NCCAM)
  Ruth L. Kirschstein National Research Service Award (NRSA)
  Ginger extracts in the prevention of metabolic bone disease

  This was an individual fellowship training grant supporting four years of doctoral training in physiological sciences. Specifically, this grant supported my dissertation research on the bone-sparing effects of natural product-derived compounds in translational models of osteoporosis and lytic breast cancer bone metastases.

REFERENCES

- **Theresa A. Guise, M.D.**
  Professor
  Indiana University
  Department of Medicine
  Division of Endocrinology
  980 West Walnut Street
  Walther Hall R3, #C132
  Indianapolis, IN 46202, USA
  TELE 1-317-278-6014
  FAX 1-317-278-2912
  tguise@iu.edu

- **Andrew R. Marks, M.D.**
  Professor
  Chair of Physiology
  Columbia University
  Department of Physiology
  630 West 168th Street
  New York, NY 10032, USA
  TELE 1-212-305-3512
  FAX 1-212-305-3475
  arm42@columbia.edu

- **Janet L. Funk, M.D.**
  Associate Professor
  University of Arizona
  Department of Medicine
  Endocrinology Section
  1656 East Mabel Street
  PO Box 245218
  Tucson, AZ 85724, USA
  TELE 1-520-626-3242
  FAX 1-520-626-3644
  jfunk@u.arizona.edu

You have been approved for NIH LRP funding!

lrp@nih.gov

Fri 7/17/2015 3:02 AM

To:Wright, Laura E <laewrig@iu.edu>;

Dear Laura Wright:

Congratulations! Your application to the National Institutes of Health (NIH) Clinical Loan Repayment Program (LRP) was approved for funding by National Cancer Institute (NCI). Your contract is for a period of two years. NO ACTION IS NEEDED TO ACCEPT THIS AWARD. However, if you decide not to participate in the program, please contact us at lrp@nih.gov.

We have set up a personalized online account for you to review and you can access your secure online account at https://www.lrp.nih.gov/LRPPortal. Your username (email address) and password are the same as used for your LRP application. Please login now and carefully review the important information concerning your obligations and responsibilities under the LRP contract. In addition to repaying your loan, NIH also pays the IRS an amount equaling 39 percent of your loan payment to cover the tax burden associated with this award. You will be responsible for any additional tax burden over the 39 percent. After year-end you will receive a Form 1099 tax form reporting our payments.

Accepting the LRP award binds you to the terms of the contract. If you will not be able to fulfill your responsibilities outlined in the contract for the entire term of your contract, you must decline the award in writing within 48 hours of receiving this email (see Section E – Contract Termination of the LRP contract). If you have questions regarding your commitment under this program, please contact the LRP Information Center at (866) 849-4047.

YOUR SERVICE OBLIGATION
By accepting the NIH LRP Award, you agree to continue performing the research outlined in your application for your current employer during the term of the contract. If you change research projects, supervisors, or institutions during the contract period, you are required to notify our office immediately. Your failure to notify us or failure to provide the required materials may result in termination of your contract.

YOUR LOAN PORTFOLIO
You can view your loan portfolio by accessing your secure online account at https://www.lrp.nih.gov/LRPPortal. If you have any concerns or believe your loan information is incomplete or incorrect, you must advise us by email at lrp@nih.gov within seven (7) days after receipt of this email. If you fail to notify us and later discover inconsistencies or omissions, we may not be able to reconcile or resolve them.

Our principal means of contacting you will be via your secure online account and email. Please make certain you login to your online account often and keep your contact information current. If you have any questions about your participation in the LRP, please contact our Information Center at (866) 849-4047 or at lrp@nih.gov.

Sincerely,

NIH Division of Loan Repayment
www.lrp.nih.gov

June 1, 2015

Indiana University
980 West Walnut Street, Walther Hall R3 Room C122, Indianapolis, IN 46202 USA

Dear Laura Wright,

We are delighted to inform you that you have been selected to receive an ASBMR Harold M. Frost Young Investigator Award to attend the 45th ORS International Sun Valley Workshop on Musculoskeletal Biology in Sun Valley, Idaho, USA, August 2-5, 2015. Congratulations!

The American Society for Bone and Mineral Research and the Sun Valley Meeting organizers honor Harold Frost each year by offering these young investigator awards in his name. As a mentor to countless clinicians and basic scientists, Harold Frost influenced many young scientists and had a profound impact on the direction of skeletal biology and metabolic bone disease research.

As the recipient of this travel award, you will receive $1,500 at the meeting. You are, however, expected to make your own arrangements for travel and accommodations. Travel and accommodation information are available on the Sun Valley Workshop website. You will also be required to present your research in a 15 minute talk from the podium at the meeting. As an award recipient, you will be registered automatically to attend the ORS Sun Valley workshop. If you are an ORS member you will not receive an invoice; registration is complimentary. If you are NOT an ORS member you will be required to pay a $75 registration fee, invoice will be emailed to you next week by the ORS office. However if you are not a current member but decide to join now, the registration fee can be waived.

Please note: Your award will be presented to you during a special session at the meeting. The Sun Valley Meeting organizers will be contacting you with further details. However, you should be aware that this year the organizers are requesting that all talks by awardees be previewed by our young investigator mentor, Dr. Lorena Havill. Therefore, we will be requesting that you submit your slide set for review to Lorena Havill (lorenabird@gmail.com) by **July 14.**

Please confirm by Friday, June 5th that you accept this award and can attend the 45th ORS International Sun Valley Workshop on Musculoskeletal Biology in Sun Valley, Idaho, USA on August 2-5, 2015.

For more information or if you have any questions, please contact ORS office at lewsza@ors.org or by telephone at +1 (847) 430-5022.

We look forward to seeing you in Sun Valley, and again, congratulations for this accomplishment!

Sincerely,

Roland Baron, DDS, Ph.D.
ASBMR President

David B. Burr, Ph.D.
Sun Valley Organizer

cc: Ann Elderkin, *ASBMR, Executive Director*

Letrozole and Ovariectomy Cause Bone Loss, Muscle Weakness and Increased Breast Cancer Bone Metastases in Mice

L.E. Wright[1], A.A. Harhash[1], D.L. Waning[1], K.S. Mohammad[1], A.R. Marks[2], T.A. Guise[1]

[1]Department of Medicine, Division of Endocrinology, Indiana University, Indianapolis, IN, USA
[2]Department of Physiology, Columbia University, New York, NY, USA

Adjuvant endocrine therapy using an aromatase inhibitor (AI) is a standard treatment for postmenopausal women with estrogen receptor (ER)-positive breast cancer. Unfortunately, 50% of women treated with an AI develop musculoskeletal complications. Previous studies in our laboratory have demonstrated bone loss and muscle weakness in ovariectomized (OVX) mice. We therefore hypothesized that complete estrogen deprivation using the AI letrozole would cause more profound muscle weakness and bone loss than OVX alone, and that this high bone turnover state could accelerate the progression of breast cancer bone metastases and negatively impact muscle function.

To test this, four-week female athymic nude mice underwent OVX or sham surgery and were treated daily with vehicle or AI (10µg/day; n=20/group). Two weeks after surgery and onset of treatment, bone mineral density was reduced in OVX-AI mice relative to vehicle-shams ($p<0.01$) as assessed by dual energy X-ray absorptiometry. Using bone micro-computed tomography (SCANCO viva40CT), trabecular bone volume fraction (BV/TV) of the proximal tibia was reduced by 53% is OVX-vehicle mice ($p<0.001$) and by 67% in OVX-AI mice ($p<0.001$) relative to vehicle-sham.

After confirming bone loss, the same animals were inoculated with ER-negative MDA-MB-231 human breast cancer cells into the left cardiac ventricle and were followed for osteolytic lesion formation (n=10-15/group). Since MDA-MB-231 is ER-negative, effects of complete estrogen deprivation should be indirect. Five weeks after inoculation, osteolytic lesion area was larger in OVX-AI mice relative to sham-vehicle ($p=0.0215$), while OVX or AI alone did not alter lytic lesion area. Skeletal muscle function was assessed by ex vivo measurement of maximal contractile specific-force of the extensor digitorum longus muscle. At 200Hz maximal contractile force in sham-letrozole and OVX-vehicle mice was reduced by 7% ($p<0.05$) and reduced by 12% in OVX-AI mice ($p<0.001$) relative to sham-vehicle.

Our murine studies confirm that AI treatment induces bone loss and skeletal muscle weakness, recapitulating effects in cancer patients. As hypothesized, the severe bone loss resulting from AI-induced estrogen depletion may prime the bone microenvironment for the development of breast cancer metastases to bone and potentiate muscle weakness. This model serves as an excellent tool to study the mechanisms of underlying musculoskeletal defects in cancer patients and assess potential therapeutics.

Bone Loss Due to Complete Estrogen Deprivation Causes Muscle Weakness and Increased Progression of ER-Negative Breast Cancer in Bone

Laura E. Wright[1], David L. Waning[1], Ahmed A. Harhash[1], Khalid S. Mohammad[1], Andrew R. Marks[2], Theresa A. Guise[1]

[1]Department of Medicine, Division of Endocrinology, Indiana University, Indianapolis, IN, USA
[2]Department of Physiology, Columbia University, New York, NY, USA

Adjuvant endocrine therapy using an aromatase inhibitor (AI) is a standard treatment for postmenopausal women with ER-positive breast cancer. Unfortunately, up to 50% of women treated with an AI develop muscle weakness, bone loss and joint pain that result in treatment discontinuation. Previous studies in our laboratory have demonstrated bone loss and muscle weakness in ovariectomized (OVX) mice. We therefore hypothesized that the combination of AI-OVX would cause more profound estrogen deprivation and bone loss than OVX alone, and that this high bone turnover state could alter the bone microenvironment in ways that accelerate the progression of breast cancer growth in bone and exacerbate muscle weakness systemically.

Four-week female athymic nude mice underwent OVX or sham surgery and were treated daily with vehicle or AI (10µg/day; n=20/group). Three weeks after surgery and onset of treatment, serum levels of 17β-estradiol in OVX-AI mice were reduced by 56% ($p<0.01$; Calbiotech ELISA) and trabecular bone volume fraction at the proximal tibia was reduced by 67% ($p<0.001$; SCANCO viva40CT) relative to vehicle-sham. After confirming estrogen deficiency and bone loss, the same animals were inoculated with ER-negative MDA-MB-231 human breast cancer cells into the left cardiac ventricle and followed for cancer progression in bone. Since MDA-MB-231 cells are ER-negative, effects of estrogen deprivation on the tumor should be indirect and attributed to the bone microenvironment. Five weeks after inoculation, osteolytic lesion area increased by 110% ($p<0.01$, X-Ray) and tumor burden in bone assessed by histology was increased by 87% ($p<0.01$) in OVX-AI mice relative to sham-vehicle. Furthermore, ex vivo maximal contractile force of the extensor digitorum longus muscle was significantly reduced in OVX-AI mice (-12%, $p<0.001$) relative to sham-vehicle.

Our murine studies confirm that AI treatment induces bone loss and skeletal muscle weakness, recapitulating effects in cancer patients. As hypothesized, the severe bone loss resulting from AI-induced estrogen depletion may prime the bone microenvironment for the development of breast cancer metastases to bone and potentiate muscle weakness. This model serves as an excellent tool to study the mechanisms of underlying musculoskeletal defects in cancer patients and to assess potential therapeutics. Ongoing studies will evaluate whether protection of bone with bisphosphonates can prevent AI-induced musculoskeletal complications in our model of breast cancer bone metastases.

Murine models of breast cancer bone metastasis

Laura E. Wright,[1]* Penelope D. Ottewell,[2] Nadia Rucci,[3] Olivier Peyruchaud,[4,5] Gabriel M. Pagnotti,[6] Antonella Chiechi,[1] Jeroen T. Buijs,[7] Julie A. Sterling[8,9]

[1]Indiana University, Department of Medicine, Division of Endocrinology, Indianapolis, Indiana, USA.
[2]University of Sheffield, Department of Oncology, Mellanby Center for Bone Research, Sheffield, UK.
[3]Department of Biotechnological and Applied Clinical Sciences, University of L'Aquila, L'Aquila, Italy.
[4]INSERM, UMR_S1033, Lyon, France.
[5]Université Claude Bernard Lyon-1, Lyon, France
[6]Stony Brook University, Department of Biomedical Engineering, Stony Brook, New York, USA.
[7] Department of Urology, Leiden University Medical Center, Leiden, The Netherlands.
[8]Vanderbilt University, Department of Medicine, Division of Clinical Pharmacology, Nashville, Tennessee, USA.
[9]Department of Veterans Affairs, Tennessee Valley Healthcare System, Nashville, Tennessee, USA.

***To whom correspondence may be addressed:**
Laura E. Wright, Ph.D.
980 West Walnut Street
Walther Hall R3, Room C132
Indianapolis, IN 46202, USA
Tele: 1.317.278.7785
Fax: 1.317.278.2912
Email: laewrig@iu.edu

Running title: Modeling breast cancer bone metastases in mice

Abstract

Bone metastases cause significant morbidity and mortality in late-stage breast cancer patients and are currently considered incurable. Investigators rely on translational models to better understand the pathogenesis of skeletal complications of malignancy in order to identify therapeutic targets that may ultimately prevent and treat solid tumor metastasis to bone. Many experimental models of breast cancer bone metastases are in use today, each with its own caveats. In this methods review we characterize the bone phenotype of commonly utilized human- and murine-derived breast cell lines that elicit osteoblastic and/or osteolytic destruction of bone in mice, and report methods for optimizing tumor-take in murine models of bone metastasis. We then provide protocols for four of the most common xenograft and syngeneic inoculation routes for modeling breast cancer metastasis to the skeleton in mice, including the intra-cardiac, intra-arterial, orthotopic, and intra-tibial methods of tumor cell injection. Recommendations for *in vivo* and *ex vivo* assessment of tumor progression and bone destruction are provided, followed by discussion of the strengths and limitations of the available tools and translational models that aid investigators in the study of breast cancer metastasis to bone.

Introduction

Breast cancer metastasis to the skeleton and subsequent bone destruction often result in severe bone pain, fragility fractures, nerve compression syndromes, and hypercalcemia of malignancy resulting in significant morbidity and mortality.[1,2] Elucidation of the molecular mechanisms that mediate breast cancer bone metastases and cancer-induced bone destruction has begun to reveal potential therapeutic targets that may lead to improved patient survival and quality of life; however further investigation is necessary to address this currently irreversible late-stage complication of malignancy. Therefore, it is of utmost importance for investigators to establish well-characterized *in vivo* models of breast cancer bone metastasis.

Unlike the study of postmenopausal osteoporosis where the ovariectomy model is the clear FDA-mandated choice,[3] there are numerous murine models of breast cancer metastasis to bone, each with its own benefits and limitations. Because spontaneous metastasis to the skeleton from primary tumors in animals is rare, and no single model reproduces all of the genetic and phenotypic changes of human breast cancer bone metastasis, researchers must select a model or combination of models that best suits the aspect of the metastatic disease that they wish to investigate. Here we 1) identify the most commonly utilized breast cancer cell lines that elicit osteolytic, osteoblastic, or mixed phenotypes in bone, 2) provide protocols for tumor cell inoculation routes that model metastatic disease in the skeleton, and 3) explore methods for the post-inoculation monitoring of breast cancer progression in bone.

Modeling osteolytic breast cancer bone metastases

Inoculation of bone trophic tumor cells directly into the blood stream provides a useful tool for investigating the processes associated with breast cancer cell homing, colonization, and subsequent metastatic tumor growth and osteolytic lesion formation in bone. Intra-cardiac inoculation of human triple negative MDA-MB-231 adenocarcinoma cells into immune compromised mice (i.e., BALB/c nude, MF1 nude, NOD/SCID) results in tumor cell

dissemination through the arterial vascular system and homing primarily to long bones, spine, jaw, and lungs (**Figure 1A; Table 1**).[4,5] In syngeneic tumor models where murine-derived cell lines are inoculated into a murine host, a similar metastatic profile can be observed following intra-cardiac injection of 4T1 or PyMT MMTV mammary cancer cells into immune competent BALB/c or FVB/N mice, respectively (**Table 1**).[6,7]

Visceral metastases, particularly to the lung, can significantly shorten the lifespan of a mouse and thus limit the experimental timeframe during which skeletal metastases can be studied *in vivo*. MDA-MB-231 and 4T1 cell lines have therefore been manipulated in the laboratory to produce bone-seeking sub-lines that favor homing to and colonization of mouse tibiae and femurs with a reduced propensity to metastasize to the lung. Bone-seeking sub-lines, often referred to in the literature as MDA-MB-231-B02, MDA-MB-231-1833, MDA-MB-231-B, MDA-IV, and MDA-MB-231-bone, form tumors in the long bones of up to 90% of mice following intra-cardiac inoculation in BALB/c nude mice.[8-12] Intra-cardiac inoculation of the sub-line 4T1-2 cells into BALB/c mice results in bone metastases in 70-80% of animals (**Table 1**).[13]

Direct intra-tibial injection of a number of breast cancer cell lines including MDA-MB-231, MDA-MB-436 and SUM1315 into immunocompromised mice, and 4T1 and PyMT MMTV cell lines into immune competent BALB/c and FVB/N mice results in the development of osteolytic mammary tumors in bone with minimal impact outside of bone marrow engraftment (**Figure 1B; Table 1**).[7,14,15] The intra-tibial model bypasses the early stages of metastasis including homing to the bone microenvironment and is therefore useful for a more direct assessment of tumor-bone interactions, particularly when interested in studying genetic manipulations of the host or tumor cells of interest.

Intra-cardiac, intra-arterial, and intra-tibial inoculation of cancer cells provide useful tools for examining the later stages of breast cancer bone metastasis; however, these aforementioned models do not permit investigation into the stages that precede the colonization of breast cancer in bone, including primary tumor growth or the dissemination of tumor cells

through intravasation. The 4T1 mouse mammary cancer cell line was derived from a BALB/c spontaneous mammary carcinoma,[16] and orthotopic inoculation of 4T1 cells into the mammary fat pad of BALB/c mice results in spontaneous metastasis to lungs (~60% of mice) and bone (~20-30% of mice; **Table 1**).[17] Incidence of bone metastasis can be increased to 50-70% by utilizing the bone-seeking 4T1-2 sub-line.[18,19] This syngeneic model has the benefit of utilizing an immune competent mouse, however it lacks the clinical applicability achieved by the use of a human-derived breast cancer cell line.

Recently, it was shown that orthotopic inoculation of luciferase-transduced murine invasive lobular breast carcinoma cells (KEP cells) resulted in formation of bone metastases in the appendicular and axial skeleton within 3 weeks after resection of the orthotopic tumor with minimal lung involvement in BALBc nude mice (**Table 1**).[20] Although MDA-MB-231 do not metastasize to murine bone from the orthotopic site in BALB/c nude and NOD SCID mice, distant metastases at skeletal sites were observed when using NSG mice,[21] suggesting the importance of NK cells in regulating the metastatic process.

Spontaneous metastasis of an orthotopic human breast cancer tumor to bone can be achieved in an immune compromised mouse using a unique model that incorporates human-derived bone X-plants. In recent studies, orthotopic inoculation of human-derived SUM-1315 or MDA-MB-231-IV cells into the mammary fat pad of NOD SCID mice four weeks following ectopic implantation of human bone resulted in spontaneous metastasis of human breast cancer cells specifically to the human bone grafts in 40-60% of animals (**Table 1**).[22,23]

Modeling osteoblastic breast cancer bone metastases

Although patients with breast cancer usually develop osteolytic bone metastases, as many as 25% will present with osteoblastic bone metastases.[24] The human breast cancer cell lines ZR-75-1 and MCF-7 can be utilized to establish an osteoblastic bone metastatic phenotype in mice.

ZR-75-1 cultures were initially derived from a malignant ascetic effusion in a 63-year-old Caucasian female with ductal carcinoma. ZR-75-1 cells possess receptors for all four classes of steroid hormones and are thus responsive to estradiol stimulation.[25,26] Mice inoculated via intra-cardiac route with ZR-75-1 cells develop osteoblastic bone metastases in the long bones, however bone metastases are typically not detectable by X-ray for 12-25 weeks post-inoculation (**Figure 1C; Table 2**).

Human MCF-7 breast cancer cells were derived from a metastatic pleural effusion in a 69-year-old Caucasian female with breast carcinoma.[27] MCF-7 cells retain characteristics of differentiated mammary epithelium and possess estrogen receptors.[27,28] Intra-cardiac inoculation of MCF-7 cells in immune compromised mice results in mixed osteolytic/osteoblastic bone metastases in the long bones after 20-25 weeks (**Table 2**). In order to speed metastatic progression, the MCF-7 cell line has been stably transfected with the oncogene Neu and this cell line establishes mixed osteolytic and osteoblastic bone metastases in immunocompromised mice within 10-12 weeks after intra-cardiac inoculation.[29] Because ER+ MCF-7 cell growth is estrogen dependent, mice should be implanted subcutaneously with slow-release estradiol pellets (0.25mg) prior to intra-cardiac tumor cell inoculation in order to more closely mimic a pre-menopausal tumor environment and speed the progression of tumor growth in bone.[30,31] MCF-7 and MCF-7/Neu cells are also commonly utilized to establish bone lesions in mice via the intra-tibial inoculation route, with lesions developing in a shorter timespan of 1-3 weeks post injection (**Figure 1D; Table 2**). Estradiol supplementation is typically not introduced when MCF-7 cells are directly implanted into bone.

Materials and Methods

This section begins by detailing recommendations for the preparation of breast cancer cells and pre-operative care instructions for the handling of mice prior to inoculation. Four of the most commonly utilized cell inoculation routes resulting in breast cancer bone metastases are

then described, including lists of necessary materials for each technique. Recommendations for the post-inoculation monitoring of animals and assessment of tumor progression in bone *in vivo* and *post mortem* are then described.

Breast cancer cell preparation

Manufacturer specifications should guide the user as to the appropriate growth conditions for the cell line of interest. As a general rule for all tumor cell inoculation routes, prepare cells from a fresh batch of low passage number. Split cells 1-2 days prior to the injections such that they reach ~80% confluence on the day of inoculation. Overcrowding of tumor cells can affect their metastatic potential *in vivo* therefore cell confluence prior to inoculation must be monitored judiciously. Wash flasks with the appropriate cold cell culture media or PBS, trypsinize (0.15% Trypsin-EDTA) and remove cells with ice-cold media containing 10% FBS. Centrifuge (200 x g, 5min) and suspend the cell pellet in ice-cold PBS for quantitation. Re-suspend the cells at the desired concentration (**Table 3**) in cold PBS and keep the cell suspension for no more than 30min on ice until the moment of inoculation. Prepare cells in small batches (enough for 1-2 cages or 5-10 animals) and keep on ice to minimize clumping and risk of embolism during the *in vivo* inoculation. Due to volumetric limitations of the mouse circulation, 100µL is the recommended injection volume using the intra-cardiac or intra-arterial routes.

Reagents for tumor cell preparation

1) PBS (without Ca^{2+} and Mg^{2+})
2) 0.15% Trypsin EDTA
3) Cold DMEM (or other media) with 10% FBS

Pre-operative management of mice

For the intra-cardiac, intra-arterial, and intra-venous metastasis models, mice are inoculated between 4-6 weeks of age, as tumor-take is drastically reduced after 6 weeks. For the intra-tibial injection, 6-8 week old mice are typically used, as tibiae of younger mice are small and difficult to inject accurately. A ketamine/xylazine cocktail (100mg/kg and 10mg/kg, respectively) or isoflurane (2.5% isoflurane at 2-3L/min O_2) may be utilized for anesthesia during the inoculation of tumor cells depending on the laboratory's preference. Many groups however experience improved survival rates following intra-cardiac inoculation with use of isoflurane (vs. ketamine/xylazine), likely due to increased vascular tone and body temperature.

Cellular inoculation routes for modeling breast cancer bone metastases in mice

1) Intra-cardiac inoculation of breast cancer cells

Once a mouse has been properly anesthetized and is unresponsive to pinch, place it on a sterile surface in supine position ensuring that the vertebral column is straight. Tape the forelimbs away from the torso at a slightly angled and upwards position (**Figure 2A**). Prior to inoculation, clean the chest of the animal thoroughly with betadine and wipe with an alcohol pad, or as per the institutional standard operating procedures. Once the chest has been sterilized, gently place one hand on the chest of the mouse to tighten the skin and mark the top of the sternum and the xyphoid process (distal sternum) with a permanent marker (**Figure 2A**). Make a 3rd mark in the middle of these two landmarks and slightly to your right (animal's left) just over the heart in the third intercostal space (**Figure 2A**). This mark identifies the location of the left cardiac ventricle where you will insert the needle for tumor cell inoculation.

With intra-cardiac inoculation, prepare the needle by leaving a small air space in the top of the syringe before slowly drawing up the desired volume of cell suspension into the syringe (**Figure 2B**). This air space will permit a small influx of bright red oxygenated blood into the syringe hub when properly inserted into the left cardiac ventricle. Hold the skin of the mouse tight with one hand, and insert the needle perpendicularly into the middle marking (**Figure 2C**).

When the needle has entered the left cardiac ventricle, watch for the pulse of blood to appear in the hub of the needle. The appearance of air bubbles in the needle hub upon insertion indicates that it has likely entered the lungs and will need to be removed and repositioned. If you do not see a red pulse of blood in the needle hub but are confident that you are in the correct location, you can pull up slightly on the syringe plunger to verify your position in the cardiac ventricle. If there is still no visible red pulse, the needle can be slowly and slightly adjusted up or down. When small adjustments are futile, remove and reposition the insertion point completely or set the mouse aside temporarily. Extended anesthesia can cause vasoconstriction and reduce the animal's blood pressure such that the pulse of blood into the needle's hub becomes less noticeable.

Once the needle is correctly positioned in the left cardiac ventricle, inject the cell suspension slowly into the left ventricle being careful not to move the needle or press it deeper into the thoracic cavity. Keep a close eye on the cell suspension in the syringe and do not inject the air bubble at the top of the syringe (**Figure 2B**). As soon as the cells have been inoculated, quickly remove the needle, apply slight pressure at the injection site for a few seconds, and place the mouse on a heating pad until fully awake. Once mice have fully recovered, monitor their behavior for 24h and watch for potential signs of embolism or distress.

Materials for intra-cardiac inoculation

1) Anesthetized mouse (immune compromised if using human cells)
2) Cellular suspension
3) 0.5 - 1cc insulin syringe, 27-29G, 0.5 inch
4) Surgical tape
5) Betadine and alcohol swabs
6) Permanent marker
7) Water recirculating heating pad

2) Intra-arterial inoculation of breast cancer cells in the tail

Once a mouse has been anesthetized with isoflurane, place it on a sterile surface in supine position and tape the torso of the mouse to the table for stability. Use a heating pad or lamp to dilate the vessels within the tail for 2-3 minutes in order to facilitate greater ease of inoculation. Alternatively, the tail can be placed in warm water (30-35^{o}C). Using an alcohol pad, disinfect the tail vigorously, which will also help dilate the vessels within the tail and facilitate inoculation. Keep the tail clinched between the forefinger and thumb, and insert the needle (beveled edge facing up) horizontally across the proximal section of the tail into the artery (**Figure 3**). Once the needle has entered the artery, the opposite hand is used to retract the syringe plunger slightly to inspect for a tight fitting within the artery and inspect the barrel of the syringe for a small amount of blood, which should appear at the needle hub. This will not occur if the needle has not breached the epithelial membrane of the artery or if the syringe has protruded through the artery. Once the syringe is properly seated within the artery, depress the plunger slowly in order to minimize cell lysis resulting from fluid shear. The needle should ideally pierce the artery just once in order for the cell bolus to be delivered in its entirety. However, when small adjustments are futile, remove the needle completely, and reposition the insertion point proximally to the initial site of injection. Once mice have fully recovered, monitor their behavior for 24h and watch for potential signs of embolism, pain, or distress.

Materials for intra-arterial tail inoculation

1) Anesthetized mouse (immune compromised if using human cells)
2) Cellular suspension
3) 0.5 - 1cc insulin syringe, 27-29G, 0.5 inch
4) Surgical tape
5) Betadine and alcohol swabs

6) Water recirculating heating pad

3) Orthotopic (mammary fat pad) inoculation of breast cancer cells

Place an anesthetized mouse in supine position on a sterile surface and tape the forelimbs and hind limbs away from the torso (**Figure 4A**). Prior to inoculation, clean the inguinal surface of the animal thoroughly with betadine and wipe with an alcohol pad or as per the institutional standard operating procedures. Using sterile surgical instruments, create a small incision in the skin adjacent to the 4th mammary fat pad (**Figure 4B,C**). Insert the needle into the 4th mammary gland fat pad and slowly inoculate the tumor cell suspension (**Figure 4D,E; Video 1**). The 4th mammary gland fat pad is located at the intersection of three prominent blood vessels (**Figure 4C**). As with all techniques, it may be important for investigators to practice and familiarize themselves with the necessary anatomical landmarks prior to initiation of a multi-animal study. After the injection of cells, close the wound with 4-6 unconnected sutures, administer an analgesic as per institutional guidelines, and place the mouse on a heating pad until fully awake.

In order to limit the occurrence of spontaneous tumor metastases to the lungs when using murine-derived cells (e.g., 4T1), primary tumors can be surgically resected from anesthetized mice when tumors reach ~1cm^3. Animals can then be followed for 3-4 additional weeks for the development of bone metastases.

Some laboratories have reported that orthotopic implantation of the human-derived breast cancer cell lines SUM-1315 and MDA-MB-231-IV into immune compromised mice can elicit spontaneous metastasis to bone when preceded by engraftment of human bone plugs.[22,23] In this model, 5mm bone biopsy cores obtained from human femoral heads (within 2-4 hours of removal from the patient) can be implanted under the skin on the posterior surface of the animal prior to tumor cell inoculation in the mammary fat pad. Four weeks after bone plug implantation, the human bone grafts become vascularized and bone marrow resembles that of normal

bone.[22,23] Orthotopic injection of human-derived tumor cells can then proceed as described, and the human bone plugs are then excised at the termination of the study (~8-14 weeks) and evaluated for the presence of breast cancer metastases.

Materials for orthotopic inoculation

1) Anesthetized mouse (immune compromised if using human cells)
2) Cellular suspension
3) 0.1cc Hamilton syringe, 25-27G, 0.5 inch
4) Tape
5) Betadine and alcohol swabs
6) Sterile scissors and forceps
7) Suture
8) Water recirculating heating pad
9) Analgesic

4) Intra-tibial inoculation of breast cancer cells

Prepare a syringe with the desired tumor cell suspension and set aside until ready to inject. After sterilizing the hind limbs, bend the knee to nearly 90° (**Figure 5A**). While holding the hind limb between the thumb and index finger, locate the patellar ligament between the knee and the tibia, which should be visible through the skin as a white longitudinal structure. Some laboratories choose to make a 2-3mm incision through the skin on the knee to more easily visualize the tibia and patellar ligament however with practice this may not be necessary. Holding the needle parallel to the tibia in the dominant hand, push the needle through the center of the patellar ligament and into the proximal end of the tibia (**Figure 5B**). Resistance will be felt once the needle reaches the bone. Twist the needle slightly to drill through the growth plate until the needle can be felt giving way. Once inserted into the bone approximately 2-3mm, attempt to

move the needle slightly from side to side. When the needle is in the tibia, it will not be easily moved. If it moves freely from side to side, the needle is most likely embedded primarily in muscle and the insertion will need to be repeated. When the needle is accurately placed inside the marrow cavity of the tibia, inject the cell suspension slowly and then withdraw the needle using the same drilling motion used to enter the bone. In the event that the needle becomes clogged when penetrating or drilling through the top of the tibia, remove the original needle and re-insert a new needle, trying to follow the route created by the first needle. Once complete, use the same technique to inject the contralateral tibia with sterile PBS or desired vehicle to serve as a sham control. Bleeding rarely occurs; however if blood does appear, apply pressure at the site. Administer an analgesic as per institutional guidelines, place the mouse on a heating pad, and monitor until active.

While cells can be inoculated into the tibia at any age, it is more difficult to penetrate the tibia in older animals once the growth plates have mineralized (>8 weeks old). On the other hand, very young mice can present injection difficulties due to the small size of the tibia; most laboratories therefore select 4-6 week-old mice for the intra-tibial inoculation route. If the mouse strain selected is furred, shave or wet the hair on the hind limb prior to the inoculation in order to better visualize the patellar ligament and other landmarks in the knee.

Materials for intra-tibial inoculation

1) Anesthetized mouse (immune compromised if using human cells)
2) Cellular suspension
3) 0.1cc Hamilton syringe, 25-27G, 0.5 inch
4) Betadine and alcohol swabs
5) Water recirculating heating pad
6) Analgesic

Assessment of tumor progression in bone

Throughout a bone metastasis experiment, mice should be monitored daily for changes in activity levels, mobility, and onset of cachexia, which is a paraneoplastic syndrome characterized in mice by loss of body weight, muscle atrophy and weakness, arched appearance, and lethargy.[32,33] Mice should be euthanized when >10-20% body weight is lost, tumor progression impairs mobility (e.g., long bone fracture, head-tilt, paraplegia), or an animal appears to be in respiratory distress. A sub-set of mice may require euthanasia sooner than other mice in large studies. With the exception of survival studies, it is important that mice be euthanized on the same day or as close to the same day as possible such that the experimental timeframe is identical for all mice, thus permitting an accurate comparison of tumor progression between groups.

Osteolytic lesion area and abnormal bone remodeling can be visualized and assessed weekly *in vivo* using a cabinet X-Ray machine (**Figure 6A; Table 4**). Because X-Ray analysis is an assessment of overt osteolytic lesion formation and provides only indirect information on tumor cell growth, cancer cell lines are commonly transfected with bioluminescent proteins permitting *in vivo* visualization and quantitation of tumor growth at metastatic sites using bioluminescence imaging (BLI) (**Table 4**).[11,20,34] BLI serves as an ideal complement to X-Ray analysis of osteolysis, as it provides information on the presence of extra-skeletal metastases as well as micrometastases in bone, which precede bone destruction.

At the termination of the study, mice should be subjected to necropsy and examined closely for gross evidence of metastatic foci outside of bone. For an intra-cardiac tumor inoculation study, evidence of tumor growth in the mediastinum surrounding the heart indicates that tumor cells were not accurately injected into the left cardiac ventricle and the mouse should be excluded from the study. Fix all vital organs for future analysis. Carefully cut and scrape away skeletal muscle from the forelimbs, hind limbs, and vertebral column, and fix the skeletal samples. Prior to decalcification of the bones, high resolution *ex vivo* bone microcomputed

tomography (μCT) can be performed to assess osteolytic or osteoblastic bone destruction and BV/TV at the distal femur, proximal tibia, or lumbar vertebrae (**Figure 6B**).

Following decalcification, paraffin-embedded bone should be sectioned and stained with hematoxylin/eosin (H&E), and tumor burden (mm^2) should be measured in long bones and spine using image analysis software (**Figure 6C**). Osteoblast numbers may also be quantitated in H&E stained sections. Histological sections should also be stained for tartrate resistant acid phosphatase (TRAcP) activity in order to assess the total osteoclast number relative to the bone surface and the osteoclast number at the bone and tumor interface, all of which are known to increase with cancer-induced osteolysis (**Figure 6D, Table 4**).[35,36] Finally, serum can be assayed for the presence of bone turnover markers, hormones, inflammatory factors, or growth factors of interest.

When applicable, quantification of spontaneous metastases to lung, liver, brain or adrenals can be performed in paraffin embedded organs collected at necropsy. For these analyses, 5μm sections can be cut every 200μm through the organ and stained with H&E. The number and area of metastatic foci for each section can then be determined using image analysis software, and results can be expressed as the total metastatic foci number per organ and as total metastatic area per organ.

Discussion

When considering skeletal metastasis models with the intention of studying breast cancer osteolysis, a common choice is the intra-cardiac injection of human breast cancer cells in immune compromised mice.[37-39] Alternatively, these human cells can be directly implanted into bone, bypassing earlier steps in the metastatic process. A benefit of the former model is that tumor cells detected in bone have themselves “seeded the soil,” thus replicating the more natural progression of disseminated tumor cells formation of micrometastases which progress in size over time, as occurs in humans. The necessity of using immune cell deficient mice when

inoculating human cell lines is typically seen as a limitation because it does not accurately model the immune competent human patient. It can however be seen as an advantage, as it eliminates possible confounding effects related to the animal's immune response and permits the study of human cells in a very permissive host environment.

The pathogenesis of breast cancer bone destruction in the intra-cardiac MDA-MB-231 model is relatively similar to the human condition. Upon inoculation, breast cancer cells circulate in the vasculature, home to the bone compartment, and micrometastases can be detected by BLI in distant skeletal sites in as early as one week after injection.[40] As the tumor cells proliferate in the bone microenvironment, tumor-derived osteolytic factors stimulate osteoclastic bone resorption and the development of bone lesions, which are quantifiable by X-Ray. The most substantial bone destruction tends to occur in the metaphyses of the distal femur and proximal tibia, likely due to the high vascularization and metabolic activity characteristic of these trabecular bone compartments.[41]

Estrogen receptor (ER)+ MCF-7 cells and triple negative MDA-MB-231 cells are two of the most commonly studied human breast cancer cell lines.[39] While ER+ primary tumors have a high propensity to metastasize to bone in patients,[42] ER+ MCF-7 cells are utilized less frequently in models of breast cancer bone metastasis, as tumor-take can be limited using the intra-cardiac inoculation route, and MCF-7 cells require a longer time to develop osteolytic and osteoblastic lesions.[43,44] In contrast, ER- MDA-MB-231 cells readily metastasize to bone and develop osteolytic lesions as early as 2-3 weeks post-inoculation.[38] In defense of the use of an ER- cell line, it should also be noted that there is a large discordance between the ER status of primary tumors and the ER status of the bone metastatic tumors in patients.[42]

The intra-tibial inoculation method is ideal for modeling the final stages of breast cancer bone metastasis and for studying direct interactions between tumor cells and the bone microenvironment without concerns about differential tumor-take from animal to animal. Murine-derived 4T1 cell proliferation in the tibia and subsequent development of osteolytic lesions can

occur with the injection of as few as 10,000 murine-derived cells. At higher cellular concentrations (50,000-200,000 cells), our laboratories have observed 4T1 cell metastasis to contralateral tibiae, femurs, forelimbs, and the lungs, often limiting the duration and utility of the model. As with all techniques presented here, it is recommended that investigators thoroughly characterize their cell line and inoculation route of choice by conducting dose response studies in order to establish the optimal protocols prior to embarking on large animal trials.

Inoculation of cancer cells into the tail vein is a well-established bone metastasis model for multiple myeloma.[45,46] Our laboratories and others have found that the injection of breast cancer cells into the tail vein results almost exclusively in lung metastases, with limited tumor take in bone.[47-48] When skeletal metastases are desired, we therefore recommend utilization of the tail artery as the tumor inoculation route for breast cancer models.[47-52]

In addition to specific limitations related to model choice discussed above, standard methodologies used by bone metastasis researchers to assess bone destruction and tumor burden have their own limitations. Osteolytic lesion area and tumor burden area in bone are typically assessed by measurement of X-Ray scan or by serial histological sectioning, respectively, and are thus merely two-dimensional approximations of three-dimensional tumors. Improvement in imaging has enhanced sensitivity of detection and yields more accurate quantification of metastases. Typically, bioluminescent imaging (BLI) using codon-optimized luciferase-labeled cells yield higher detection than fluorescent imaging (FLI) using GFP labeled cells.[53] Small animal imaging of bone has forged ahead with the development of high-resolution *in vivo* μCT scanners[54] in combination with BLI.[55] However, the bone metastasis research community has been slower to adopt such methodologies. One reason for this is that cumulative radiation exposure from CT scanners has been found to enhance metastases,[56] and thus could confound cancer metastasis models if radiation exposure is not monitored judiciously.

Despite their limitations and caveats, the established murine models of breast cancer bone metastases have proven to be excellent tools for the study of bone and cancer cross-talk

and for the evaluation of potential therapeutics that prevent cancer progression and disrupt the cycle of bone destruction driven by metastasis.

Multimedia

The following article documents and visually demonstrates intra-cardiac and intra-tibial inoculation of cancer cells in mice, and also demonstrates representative experimental endpoints of bone metastasis: http://www.jove.come/video/4260.

Acknowledgments

The authors wish to thank Alyssa Merkel and Kristin Kwakwa for capturing the photographs in Figures 2 and 5, and Johnny Ribeiro and Khalid Mohammad for their technical input on the orthotopic and intra-tibial models, respectively.

This work was supported by the Department of Defense Breast Cancer Research Program BC134025 (LEW), and by grants from INSERM (OP), the Comité Départemental de la Loire de la Ligue Contre le Cancer (OP), the Fondation ARC (OP), NIAMS AR43498 (GMP), the Department of Veterans Affairs 1I01BX001957 (JAS), and NCI 1R01CA163499 (JAS).

Conflict of Interest

The authors declare no conflict of interest.

References

1. Coleman RE. Skeletal complications of malignancy. *Cancer* 1997;**80**:1588-94.
2. Mundy GR. Metastasis to bone: causes, consequences and therapeutic opportunities. *Nat Rev Cancer* 2002;**2**:584-93.
3. Thompson DD, Simmons HA, Pirie CM, Ke HZ. FDA Guidelines and animal models for osteoporosis. *Bone* 1995;**17**:125S-33S.

4. Ottewell PD, Wang N, Brown HK, Reeves KJ, Fowles CA, Croucher PI, et al. Zoledronic acid has differential antitumor activity in the pre- and postmenopausal bone microenvironment in vivo. *Clin Cancer Res* 2014;**20**:2922-32.
5. Ottewell PD, Wang N, Brown HK, Fowles CA, Croucher PI, Eaton CL, et al. OPG-Fc inhibits ovariectomy-induced growth of disseminated breast cancer cells in bone. *Int J Cancer*. 2015 Jan 21. doi: 10.1002/ijc.29439. [Epub ahead of print]
6. Lee JH, Kim B, Jin WJ, Kim JW, Kim HH, Ha H, et al. Trolox inhibits osteolytic bone metastasis of breast cancer through both PGE2-dependent and independent mechanisms. *Biochem Pharmacol* 2014;**91**:51-60.
7. Werbeck JL, Thudi NK, Martin CK, Premanandan C, Yu L, Ostrowksi MC, et al. Tumor microenvironment regulates metastasis and metastasis genes of mouse MMTV-PymT mammary cancer cells in vivo. *Vet Pathol* 2014;**51**:868-81.
8. Pécheur I, Peyruchaud O, Serre CM, Guglielmi J, Voland C, Bourre F, et al. Integrin alpha(v)beta3 expression confers on tumor cells a greater propensity to metastasize to bone. *FASEB J* 2002;**16**:1266-8.
9. Ottewell PD, Deux B, Mönkkönen H, Cross S, Coleman RE, Clezardin P, et al. Differential effect of doxorubicin and zoledronic acid on intraosseous versus extraosseous breast tumor growth in vivo. *Clin Cancer Res* 2008;**14**:4658-66.
10. Kang Y, Siegel PM, Shu W, Drobnjak M, Kakonen SM, Cordón-Cardo C, et al. A multigenic program mediating breast cancer metastasis to bone. *Cancer Cell* 2003;**3**:537-49.
11. Wetterwald A, van der Pluijm G, Que I, Sijmons B, Buijs J, Karperien M, et al. Optical imaging of cancer metastasis to bone marrow: a mouse model of minimal residual disease. *Am J Pathol* 2002;**160**:1143-53.
12. Nutter F, Holen I, Brown HK, Cross SS, Evans CA, Walker M, et al. Different molecular profiles are associated with breast cancer cell homing compared with colonisation of bone: evidence using a novel bone-seeking cell line. *Endocr Relat Cancer* 2014;**21**:327-41.
13. Nasrazadani A, Van Den Berg CL. c-Jun N-terminal Kinase 2 Regulates Multiple Receptor Tyrosine Kinase Pathways in Mouse Mammary Tumor Growth and Metastasis. *Genes Cancer* 2011;**2**:31-45.
14. Fathers KE, Bell ES, Rajadurai CV, Cory S, Zhao H, Mourskaia A, et al. Crk adaptor proteins act as key signaling integrators for breast tumorigenesis. *Breast Cancer Res* 2012;**14**:R74.
15. Ottewell PD, Woodward JK, Lefley DV, Evans CA, Coleman RE, Holen I. Anticancer mechanisms of doxorubicin and zoledronic acid in breast cancer tumor growth in bone. *Mol Cancer Ther* 2009;**8**:2821-32.
16. Aslakson CJ, Miller FR. Selective events in the metastatic process defined by analysis of the sequential dissemination of subpopulations of a mouse mammary tumor. *Cancer Res* 1992;**52**:1399-1405
17. Abdelaziz DM, Stone LS, Komarova SV. Osteolysis and pain due to experimental bone metastases are improved by treatment with rapamycin. Breast Cancer Res Treat 2014;**143**:227-37.
18. Lelekakis M, Moseley JM, Martin TJ, Hards D, Williams E, Ho P, et al. A novel orthotopic model of breast cancer metastasis to bone. *Clin Exp Metastasis* 1999;**17**:163-70.
19. Withana NP, Blum G, Sameni M, Slaney C, Anbalagan A, Olive MB, et al. Cathepsin B inhibition limits bone metastasis in breast cancer. *Cancer Res* 2012;**72**:1199-209.
20. Buijs JT, Matula KM, Cheung H, Kruithof-de Julio M, van der Mark MH, Snoeks TJ, et al. Spontaneous bone metastases in a preclinical orthotopic model of invasive lobular carcinoma; the effect of pharmacological targeting TGFβ receptor I kinase. *J Pathol* 2015;**235**:745-59.

21. Iorns E, Drews-Elger K, Ward TM, Dean S, Clarke J, Berry D, et al. A New Mouse Model for the Study of Human Breast Cancer Metastasis. *PLoS One* 2012;**7**:e47995.
22. Kuperwasser C, Dessain S, Bierbaum BE, Garnet D, Sperandio K, Gauvin GP, et al. A mouse model of human breast cancer metastasis to human bone. *Cancer Res* 2005;**65**:6130-8.
23. Holen I, Nutter F, Wilkinson JM, Evans CA, Avgoustou P, Ottewell PD. Human breast cancer bone metastasis in vitro and in vivo: a novel 3D model system for studies of tumour cell-bone cell interactions. *Clin Exp Metastasis* 2015;**32**:689-702.
24. Suva LJ, Washam C, Nicholas RW, Griffin RJ. Bone metastasis: mechanisms and therapeutic opportunities. *Nat Rev Endocrinol* 2011;**7**:208-18.
25. Engel LW, Young NA, Tralka TS, Lippman ME, O'Brien SJ, Joyce MJ. Establishment and characterization of three new continuous cell lines derived from human breast carcinomas. *Cancer Res* 1978;**38**:3352-64.
26. Engel LW, Young NA. Human breast carcinoma cells in continuous culture: a review. *Cancer Res* 1978;**38**:4327-39.
27. Soule HD, Vazguez J, Long A, Albert S, Brennan M. A human cell line from a pleural effusion derived from a breast carcinoma. *J Natl Cancer Inst* 1973;**51**:1409-16.
28. Levenson AS, Jordan VC. MCF-7: the first hormone-responsive breast cancer cell line. *Cancer Res* 1997;**57**:3071-8.
29. Yi B, Williams PJ, Niewolna M, Wang Y, Yoneda T. Tumor-derived platelet-derived growth factor-BB plays a critical role in osteosclerotic bone metastasis in an animal model of human breast cancer. *Cancer Res* 2002;**62**:917-23.
30. Thomas RJ, Guise TA, Yin JJ, Elliott J, Horwood NJ, Martin TJ, et al. Breast cancer cells interact with osteoblasts to support osteoclast formation. *Endocrinology* 1999;**140**:4451-8.
31. Canon J, Bryant R, Roudier M, Branstetter DG, Dougall WC. RANKL inhibition combined with tamoxifen treatment increases anti-tumor efficacy and prevent tumor-induced bone destruction in an estrogen receptor-positive breast cancer bone metastasis model. *Breast Cancer Res Treat* 2012;**135**:771-80.
32. Fearon KC, Glass DJ, Guttridge DC. Cancer cachexia: mediators, signaling, and metabolic pathways. *Cell metabolism* 2012;**16**:153-66.
33. Waning DL, Mohammad KS, Reiken SR, Wenjun X, Anderssen DC, John S, et al. TGFβ mediates muscle weakness associated with bone metastases. *Nature Med* 2015; Oct 12. doi: 10.1038/nm.3961. [Epub ahead of print]
34. Rucci N, Capulli M, Ventura L, Angelucci A, Peruzzi B, Tillgren V, et al. Proline/arginine-rich end leucine-rich repeat protein N-terminus is a novel osteoclast antagonist that counteracts bone loss. *J Bone Miner Res* 2013;**28**:1912-24.
35. Guise TA. Molecular mechanisms of osteolytic bone metastases. *Cancer* 2000;**88**:2892-8.
36. Wright LE, Frye JB, Lukefahr AL, Timmermann BN, Mohammad KS, Guise TA, et al. Curcuminoids block TGF-β signaling in human breast cancer cells and limit osteolysis in a murine model of breast cancer bone metastasis. *J Nat Prod* 2013;**76**:316-21.
37. Arguello F, Baggs RB, Frantz CN. A murine model of experimental metastasis to bone and bone marrow. *Cancer Res* 1988;**48**:6876-81.
38. Guise TA, Yin JJ, Taylor SD, Kumagai Y, Dallas M, Boyce BF, et al. Evidence for a causal role of parathyroid hormone-related protein in the pathogenesis of human breast cancer-mediated osteolysis. *J Clin Invest* 1996;**98**:1544-9.
39. Yoneda T, Sasaki A, Dunstan C, Williams PJ, Bauss F, De Clerck YA, et al. Inhibition of osteolytic bone metastasis of breast cancer by combined treatment with the bisphosphonate ibandronate and tissue inhibitor of the matrix metalloproteinase-2. *J Clin Invest* 1997;**99**:2509-17.

40. Johnson LC, Johnson RW, Munoz SA, Mundy GR, Peterson TE, Sterling JA. Longitudinal live animal micro-CT allows for quantitative analysis of tumor-induced bone destruction. *Bone* 2011;**48**:141-51.
41. Rosol TJ, Tannehill-Gregg SH, Corn S, Schneider A, McCauley LK. Animal models of bone metastasis. *Cancer Treat Res* 2004;**118**:47-81.
42. Coleman RE, Rubens RD. The clinical course of bone metastases from breast cancer. *Br J Cancer* 1987;**55**:61-66.
43. Rucci N, Ricevuto E, Ficorella C, Longo M, Perez M, Di Giacinto C, et al. In vivo bone metastases, osteoclastogenic ability, and phenotypic characterization of human breast cancer cells. *Bone* 2004;**34**:697-709.
44. Lu X, Wang Q, Hu G, Van Poznak C, Fleisher M, Reiss M, et al. ADAMTS1 and MMP1 proteolytically engage EGF-like ligands in an osteolytic signaling cascade for bone metastasis. *Genes Dev* 2009;**23**:1882-94.
45. Dallas SL, Garrett IR, Oyajobi BO, Dallas MR, Boyce BF, Bauss F, et al. Ibandronate reduces osteolytic lesions but not tumor burden in a murine model of myeloma bone disease. *Blood* 1999;**93**:1697-706.
46. Mitsiades CS, Mitsiades NS, Bronson RT, Chauhan D, Munshi N, Treon SP, et al. Fluorescence imaging of multiple myeloma cells in a clinically relevant SCID/NOD in vivo model: biologic and clinical implications. *Cancer Res* 2003;**63**:6689-96.
47. Yang S, Zhang JJ, Huang XY. Mouse models for tumor metastasis. *Methods Mol Biol* 2012;**928**:221-8.
48. Kuperwasser C, Dessain S, Bierbaum BE, Garnet D, Sperandio K, Gauvin GP, et al. A mouse model of human breast cancer metastasis to human bone. *Cancer Res* 2005;**65**:6130-8.
49. van der Horst G, van der Pluijm G. Preclinical models that illuminate the bone metastasis cascade. In: Joerger M, Gnant M (Eds.) Prevention of Bone Metastases. Springer-Verlag Berlin Heidelberg, 2012: 1-24.
50. Buijs JT, Henriquez NV, van Overveld PG, van der Horst G, Que I, Schwaninger R, et al. Bone morphogenetic protein 7 in the development and treatment of bone metastases from breast cancer. *Cancer Res* 2007;**67**:8742-51.
51. Bachelier R, Confavreux CB, Peyruchaud O, Croset M, Goehrig D, van der Pluijm G, et al. Combination of anti-angiogenic therapies reduces osteolysis and tumor burden in experimental breast cancer bone metastasis. *Int J Cancer* 2014;**135**:1319-29.
52. Croset M, Goehrig D, Frackowiak A, Bonnelye E, Ansieau S, Puisieux A, et al. TWIST1 expression in breast cancer cells facilitates bone metastasis formation. *J Bone Miner Res* 2014;**29**:1886-99.
53. Peyruchaud O, Winding B, Pécheur I, Serre CM, Delmas P, Clézardin P. Early detection of bone metastases in a murine model using fluorescent human breast cancer cells: application to the use of the bisphosphonate zoledronic acid in the treatment of osteolytic lesions. *J Bone Miner Res* 2001;**16**:2027-34.
54. Bouxsein ML, Boyd SK, Christiansen BA, Guldberg RE, Jepsen KJ, Müller R. Guidelines for assessment of bone microstructure in rodents using micro-computed tomography. *J Bone Miner Res* 2010;**25**:1468-86.
55. Lim E, Modi K, Christensen A, Meganck J, Oldfield S, Zhang N. Monitoring tumor metastases and osteolytic lesions with bioluminescence and micro CT imaging. J Vis Exp 2011;Apr14:pii2775.
56. Cowey S, Szafran A., Kappes J, Zinn KR, Siegal GP, Desmond RA, et al. Breast cancer metastasis to bone: evaluation of bioluminescent imaging and microSPECT/CT for detecting bone metastasis in immunodeficient mice. *Clin Exp Metastasis* 2007;**24**:389-401.

Figure Legends

Figure 1. Radiographs of the distal femur and proximal tibia of mice with breast cancer bone metastases. Representative images are presented of **A**. MDA-MB-231 breast cancer bone metastases four weeks post-inoculation of 100,000 cells via intra-cardiac route, **B**. ZR-75-1 breast cancer bone metastases 25 weeks post-inoculation of 100,000 cells via intra-cardiac route, **C**. 4T1 breast cancer bone metastases four weeks post-inoculation of 10,000 cells via intra-tibial route, and **D**. MCF-7 breast cancer bone metastases 20 weeks post-inoculation of 100,000 cells via intra-tibial route.

Figure 2. Inoculation of breast cancer cells in the left cardiac ventricle of a mouse.

Figure 3. Schematic representation of the tail vasculature of a mouse.

Figure 4. Inoculation of breast cancer cells in the 4^{th} mammary fat pad of a mouse.

Figure 5. Inoculation of breast cancer cells in the proximal tibia of a mouse.

Figure 6. The assessment of tumor progression in bone can be done by **A**. quantitation of osteolytic lesion area by X-Ray, **B**. measurement of bone volume fraction (BV/TV) by bone high resolution microcomputed tomography (μCT), **C**. histological assessment of tumor area using hematoxylin/eosin (H&E) staining of long bones and vertebrae, and **D.** quantitation of tartrate resistant acid phosphatase (TRAcP)+ osteoclasts.

Appendices

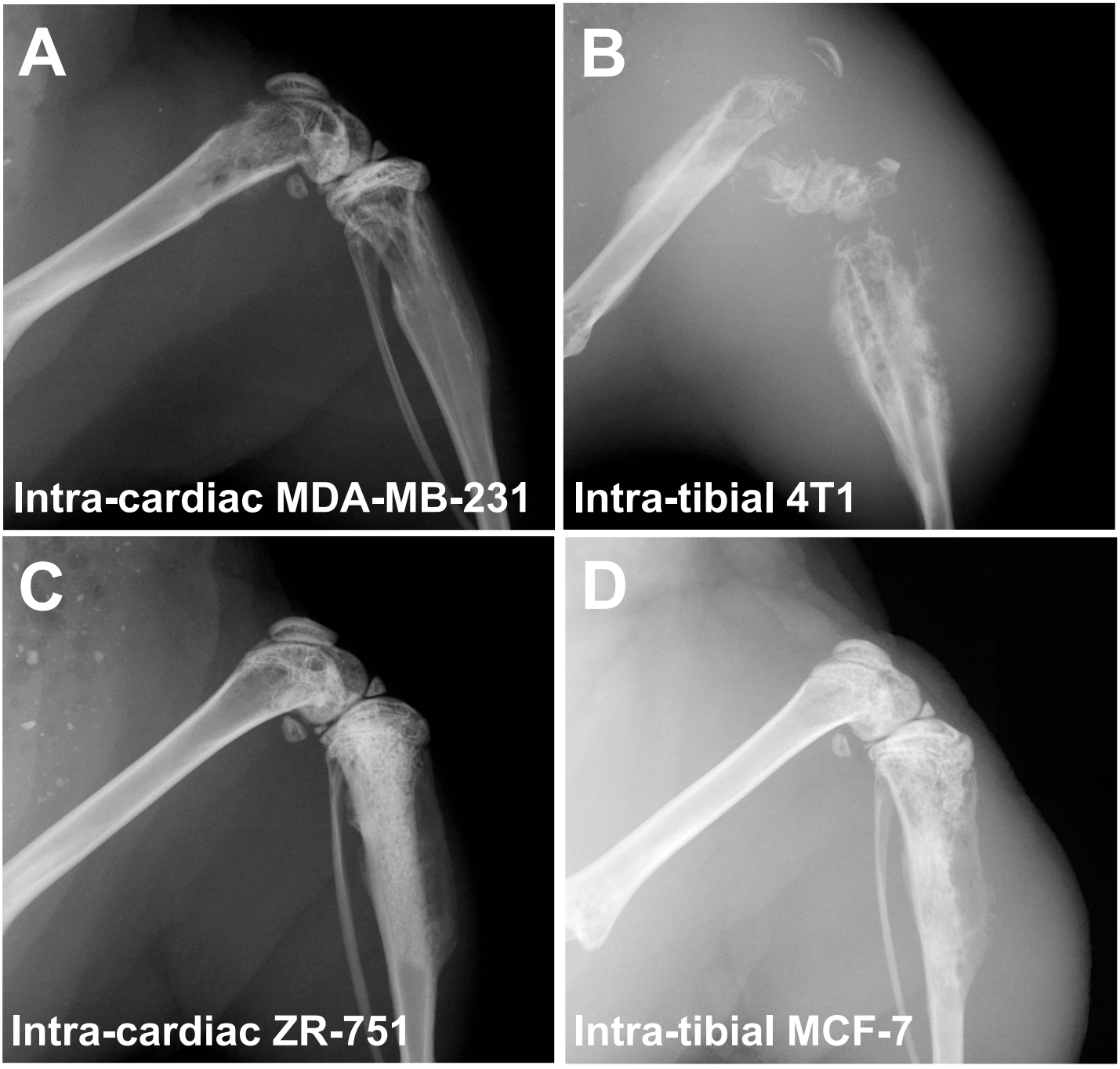
A
Intra-cardiac MDA-MB-231
B
Intra-tibial 4T1
C
Intra-cardiac ZR-751
D
Intra-tibial MCF-7

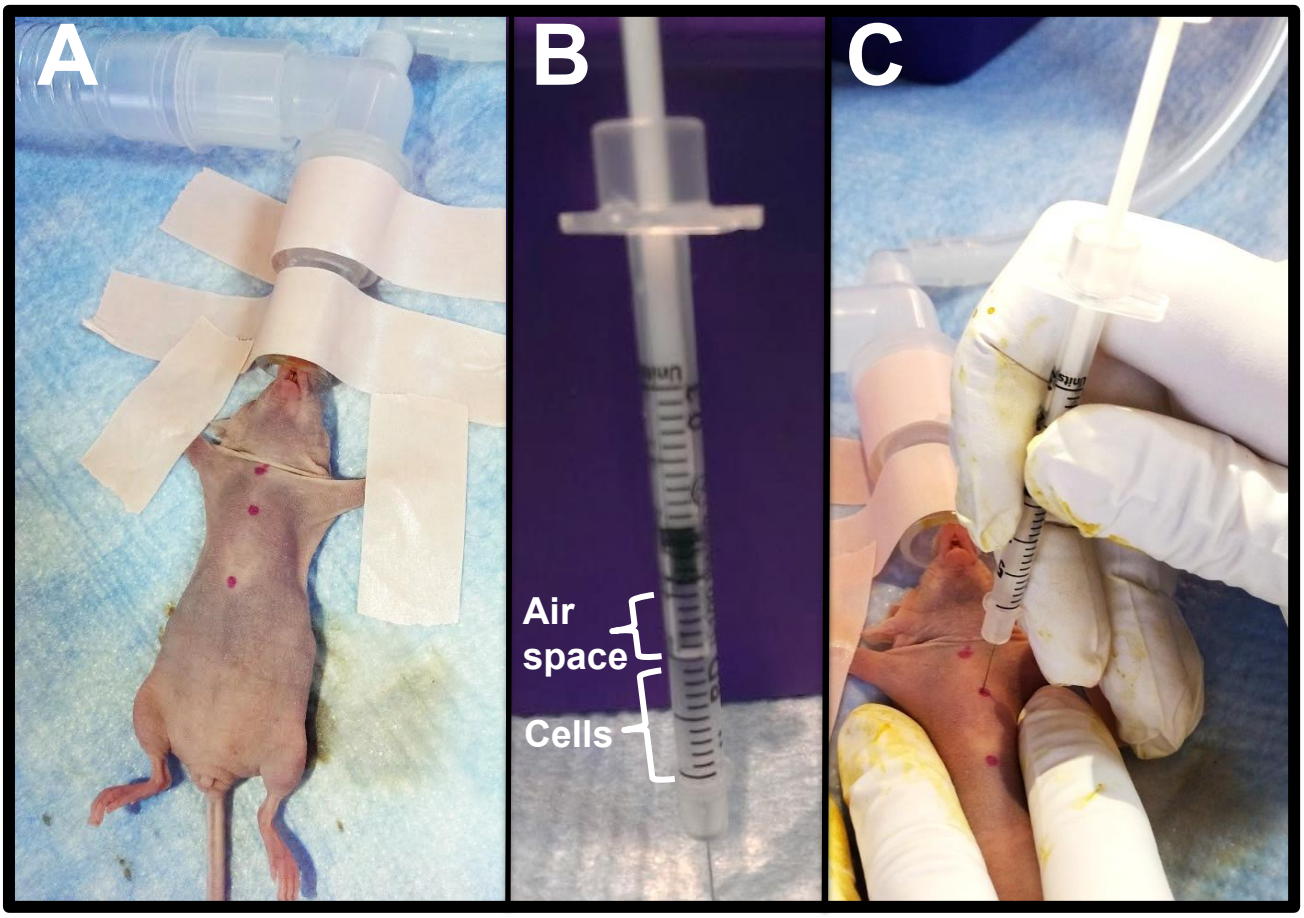
A
B
C
Air space
Cells

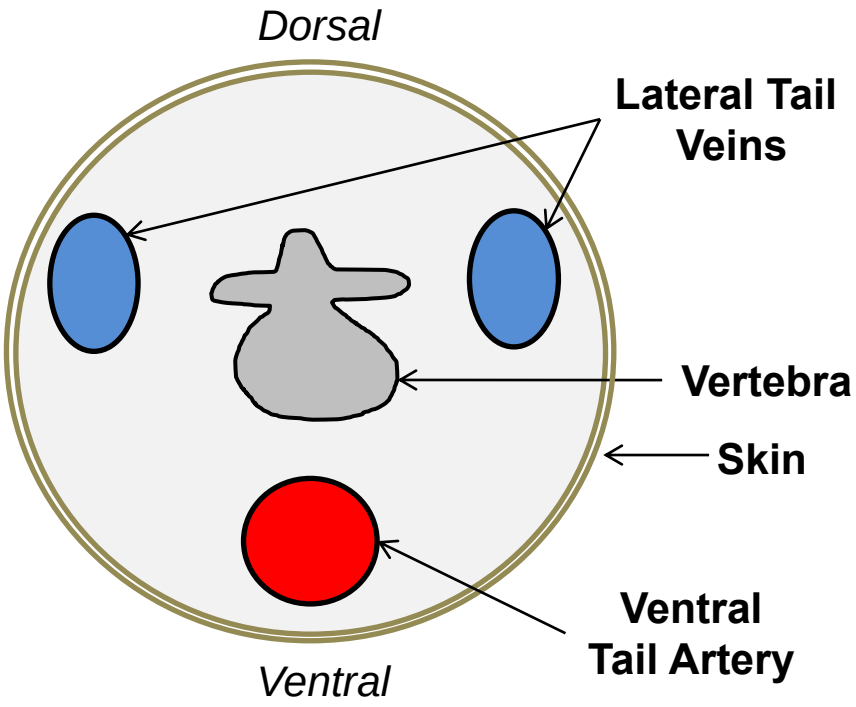
Dorsal
Lateral Tail Veins
Vertebra
Skin
Ventral Tail Artery
Ventral

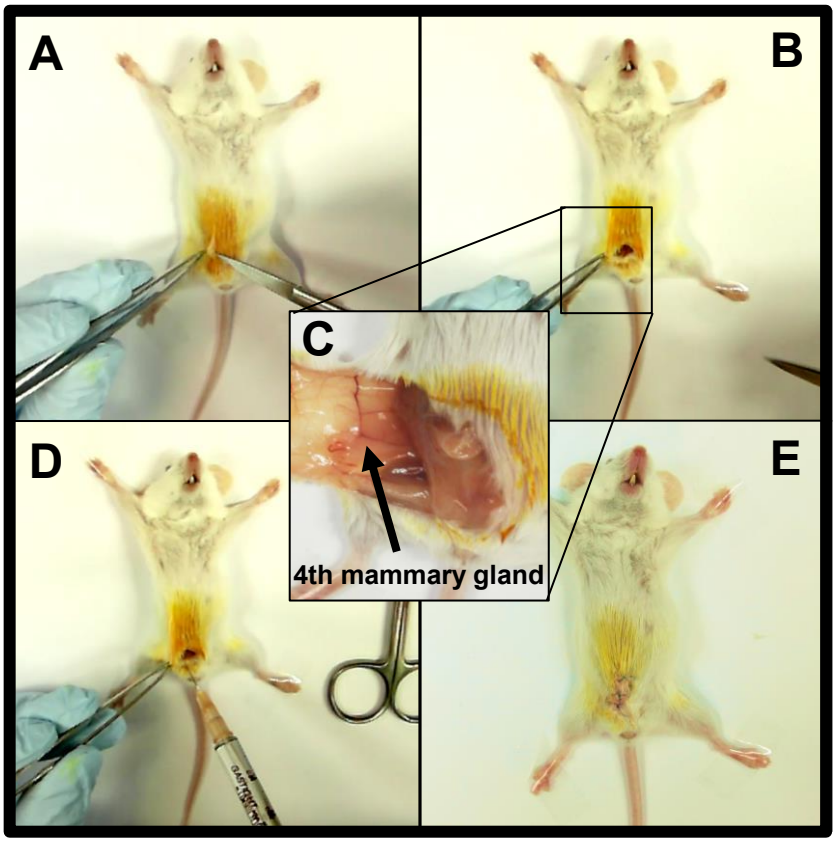
A
B
C
4th mammary gland
D
E

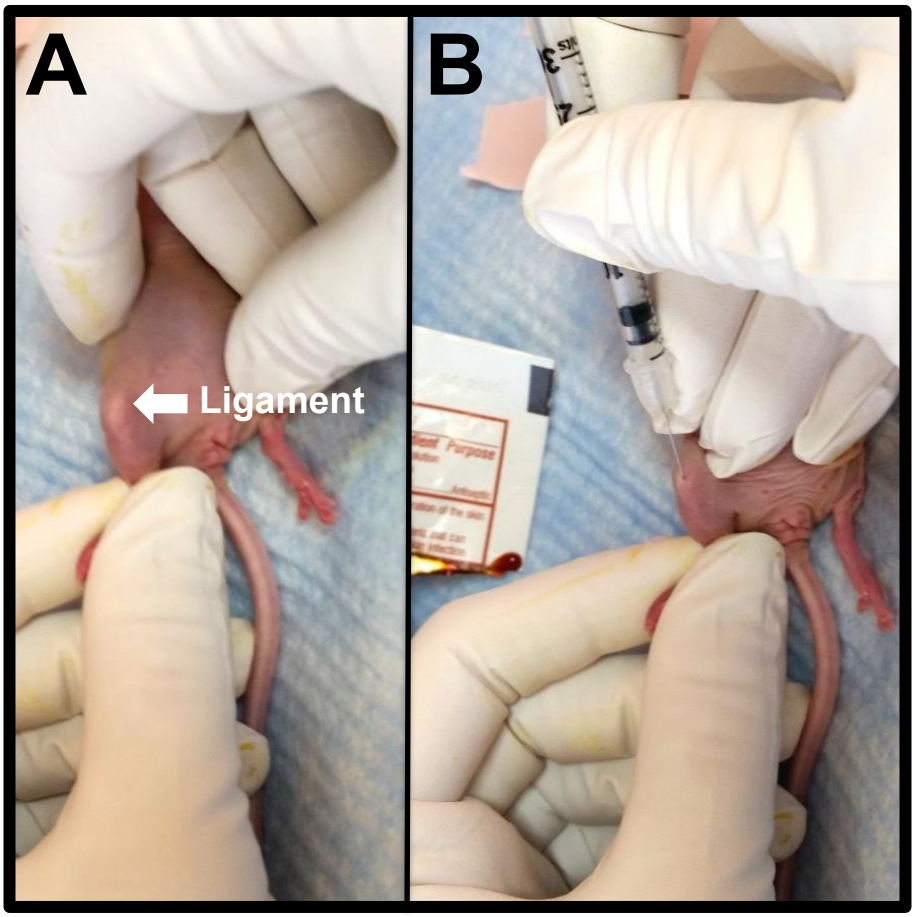
A
Ligament
B

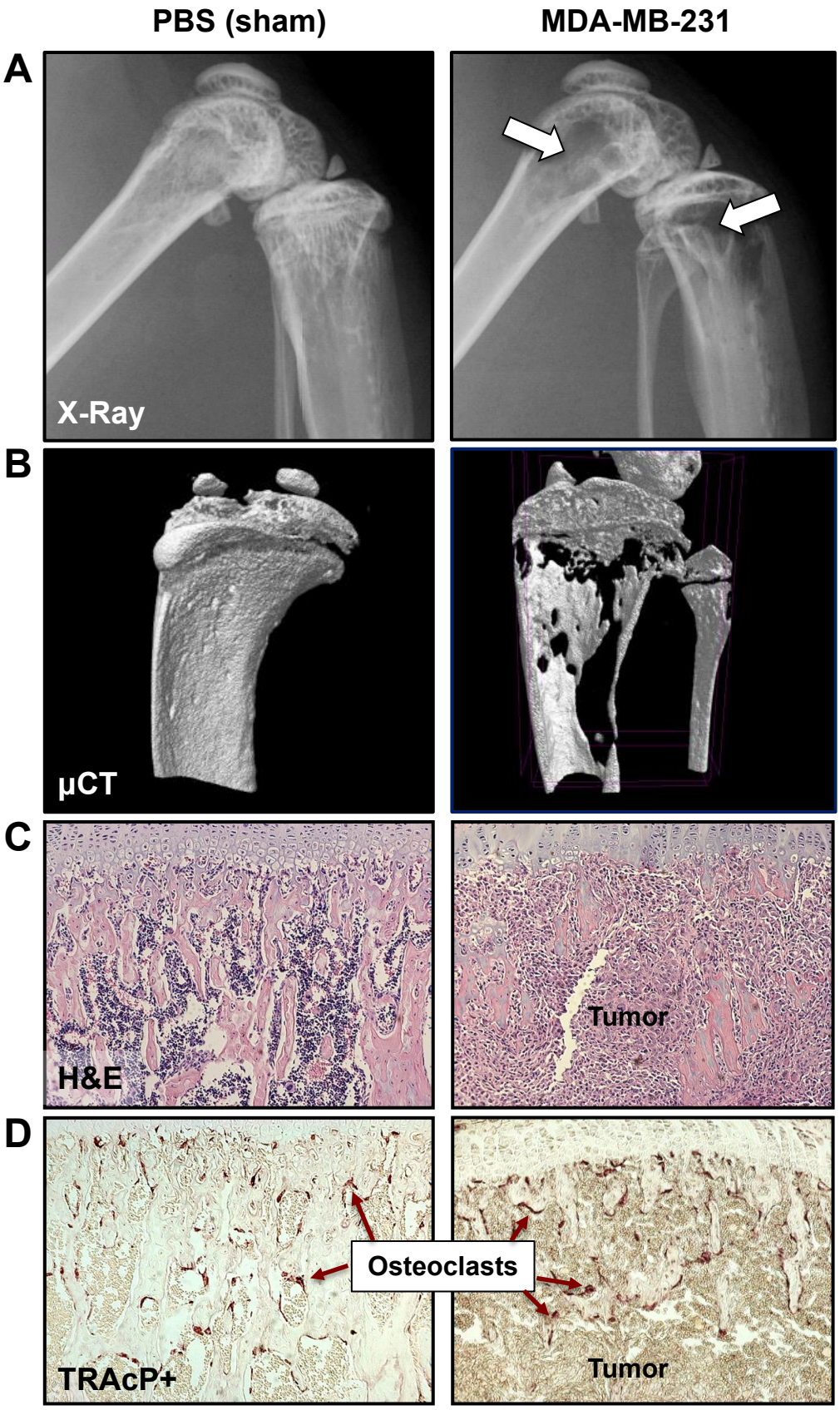
PBS (sham)
MDA-MB-231
A
X-Ray
B
µCT
C
H&E
Tumor
D
TRAcP+
Osteoclasts
Tumor

Table 1 Human and mouse mammary cancer cell lines that form osteolytic bone lesions following inoculation into mice

Cell line	Species	Origin	Subline	Mouse strain	Inoculation route	Metastatic site(s)	Time to lesion formation
MDA-MB-231	Human	Human mammary adenocarcinoma isolated from a pleural effusion from a 51 year old Caucasian female	Parental	BALB/c nude MF1 nude NOD/SCID	Intra-cardiac	Mouse long bones, spine and jaw	2-3 weeks
					Intra-tibial	Mouse tibiae	1-3 weeks
				NSG	Orthotopic	Mouse bones	7 weeks
			MDA-MB-231-BO2	BALB/c nude	Intra-cardiac	Mouse long bones, spine and jaw	2-3 weeks
					Intra-tibial	Mouse tibiae	1-3 weeks
					Intra-arterial	Mouse long bones	2-3 weeks
			MDA-MB-231-IV	BALB/c nude	Intra-cardiac	Mouse long bones, spine and jaw	2-3 weeks
					Intra-tibial	Mouse tibiae	1-3 weeks
					Intra-arterial	Mouse long bones	2-3 weeks
					Intra-venous	Mouse long bones	2-3 weeks
					Orthotopic	Human bone X-plants	10-14 weeks
MDA-MB-436	Human	Human mammary adenocarcinoma isolated from a pleural effusion from a 43 year old Caucasian female	Parental	MF1 nude BALB/c nude NOD/SCID	Intra-osseous	Mouse tibiae	2-3 weeks
SUM1315	Human	Isolated from a metastatic nodule of a Caucasian female	Parental	NOD/SCID	Intra-tibial	Mouse tibiae	3-4 weeks
					Orthotopic	Human bone X-	8-12

		patient with ductal carcinoma				plants	weeks
4T1	Mouse	Isolated from a stage 1V mammary tumor from a female BALB/c cfC3H mouse	Parental	BALB/c cfC3H	Intra-cardiac Intra-tibial Orthotopic	Mouse long bones, spine, jaw and lungs Mouse tibiae Mouse long bones, jaw and lungs	2-3 weeks 1-3 weeks 3-6 weeks
			4T1-2	BALB/c cfC3H	Intra-cardiac Intra-tibial Orthotopic	Mouse long bones, spine, jaw and lungs Mouse tibiae Mouse long bones, jaw and lungs	2-3 weeks 1-3 weeks 3-4 weeks
PyMT MMTV	Mouse	Isolated from mammary tumour induced by MMTV viral oncogene in FVB/N female mouse	Parental	FVB/N	Intra-cardiac Intra-tibial	Mouse long bones, spine, jaw and lungs Mouse tibiae	2-3 weeks 1-2 weeks
KEP	Mouse	Mouse invasive lobular carcinoma derived from a Keratin14-driven E-cadherin/p53 (KEP) knock out primary mammary carcinoma	KEP/Luc KEP/Luc	$RAG^{-/-}$; $IL2R\gamma c^{-/-}$ BALB/c BALB/c nude	Orthotopic Intra-cardiac Orthotopic Intra-tibial	Spine Mouse long bones and spine Mouse long bones and spine Mouse tibiae	3-5 weeks 2-4 weeks 6-9 weeks 2-4 weeks

Table 2 Human mammary cancer cell lines that form osteoblastic bone lesions following inoculation into mice

Cell line	Species	Origin	Subline	Mouse strain	Inoculation route	Metastatic site(s)	Time to lesion formation
MCF-7	Human	Human mammary adenocarcinoma isolated from a pleural effusion in a 69 year old Caucasian female	Parental	BALB/c nude	Intra-cardiac Intra-tibial	Mouse long bones Mouse tibiae	20-25 weeks 1-3 weeks
			MCF-7/Neu	BALB/c nude	Intra-cardiac Intra-tibial	Mouse long bones Mouse tibiae	10-12 weeks 1-3 weeks
ZR-75-1	Human	Human ductal carcinoma derived from a malignant ascetic effusion in a 63 year old Caucasian female	Parental	BALB/c nude	Intra-cardiac	Mouse long bones and spine	12-25 weeks

Table 3 Preparation of breast cancer tumor cells for inoculation in mice

Inoculation route	Cell number	Volume (PBS)	Syringe / needle
Intra-cardiac	100,000	100µL	0.5 - 1cc insulin / 27-29G, 0.5 inch
Intra-arterial (tail)	100,000	100µL	0.5 - 1cc insulin / 27-29G, 0.5 inch
Orthotopic	100,000 – 500,000	10 – 20µL	0.1cc Hamilton / 25-27G, 0.5 inch
Intra-tibial	10,000 – 250,000	10 – 20µL	0.1cc Hamilton / 25-27G, 0.5 inch

Table 4 Principal endpoints used to characterize the development of bone metastases in mice

***In vivo* analyses**	
Type	**Frequency**
Activity levels and hind limb mobility	Daily
Respiratory distress	Daily
Symptoms of cachexia	Daily
X-Ray analysis of osteolytic lesions	Weekly or bi-monthly
Bioluminescence imaging (BLI; if applicable)	Weekly or bi-monthly
***Post mortem* analyses**	
Type	**Endpoint**
Gross dissection	Inspection for visceral metastases in lung, liver, adrenals, and brain tissue
Bone microcomputed tomography (μCT)	Trabecular bone volume/total volume (BV/TV) of the proximal tibia, distal femur, and lumbar vertebrae
Histomorphometric analysis of bone	TRAcP staining of bone - Osteoclast number/bone surface (OcN/BS) - Osteoclast surface/bone surface (OcS/BS) - Osteoclast number at the bone-tumor interface Hematoxylin/eosin (H&E) staining of bone for BV/TV and osteoblast number/bone surface (ObN/BS)
Tumor characterization	H&E staining of forelimbs, hind limbs, and spine for total tumor area in bone Immunohistochemical staining for proteins of interest (e.g., cytokeratin, phospho-smads) H&E staining of visceral organs for quantitation of soft tissue metastases
Serum factors	Biomarkers, if applicable (e.g., bone turnover markers, hormones, inflammatory factors, growth factors, tumor-derived factors)

nature medicine

Excess TGF-β mediates muscle weakness associated with bone metastases in mice

David L Waning[1,9], Khalid S Mohammad[1,9], Steven Reiken[2], Wenjun Xie[2], Daniel C Andersson[2,8], Sutha John[1], Antonella Chiechi[1], Laura E Wright[1], Alisa Umanskaya[2], Maria Niewolna[1], Trupti Trivedi[1], Sahba Charkhzarrin[1], Pooja Khatiwada[1], Anetta Wronska[2], Ashley Haynes[2], Maria Serena Benassi[3], Frank A Witzmann[4], Gehua Zhen[5], Xiao Wang[5], Xu Cao[5], G David Roodman[6,7], Andrew R Marks[2] & Theresa A Guise[1]

Cancer-associated muscle weakness is a poorly understood phenomenon, and there is no effective treatment. Here we find that seven different mouse models of human osteolytic bone metastases—representing breast, lung and prostate cancers, as well as multiple myeloma—exhibited impaired muscle function, implicating a role for the tumor-bone microenvironment in cancer-associated muscle weakness. We found that transforming growth factor (TGF)-β, released from the bone surface as a result of metastasis-induced bone destruction, upregulated NADPH oxidase 4 (Nox4), resulting in elevated oxidization of skeletal muscle proteins, including the ryanodine receptor and calcium (Ca^{2+}) release channel (RyR1). The oxidized RyR1 channels leaked Ca^{2+}, resulting in lower intracellular signaling, which is required for proper muscle contraction. We found that inhibiting RyR1 leakage, TGF-β signaling, TGF-β release from bone or Nox4 activity improved muscle function in mice with MDA-MB-231 bone metastases. Humans with breast- or lung cancer–associated bone metastases also had oxidized skeletal muscle RyR1 that is not seen in normal muscle. Similarly, skeletal muscle weakness, increased Nox4 binding to RyR1 and oxidation of RyR1 were present in a mouse model of Camurati-Engelmann disease, a nonmalignant metabolic bone disorder associated with increased TGF-β activity. Thus, pathological TGF-β release from bone contributes to muscle weakness by decreasing Ca^{2+}-induced muscle force production.

Skeletal muscle weakness is a debilitating consequence of advanced malignancies, which are often associated with bone metastases. Research and therapy have focused on increasing muscle mass in humans with cancer-associated skeletal muscle weakness[1], but it is unclear whether a gain of mass alone will improve muscle function[2,3]. Moreover, little is known about whether tumors and their associated metastases cause muscle dysfunction resulting in weakness, or whether cancer-associated weakness is due solely to loss of muscle mass. Therefore, using mouse models of human cancers with bone metastases, we investigated whether there is a cause of muscle weakness that is independent of muscle mass loss.

Individuals with advanced cancer (including those of the breast, prostate and lung), often have bone metastases and muscle weakness. In the tumor-bone microenvironment, cancer cells (including those in individuals with multiple myeloma) secrete factors that stimulate osteoclastic bone resorption, resulting in skeletal complications of bone pain, fractures, hypercalcemia, nerve compression syndromes and muscle weakness[4]. Osteoclastic bone resorption releases growth factors stored in the bone matrix, principally TGF-β, that further promote cancer cell invasion, growth and osteolytic factor production to fuel a feed-forward cycle that induces more bone destruction and tumor growth[4–7]. Bone resorption and formation is dynamically coupled by TGF-β (ref. 8), and pathologically increased TGF-β release from bone, due to tumor-induced osteolysis, could be contributing to muscle weakness. Here we found that mouse models of human breast, lung and prostate cancers, as well as a mouse model of multiple myeloma, in which all mice develop osteolytic bone metastases and exhibit profound skeletal muscle weakness. We report that pathologically increased TGF-β release from bone causes muscle weakness by inducing intracellular Ca^{2+} leakage via Nox4-mediated oxidation of RyR1 on the sarcoplasmic reticulum (SR).

In normal muscle, activation of RyR1 results in the release of SR Ca^{2+} that is the required signal to trigger skeletal muscle contraction[9]. Pathological oxidation of RyR1 results in leaky channels that contribute to muscle weakness[10]. Here we show that targeting intracellular Ca^{2+} leakage, bone resorption, TGF-β activity and Nox4 activity can all prevent muscle weakness in mice with breast cancer–derived bone metastases. Furthermore, increased Nox4 binding to RyR1, oxidation of RyR1 and muscle weakness were observed in a mouse model of

[1]Department of Medicine, Indiana University School of Medicine, Indianapolis, Indiana, USA. [2]Department of Physiology and Cellular Biophysics, Helen and Clyde Wu Center for Molecular Cardiology, College of Physicians and Surgeons, Columbia University, New York, New York, USA. [3]Laboratory of Experimental Oncology, Instituto Ortopedico Rizzoli, Bologna, Italy. [4]Department of Cellular and Integrative Physiology, Indiana University School of Medicine, Indianapolis, Indiana, USA. [5]Department of Orthopedic Surgery, Johns Hopkins University School of Medicine, Baltimore, Maryland, USA. [6]Department of Medicine, Division of Hematology and Oncology, Indiana University School of Medicine, Indianapolis, Indiana, USA. [7]Richard L. Roudebush Virginia Medical Center, Indianapolis, Indiana, USA. [8]Present addresses: Department of Medicine, Cardiology Unit, Karolinska Institute, Stockholm, Sweden, and Department of Physiology and Pharmacology, Karolinska Institute, Stockholm, Sweden (D.C.A.). [9]These authors contributed equally to this work. Correspondence should be addressed to T.A.G. (tguise@iu.edu).

Received 3 April; accepted 2 September; published online 12 October 2015; doi:10.1038/nm.3961

Camurati-Engelmann disease (CED), a nonmalignant metabolic bone disorder associated with increased TGF-β activity and bone destruction.

These findings raise the possibility that increased bone destruction and associated elevations in TGF-β activity can induce skeletal muscle weakness by the oxidation of RyR1 and the resultant Ca^{2+} leakage. Thus, targeting any portion of this pathway might help to ameliorate muscle weakness in cancer patients with bone metastases.

RESULTS

Weakness and RyR1 oxidation in mice with bone metastases

To explore the basis for cancer-associated muscle weakness, we used a mouse model of human breast cancer (MDA-MB-231) that causes osteolytic bone metastases and muscle weakness (**Supplementary Fig. 1a**)[11]. We inoculated 5-week-old female nude mice with 100,000 MDA-MB-231 human breast cancer cells via the left cardiac ventricle and found that these mice had bone metastases, lower skeletal muscle mass and reduced body weight, fat and lean content (**Supplementary Fig. 1b**) 4 weeks post-tumor inoculation as compared to tumor-free (non-tumor) control mice (**Supplementary Fig. 1c**,**d**). As compared to the non-tumor control mice, the tumor-bearing mice developed muscle weakness (reduction in forelimb grip strength) (**Fig. 1a**), and the extensor digitorum longus (EDL) muscle showed lower *ex vivo* muscle-specific force (which represents the muscle force corrected for changes in muscle size) (**Fig. 1b**). Peak tetanic Ca^{2+} determines muscle force, and we found that this was also lower in the MDA-MB-231–inoculated mice than in the non–tumor-bearing control mice (**Fig. 1c**) Thus, in addition to loss of muscle mass, mice with breast cancer bone metastases had loss of muscle function.

Advanced breast cancer is characterized by increased oxidative stress[12]. We used an unbiased mass spectrometry–based screen to assess post-translational modifications of proteins in whole skeletal muscle lysates from mice with bone metastases as compared to those from non–tumor-bearing controls (**Supplementary Tables 1** and **2**). Measurement of the total carbonyl concentration in skeletal muscle lysates also showed that skeletal muscle from mice and humans with tumors metastatic to bone exhibited higher skeletal muscle protein oxidation as compared to muscle from mice and humans without bone metastases (**Supplementary Table 3**). We found that proteins involved in muscle contraction were among the skeletal muscle proteins that were nitrosylated or oxidized in mice with bone metastases (**Supplementary Tables 1** and **2**). These included sarcomeric proteins (such as tropomyosin and myosin) and the RyR1 Ca^{2+} release channel, which was identified as being both nitrosylated and oxidized (**Supplementary Tables 1** and **2**). Because tetanic Ca^{2+} was lower in mice with MDA-MB-231 bone metastases than in non-tumor control mice, we focused on RyR1, as this channel is the source of Ca^{2+} release from the SR in skeletal muscle. Oxidation of RyR1 channels in skeletal muscle results in a pathological SR Ca^{2+} leak that is associated with muscle weakness[10,13]. Indeed, skeletal muscle RyR1 channels from mice with bone metastases were oxidized, nitrosylated and depleted of the stabilizing subunit calstabin1 (also known as FKBP12) as compared to that from non-tumor control mice (the biochemical signature of leaky channels) (**Fig. 1d**). These oxidation-induced changes in RyR1 were progressive over 4 weeks after tumor inoculation during the development of bone metastases (**Supplementary Fig. 1e**) and were associated with lower muscle-specific force in mice with breast cancer bone metastases than in non-tumor control mice (**Supplementary Fig. 1f**). Mice with MDA-MB-231 breast cancer bone metastases had large osteolytic lesions, as determined by analysis of X-ray images, and the degree of muscle weakness correlated with the amount of bone destruction 4 weeks after tumor inoculation (**Supplementary Fig. 1g**,**h**). To determine whether the RyR1 modifications observed in the mouse models were relevant to human cancer, we examined skeletal muscle RyR1 from humans with breast cancer–associated bone metastases or lung cancer–associated bone metastases and compared them to those from humans who did not have cancer and found the same post-translational modifications (oxidation and nitrosylation of RyR1 and lower calstabin1 binding) as we observed in the mouse models, which we hereafter refer to as the biochemical signature of leaky RyR1 channels (**Fig. 1e**,**f**).

Muscle weakness associated with bone metastases

Because muscle weakness strongly correlated with bone destruction (**Supplementary Fig. 1h**), we investigated whether the tumor-bone microenvironment plays a role in cancer-associated muscle weakness. We inoculated 1×10^6 MDA-MB-231 cells (tenfold more cells than were used in the bone metastasis model) into the mammary fat pad (inoculation into which causes primary breast cancer only[14] and no bone metastases) and found that, in contrast to mice with bone metastases, mice with primary MDA-MB-231 mammary tumors (mean tumor mass 400 ± 91 mg) had normal muscle function (**Fig. 1g**), muscle mass, body weight and body composition (**Supplementary Fig. 1i**,**j**). Notably, these mice did not exhibit the biochemical signature of leaky RyR1 channels, in contrast to mice with bone metastases (**Fig. 1h**). These data suggest that the tumor-bone microenvironment has a critical role in the development of cancer-associated muscle weakness.

Here we examined mice with bone metastases resulting from seven different forms of human cancers, including MDA-MB-231 breast cancer, MCF-7 breast cancer, ZR75-1 breast cancer, A549 lung cancer, RWGT2 lung cancer[15], PC-3 prostate cancer and JJN-3 multiple myeloma, and we compared the results obtained from each group of mice with those from non-tumor control mice. We sought to determine whether muscle weakness and oxidative modifications of RyR1 are common features of diverse malignancies that are associated with bone destruction (osteolysis). These cancer models have bone metastases that are associated with components of ostelolysis (except for ZR75-1, which is osteoblastic). Similarly to mice with MDA-MB-231 breast cancer bone metastases, mice with osteolytic or mixed osteolytic and osteoblastic bone metastases (i.e., with components of both bone destruction and bone formation) also had lower EDL *ex vivo* muscle-specific force than did non-tumor control mice.

Mice with A549 human lung cancer bone metastases had osteolytic bone destruction, reduced forelimb grip strength and lower *ex vivo* muscle-specific force generation of the EDL than in non-tumor control mice (**Supplementary Fig. 2a**). Similarly to mice with MDA-MB-231 breast cancer bone metastases, we observed that A549 inoculation resulted in mice with lower muscle weights (EDL, tibialis anterior, soleus and gastrocnemius) and reduced body weight owing to loss of both lean and fat mass as compared to non-tumor control mice (**Supplementary Fig. 2b**). Skeletal muscle RyR1 channels from mice with A549 lung cancer bone metastases also exhibited the biochemical signature of leaky channels[10,13], as observed with skeletal muscle RyR1 from MDA-MB-231 mice (**Supplementary Fig. 2c**). RWGT2 human lung cancer bone metastases[15] caused mixed osteolytic and osteoblastic lesions in bone, and these mice had lower EDL *ex vivo* muscle-specific force but without reduced forelimb grip strength as compared to non-tumor control mice (**Supplementary Fig. 2d**). RWGT2 did not lower skeletal muscle weight (with the exception of the soleus), reduce whole body weight, alter body composition or lower

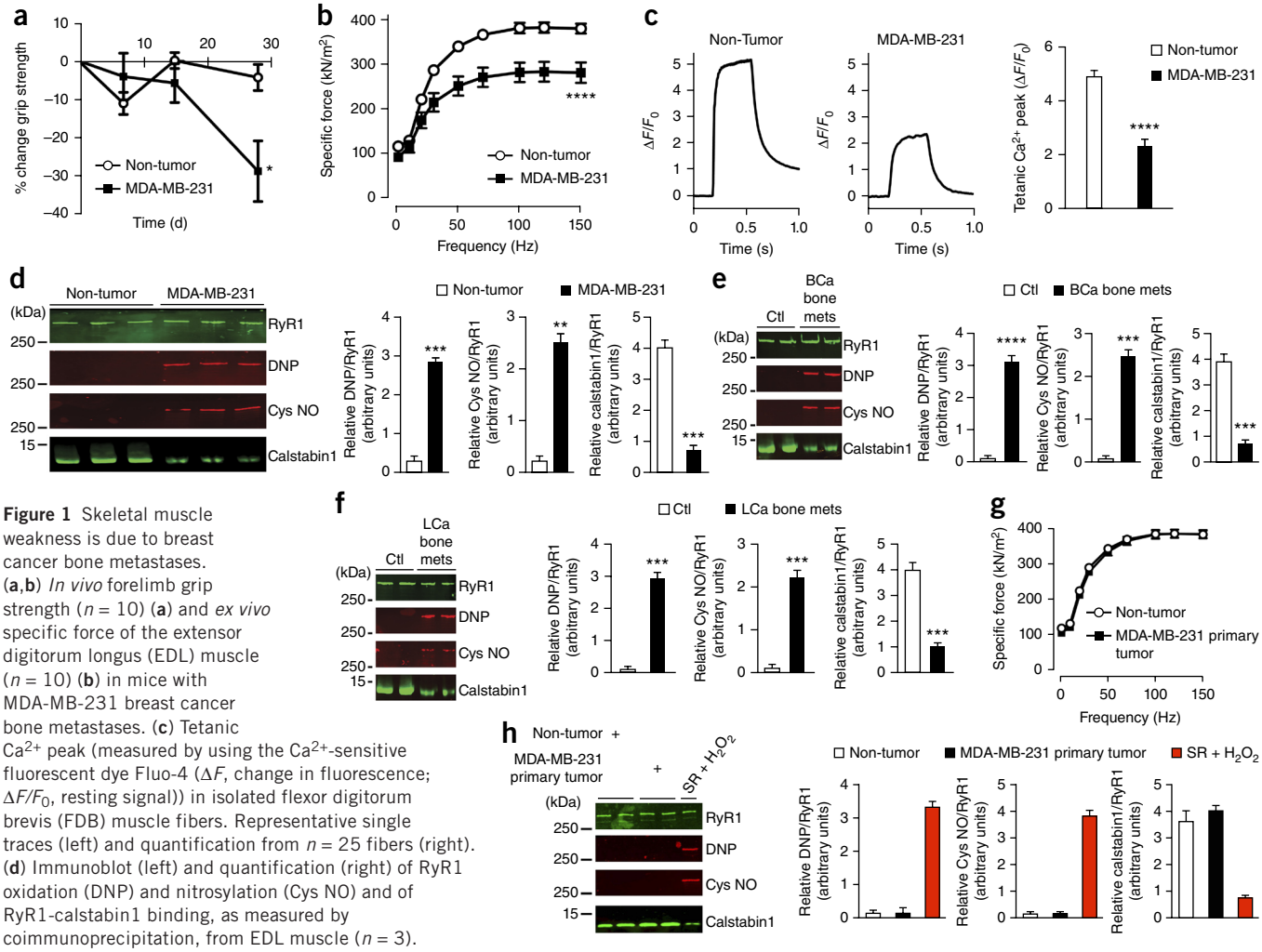

Figure 1 Skeletal muscle weakness is due to breast cancer bone metastases. (**a**,**b**) *In vivo* forelimb grip strength ($n = 10$) (**a**) and *ex vivo* specific force of the extensor digitorum longus (EDL) muscle ($n = 10$) (**b**) in mice with MDA-MB-231 breast cancer bone metastases. (**c**) Tetanic Ca^{2+} peak (measured by using the Ca^{2+}-sensitive fluorescent dye Fluo-4 (ΔF, change in fluorescence; $\Delta F/F_0$, resting signal)) in isolated flexor digitorum brevis (FDB) muscle fibers. Representative single traces (left) and quantification from $n = 25$ fibers (right). (**d**) Immunoblot (left) and quantification (right) of RyR1 oxidation (DNP) and nitrosylation (Cys NO) and of RyR1-calstabin1 binding, as measured by coimmunoprecipitation, from EDL muscle ($n = 3$). (**e**,**f**) Immunoblot (left) and quantification (right) of RyR1 oxidation and nitrosylation and of RyR1-calstabin1 binding in muscle samples from humans with breast cancer bone metastases (BCa bone mets) (**e**) or lung cancer bone metastases (LCa bone mets) (**f**) and their respective controls (Ctl); $n = 4$ per group. (**g**) *Ex vivo* EDL specific force in mice with primary MDA-MB-231 breast cancer as compared to that in non-tumor control mice ($n = 9$). (**h**) Immunoblot (left) and quantification (right) of RyR1 oxidation and nitrosylation and of RyR1-calstabin1 binding in mice with primary breast cancer ($n = 4$ per group). SR + H_2O_2, sarcoplasmic reticulum preparations treated with hydrogen peroxide. Data are mean ± s.e.m. Statistical analysis in **a**,**b**,**g** was by two-way analysis of variance (ANOVA) and in **c**–**f** was by Student's *t*-test. $^*P < 0.05$, $^{**}P < 0.01$, $^{***}P < 0.001$, $^{****}P < 0.0001$.

mid-calf cross-sectional area as compared to that observed in non-tumor control mice (**Supplementary Fig. 2e**); however, these mice did exhibit RyR1 modifications similarly to those seen in mice with MDA-MB-231 breast cancer bone metastases (**Supplementary Fig. 2f**).

Mice with MCF-7 breast cancer–associated bone metastases, which have osteolytic and osteoblastic (mixed) components, also had lower EDL *ex vivo* muscle-specific force than non-tumor control mice (**Supplementary Fig. 2g**). As compared to non-tumor control animals, mice with MCF-7–associated bone metastases did not have lower muscle weight but did lose total body weight (**Supplementary Fig. 2h**). Skeletal muscle RyR1 channels from mice with MCF-7 breast cancer and bone metastases also exhibited the same biochemical signature of leaky channels as that observed in MDA-MB-231 tumor–bearing mice with bone metastases (**Supplementary Fig. 2i**).

PC-3 human prostate cancer tumor–bearing mice showed osteolytic metastases, reduction in forelimb grip strength and lower EDL *ex vivo* muscle-specific force in comparison with non-tumor control mice (**Supplementary Fig. 3a**). As compared to the control mice, these mice also had lower muscle weight, reduced body weight and lower fat and lean mass (**Supplementary Fig. 3b**), and they showed the biochemical signature of leaky RyR1 channels (**Supplementary Fig. 3c**).

Direct inoculation of human JJN-3 multiple myeloma cells into the tibias of mice caused bone destruction as previously described[16] but no loss of body weight. Mice with JJN-3 multiple myeloma, as compared to non-tumor control mice, had lower *ex vivo* muscle-specific force of the EDL (measured in the contralateral limb), and their RyR1 channels exhibited the biochemical signature of leaky channels (**Supplementary Fig. 3d**). JJN-3 multiple myeloma–induced bone destruction (osteolytic lesion area) correlated with decreased specific force of the EDL in the contralateral limb (without decreased muscle mass or body weight) compared to non-tumor control mice, indicating once again that local bone destruction in the tumor-bone microenvironment can cause systemic muscle weakness (**Supplementary Fig. 3e**).

In contrast to non-tumor control animals, mice injected with ZR75-1 human breast cancer cells had bone metastases with abnormal new bone formation but without bone destruction (osteoblastic), as well as lower EDL *ex vivo* muscle-specific force but not reduced forelimb

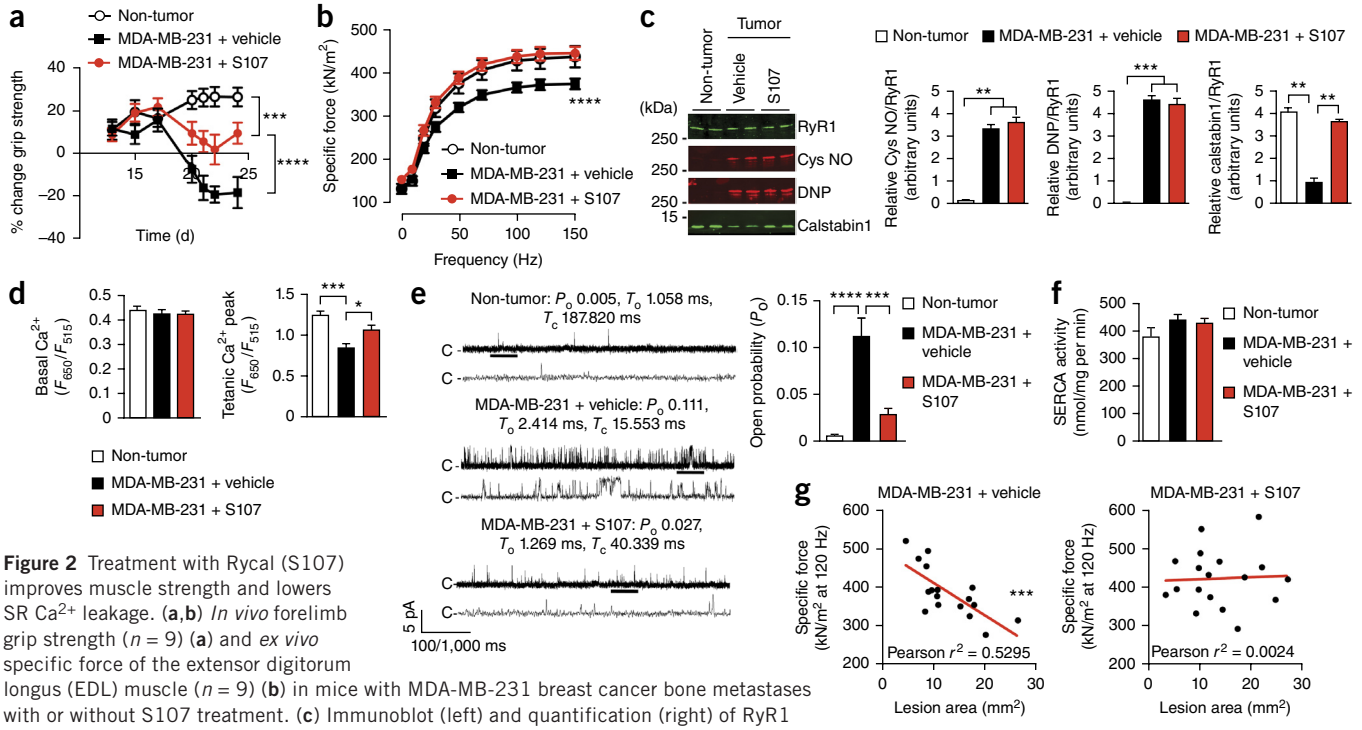

Figure 2 Treatment with Rycal (S107) improves muscle strength and lowers SR Ca^{2+} leakage. (**a**,**b**) *In vivo* forelimb grip strength ($n = 9$) (**a**) and *ex vivo* specific force of the extensor digitorum longus (EDL) muscle ($n = 9$) (**b**) in mice with MDA-MB-231 breast cancer bone metastases with or without S107 treatment. (**c**) Immunoblot (left) and quantification (right) of RyR1 oxidation (DNP) and nitrosylation (Cys NO) and of RyR1-calstabin1 binding, as measured by coimmunoprecipitation, from EDL muscle ($n = 4$). (**d**) Peak tetanic Ca^{2+} amplitude in mice with MDA-MB-231 bone metastases receiving S107 treatment (ratiometric imaging using the Ca^{2+} fluorescent dyes Fluo-4 and Fura-red to obtain an $F_{650\ nm}/F_{515\ nm}$ ratio, reflecting the absolute Ca^{2+} level) in flexor digitorum brevis (FDB) muscle fibers ($n = 36$ fibers). (**e**) RyR1 channel open probability in muscle from mice with MDA-MB-231 bone metastases receiving S107 treatment. Left, representative single-channel current traces of skeletal RyR1 channels ($n = 4$). Channel openings are shown as upward deflections. P_o, open probability; T_o, average open time; T_c, average closed time. The activity of the channel, as indicated by the thick black bar, is shown below on the expanded time scale. Right, quantification of traces from $n = 4$ channel recordings. (**f**) SERCA activity from muscle of mice with bone metastases and treated with S107 ($n = 4$). (**g**) Correlation between maximum specific force (120 Hz) and osteolytic lesion area (as measured in all limbs by X-ray imaging) in muscle from mice with MDA-MB-231 bone metastases that were treated with vehicle or S107. Data are mean ± s.e.m. Statistical analysis in **a**,**b** was by two-way ANOVA, in **c**–**f** was by one-way ANOVA with multiple comparisons and in **g** by Pearson's correlation. $^*P < 0.05$, $^{**}P < 0.01$, $^{***}P < 0.001$, $^{****}P < 0.0001$.

grip strength (**Supplementary Fig. 3f**). There was no loss of muscle weight or whole body weight, nor did the mice have changes in body composition, although mid-calf cross-sectional area was higher than in non-tumor control mice (**Supplementary Fig. 3g**), and we did not observe RyR1 modifications (**Supplementary Fig. 3h**).

Taken together, these data show that, as compared to non-tumor control animals, mice with predominantly osteolytic (MDA-MB-231 breast cancer, A549 lung cancer, PC3 prostate cancer and JJN3 multiple myeloma) and mixed osteolytic and osteoblastic bone metastases (RWGT2 lung cancer and MCF-7 breast cancer) showed lower muscle-specific force production, lower muscle strength and RyR1 modifications that are consistent with leaky channels, regardless of whether there was weight loss or reduced muscle mass as compared to that in non-tumor control mice. In contrast, mice with ZR75-1 breast cancer cells showed induction of osteoblastic bone metastases and lower muscle function but no modification of RyR1 as compared to non-tumor control mice. Of note, it takes 7 months for the ZR75-1 mice to develop bone metastases and muscle weakness, as opposed to 4–12 weeks for the same development in all of the other models we examined. The lower muscle force production in the ZR75-1 mice occurs in the absence of bone destruction and without RyR1 modifications, suggesting a mechanism distinct from the other forms of cancer in bone.

Inhibiting RyR1 Ca^{2+} leak improves muscle strength

The clinical relevance of the leaky RyR1 modifications in skeletal muscle from mice with osteolytic bone metastases is reinforced because we found the same biochemical signature of leaky RyR1 channels in skeletal muscle from humans with osteolytic breast or lung cancer that was metastatic to bone (**Fig. 1e**,**f**). The RyR1 Ca^{2+} release channel stabilizer Rycal (S107) is a small molecule in the 1,4-benzothizepine family whose structure and properties have been previously published[17]. S107 fixes leaky RyR1 channels by inhibiting oxidation-induced depletion of the channel-stabilizing subunit calstabin1 from the RyR1 complex, which stabilizes the closed state of the channel and prevents aberrant intracellular Ca^{2+} leak, thereby improving the Ca^{2+} signal for muscle force production and enhancing muscle strength and exercise capacity in rodents[10,13,17,18]. Administration of S107 (via a subcutaneous infusion pump to achieve a plasma level of 252 ± 75.1 nM; s.e.m., $n = 10$) improved forelimb grip strength and *ex vivo* muscle-specific force of the EDL in mice with breast cancer–associated bone metastases as compared to vehicle-treated mice (**Fig. 2a**,**b**). S107 prevented depletion of calstabin1 from the skeletal muscle RyR1 complex in mice with bone metastases but, as previously reported, did not prevent oxidation or nitrosylation of RyR1 (refs. 10,13) (**Fig. 2c**). S107 treatment led to higher peak tetanic Ca^{2+} in muscle fibers (**Fig. 2d**) and lower skeletal muscle RyR1 open probability (P_o) (**Fig. 2e**), consistent with decreased SR Ca^{2+} leak, than in vehicle-treated mice. The SR/ER Ca^{2+} ATPase (SERCA) pumps Ca^{2+} back into the SR, and lower SERCA activity could contribute to decreased tetanic Ca^{2+}; however, we observed no difference in SERCA activity in skeletal muscle from non-tumor mice as compared to that from mice with bone metastases (either with or without S107 treatment) (**Fig. 2f**).

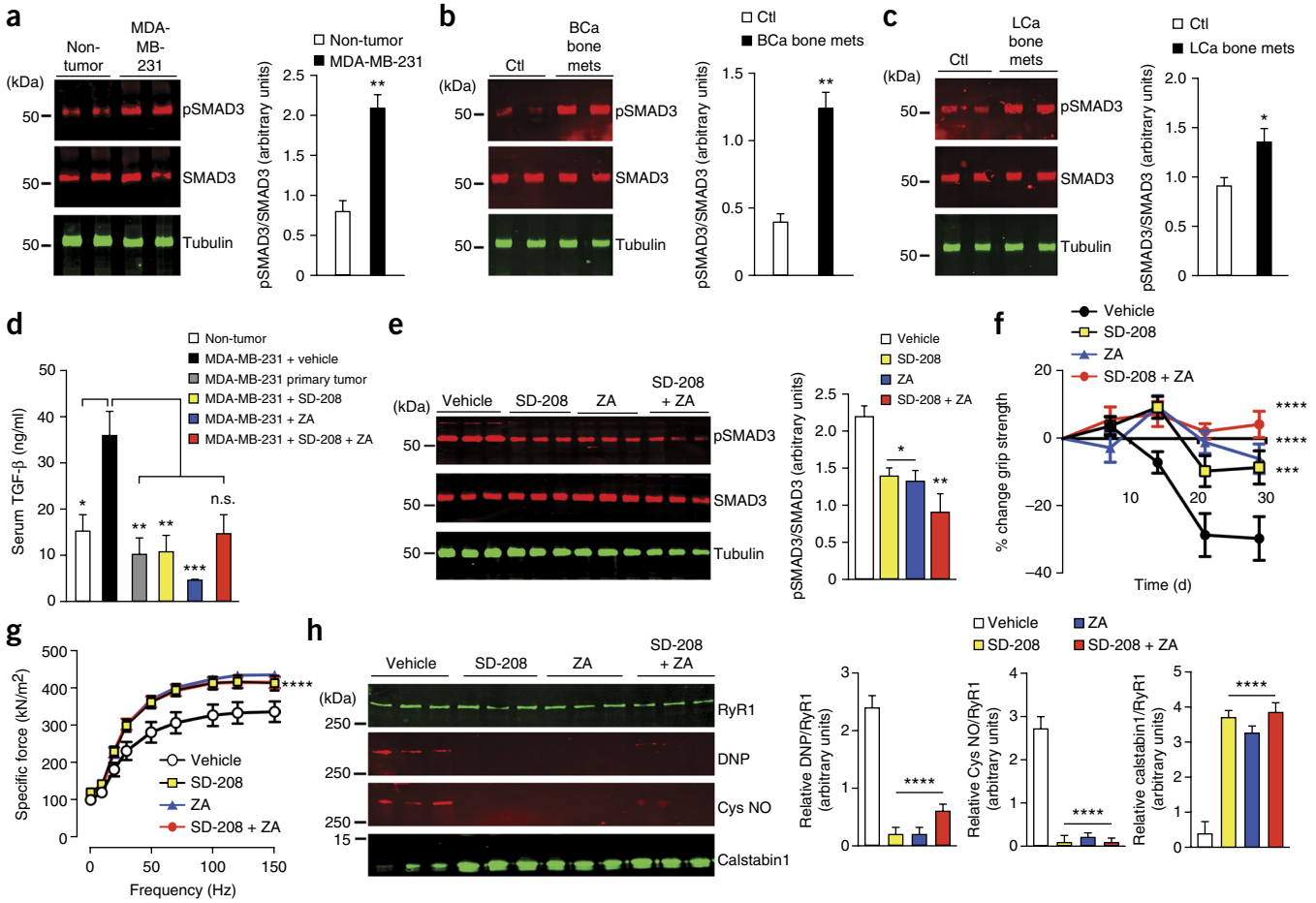

Figure 3 Blocking TGF-β signaling or inhibiting bone resorption lowers SMAD3 phosphorylation and improves muscle function. (**a**–**c**) Immunoblots of SMAD3 phosphorylation (left) and quantification (right) from muscle of mice with MDA-MB-231 bone metastases (**a**) and from muscle samples of humans with either breast cancer bone metastases (BCa bone mets) (**b**) or lung cancer bone metastases (LCa bone mets) (**c**) and their respective controls (Ctl); $n = 4$ per group. (**d**) Serum TGF-β concentration in non-tumor control mice, mice with MDA-MB-231 bone metastases, mice with MDA-MB-231 primary tumors or mice with MDA-MB-231 bone metastases receiving treatment to block TGF-β signaling (SD-208) or bone resorption (zoledronic acid (ZA)) ($n = 5$). (**e**) SMAD3 phosphorylation in mice with MDA-MB-231 bone metastases receiving either SD-208, ZA or combined therapy ($n = 3$). (**f**,**g**) *In vivo* forelimb grip strength ($n = 12$ per group) (**f**) and *ex vivo* specific force of the EDL muscle ($n = 12$ per group) (**g**) in mice treated with SD-208, ZA or a combination of both. (**h**) Immunoblot (left) and quantification (right) of RyR1 oxidation (DNP) and nitrosylation (Cys NO) and of RyR1-calstabin1 binding, as measured by coimmunoprecipitation, from EDL muscle ($n = 3$ per group). Data are mean ± s.e.m. Statistical analysis in **a**–**c** was by Student's *t*-test, in **d**,**e**,**h** was by one-way ANOVA with multiple comparisons and in **f**,**g** was by two-way ANOVA. $^{*}P < 0.05$, $^{**}P < 0.01$, $^{***}P < 0.001$, $^{****}P < 0.0001$; n.s., not significant.

S107 treatment had no effect on the development and progression of bone metastases, tumor burden, the number of osteoclasts present at the tumor bone interface (**Supplementary Fig. 4a**), body weight, or the distribution of fat and lean mass as compared to what we observed in vehicle-treated mice (**Supplementary Fig. 4b**). S107 treatment did not improve muscle mass or affect muscle fiber diameter or mid-calf cross-sectional area (**Supplementary Fig. 4c**). However, S107 treatment did eliminate the correlation between higher bone destruction and lower muscle function (**Fig. 2g**).

Calorie restriction, by reducing food intake (**Supplementary Fig. 4d**) in healthy mice for 2 weeks, led to reduced body weight and fat and lean mass, and led to lower muscle weight and reduced mid-calf cross-sectional area as compared to pair-fed mice (**Supplementary Fig. 4e**). Grip strength and *ex vivo* contractility of the EDL muscle were not affected by reduced calorie intake (**Supplementary Fig. 4f**). This shows that loss of muscle mass alone does not account for lower strength in mice with bone metastases.

Inhibiting TGF-β improves muscle strength

Bone is the largest source of TGF-β in the body[19], and TGF-β (which is deposited in bone matrix by osteoblasts) has a central role in tumor growth in bone[6,7,20,21]. TGF-β is released from mineralized bone matrix during osteoclastic resorption. This resorbing bone matrix is the primary source of TGF-β activity in mice with MDA-MB-231 bone metastases; bisphosphonate inhibition of osteoclastic bone resorption therefore effectively inhibits excess TGF-β signaling in these bone metastases[7,19]. We found that TGF-β–induced phosphorylation of the signaling factor SMAD3 (ref. 22) was higher in skeletal muscle from mice with MDA-MB-231 breast cancer bone metastases than in non-tumor control mice (**Fig. 3a**) but not in mice with MDA-MB-231 primary tumors without bone metastases (**Supplementary Fig. 5a**), consistent with a systemic effect of bone-derived TGF-β on skeletal muscle. The clinical relevance of the activation of TGF-β–mediated signaling in skeletal muscle in the presence of cancer-induced bone destruction was reinforced because SMAD3 phosphorylation was also

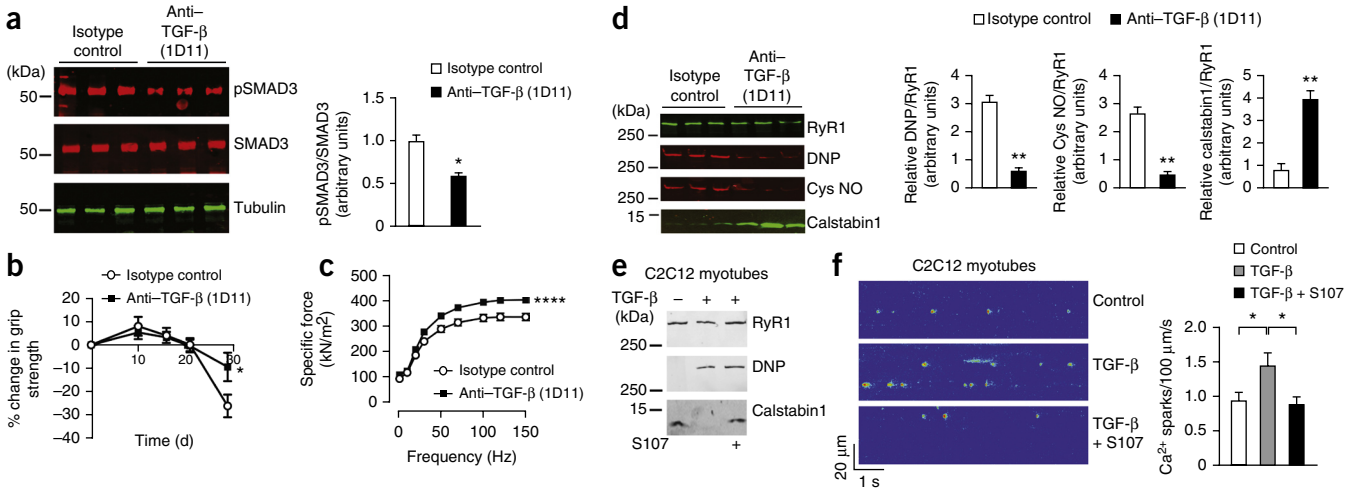

Figure 4 Blocking TGF-β ligand lowers SMAD3 phosphorylation and improves muscle function. (**a**) Immunoblot (left) and quantification (right) of SMAD3 phosphorylation in muscle from mice with MDA-MB-231 bone metastases receiving 1D11 treatment ($n = 3$). (**b**,**c**) *In vivo* forelimb grip strength (**b**) and *ex vivo* specific force of the EDL muscle (**c**) in mice treated with a TGF-β neutralizing antibody (clone 1D11) ($n = 11$ per group). (**d**) Immunoblot (left) and quantification (right) of RyR1 oxidation (DNP) and nitrosylation (Cys NO) and of RyR1-calstabin1 binding, as measured by coimmunoprecipitation, from EDL muscle ($n = 3$). (**e**) Immunoblot analysis of RyR1 oxidation and of RyR1-calstabin1 binding, as measured by coimmunoprecipitation, in C2C12 cells treated with TGF-β ± S107. (**f**) Ca^{2+} sparks in C2C12 myotubes treated with TGF-β ± S107 ($n = 52$ cells). Data are mean ± s.e.m. Statistical analysis in **a**,**d** was by Student's *t*-test, in **b**,**c** was by two-way ANOVA and in **f** was by one-way ANOVA with multiple comparisons. $^*P < 0.05$, $^{**}P < 0.01$, $^{****}P < 0.0001$.

higher in skeletal muscle from humans with breast cancer bone metastases (**Fig. 3b**) and in humans with lung cancer bone metastases than in skeletal muscle from humans without bone metastases (**Fig. 3c**). Serum TGF-β concentrations were higher in tumor-bearing mice with bone metastases, but not in those with primary breast cancer compared to non-tumor mice (**Fig. 3d**). Skeletal muscle from five additional mouse models of human cancers with osteolytic or mixed osteolytic/osteoblastic bone metastases due to A549 lung cancer, RWGT2 lung cancer, MCF-7 breast cancer, PC-3 prostate cancer, and JJN-3 multiple myeloma all showed higher SMAD3 phosphorylation, consistent with activation of TGF-β-mediated signaling in skeletal muscle compared to non-tumor control mice (**Supplementary Fig. 5a**). In contrast, the osteoblastic ZR75-1 breast cancer bone metastases did not exhibit higher SMAD3 phosphorylation in skeletal muscle compared to non-tumor control mice (**Supplementary Fig. 5a**).

Next we showed that inhibition of TGF-β improves muscle strength. We treated mice with MDA-MB-231 bone metastases with: (i) the TGF-β receptor I kinase inhibitor SD-208 (60 mg per kg body weight daily gavage); (ii) the bisphosphonate zoledronic acid (ZA) (5 µg per kg body weight; three treatments per week by subcutaneous injection), which specifically inhibits osteoclastic bone resorption and lowers TGF-β release from the bone matrix[7]; (iii) combined therapy (SD-208 + ZA); or (iv) a pan-TGF-β neutralizing antibody (clone 1D11)[23]. Serum TGF-β concentrations were decreased in MDA-MB-231 tumor-bearing mice with bone metastases treated with ZA as a consequence of lower release of TGF-β from the bone than in vehicle-treated mice (**Fig. 3d**). Bone metastases–bearing mice treated with SD-208, ZA or the combination of both, all had lower levels of skeletal muscle SMAD3 phosphorylation than observed for SMAD3 in vehicle-treated mice, indicating inhibition of TGF-β signaling (**Fig. 3e**). Both SD-208 and ZA treatment, alone and in combination, improved muscle function (forelimb grip strength and muscle-specific force of the EDL) (**Fig. 3f**,**g**) and RyR1 oxidation and nitrosylation and preserved calstabin1 binding to the RyR1 complex (**Fig. 3h**). The activity of SERCA was not affected by treatment with SD-208, ZA, or combined therapy compared to vehicle-treated mice (**Supplementary Fig. 5b**). *In vitro*, SD-208 blocked TGF-β–induced SMAD3 phosphorylation in C2C12 myotubes, a mouse myoblast cell line used for the *in vitro* study of skeletal muscle (**Supplementary Fig. 5c**). Taken together, these data show that bone-derived TGF-β has a key role in reduced muscle-specific force production and in cancer-associated muscle weakness, possibly via oxidation of RyR1.

SD-208 or ZA treatment prevented loss of skeletal muscle, body weight and lower mid-calf cross-sectional area in mice with bone metastases, and the combined therapy (SD-208 + ZA) provided an additive benefit (**Supplementary Fig. 5d**–**g**), a lower tumor burden (**Supplementary Fig. 5h**) and a lower number of osteoclasts at the tumor-bone interface compared to vehicle-treated mice (**Supplementary Fig. 5i**).

Because SD-208 is a TGF-β receptor I kinase inhibitor, it may also inhibit the effects of other TGF-β family members, including activin and myostatin. To determine the specificity of TGF-β to induce muscle weakness we treated mice with breast cancer bone metastases with a pan–TGF-β neutralizing antibody (clone 1D11)[23] or isotype control (10 mg per kg body weight (mg/kg), three times per week by intraperitoneal injection)[24]. The TGF-β–neutralizing 1D11 antibody has no effect on activin or myostatin signaling[23]. Mice with MDA-MB-231 breast cancer bone metastases treated with the 1D11 antibody showed decreased SMAD3 phosphorylation (**Fig. 4a**), increased forelimb grip strength and *ex vivo* specific force generation of the EDL muscle (**Fig. 4b**,**c**), reduced RyR1 oxidation and nitrosylation and increased binding of calstabin1 to the RyR1 complex, consistent with fixing of the leaky RyR1 channels, than in isotype antibody–treated control mice (**Fig. 4d**). 1D11 treatment lowered SMAD3 phosphorylation in TGF-β–treated C2C12 myotubes, as compared to that observed in isotype antibody control–treated cells (**Supplementary Fig. 6a**). 1D11-treated mice showed increased hindlimb muscle weight, increased body weight (due to increases in both fat and lean content) and greater mid-calf cross-sectional area than in isotype antibody–treated control mice (**Supplementary Fig. 6b**–**e**). Mice treated with 1D11 had lower bone

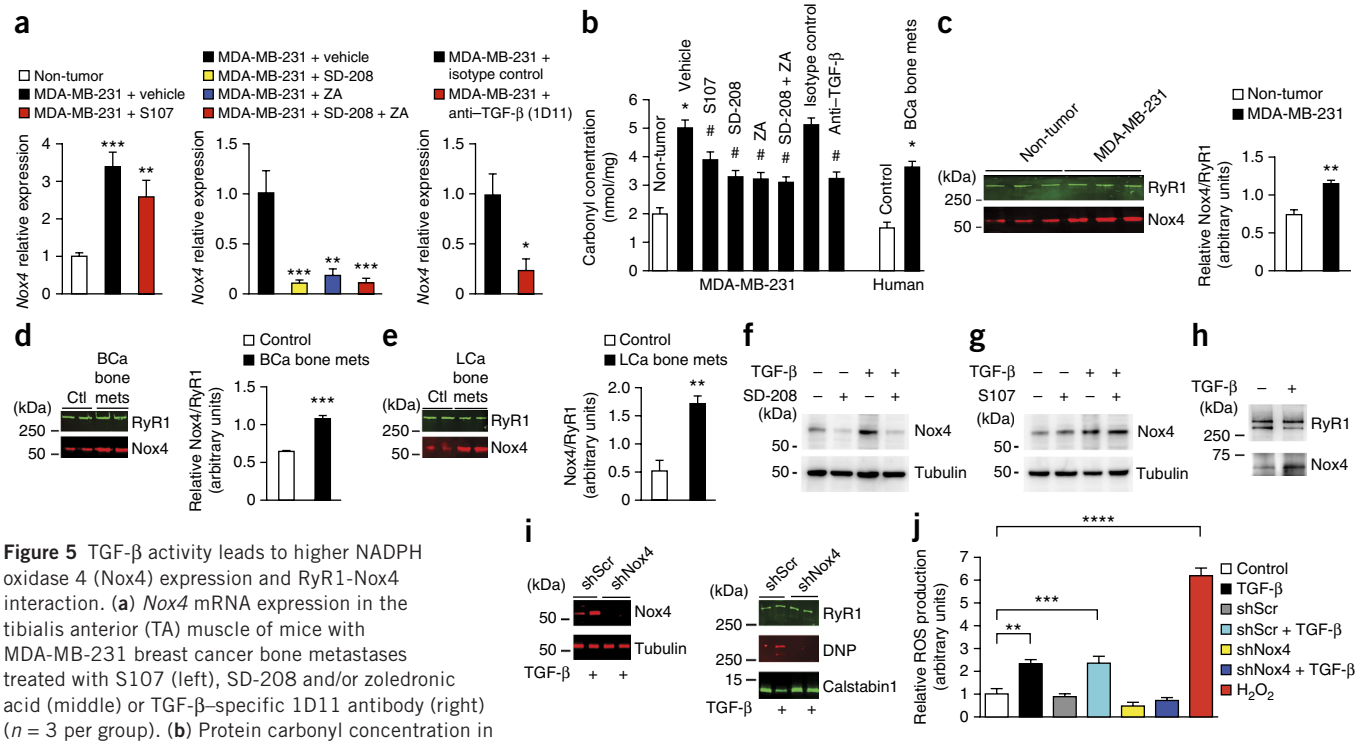

Figure 5 TGF-β activity leads to higher NADPH oxidase 4 (Nox4) expression and RyR1-Nox4 interaction. (**a**) *Nox4* mRNA expression in the tibialis anterior (TA) muscle of mice with MDA-MB-231 breast cancer bone metastases treated with S107 (left), SD-208 and/or zoledronic acid (middle) or TGF-β–specific 1D11 antibody (right) ($n = 3$ per group). (**b**) Protein carbonyl concentration in muscle from either mice with MDA-MB-231 bone metastases or humans with breast cancer and bone metastases ($n = 2$ for each group). Data are mean ± s.d. Statistical analysis was by two-way ANOVA; $^{*}P < 0.05$ as compared to non-tumor control mice or human control samples; $^{\#}P < 0.05$ as compared to vehicle-treated controls. (**c**–**e**) Immunoblot (left) and quantification (right) of Nox4 coimmunoprecipitation with RyR1 in muscle from mice with MDA-MB-231 bone metastases (**c**) ($n = 3$), muscle samples from humans with breast cancer and bone metastases (BCa bone mets) (**d**) ($n = 4$) and muscle samples from humans with lung cancer and bone metastases (LCa bone mets) (**e**) ($n = 4$) and their respective controls (in **c**, $n = 3$; in **d**,**e**, $n = 4$). (**f**,**g**) Immunoblot of Nox4 expression in C2C12 myotubes treated with either TGF-β ± SD-208 (**f**) or TGF-β ± S107 (**g**). (**h**) Immunoblot showing Nox4 coimmunoprecipitation with RyR1 in C2C12 myotubes treated with TGF-β. (**i**) Immunoblots of C2C12 cells showing either knockdown of *Nox4* using a *Nox4*-specific shRNA (left; shNox4 versus scrambled control shScr) or RyR1 oxidation (DNP) and RyR1-calstabin1 binding, as measured by co-immunoprecipitation (right). C2C12 myotubes were either untreated or treated with TGF-β. (**j**) Reactive oxygen species (ROS) generation in C2C12 myotubes ($n = 4$). H_2O_2, hydrogen peroxide. Data are mean ± s.e.m. Statistical analysis in **a**,**b**,**j** was by one-way ANOVA with multiple comparisons and in **c**–**e** was by Student's *t*-test. $^{*}P < 0.05$, $^{**}P < 0.01$, $^{***}P < 0.001$, $^{****}P < 0.0001$.

destruction (osteolytic lesion area of limbs) (**Supplementary Fig. 6f**,**g**) and lower tumor burden, and we observed no effect on the number of osteoclasts at the tumor-bone interface as compared to isotype antibody–treated control mice (**Supplementary Fig. 6h**,**i**). Taken together, these data indicate that TGF-β inhibition improves muscle function and that bone-derived TGF-β contributes to cancer-associated muscle weakness, at least in part, by inducing oxidation of RyR1.

To directly show that TGF-β is sufficient to cause RyR1 channel remodeling and intracellular Ca^{2+} leakage, we treated differentiated C2C12 myotubes with TGF-β, which induced the biochemical signature of leaky RyR1. Binding of calstabin1 to RyR1 (which fixes the RyR1-mediated leak) was restored by incubation of myotubes with S107 compared to C2C12 myotubes without TGF-β treatment (**Fig. 4e**). TGF-β treatment increased Ca^{2+} sparks in myotubes (a direct measure of RyR1-mediated SR Ca^{2+} leakage), as compared to those in C2C12 myotubes without TGF-β treatment, and the increase in the number of Ca^{2+} sparks was prevented by treatment with S107 (**Fig. 4f**). Thus, TGF-β activates a signaling pathway that leads to RyR1 oxidation and to SR Ca^{2+} leakage in skeletal muscle cells.

RyR1 oxidation is mediated by Nox4

We next sought to determine the mechanisms by which TGF-β mediates oxidation of RyR1. Nox4 is a membrane protein that transfers electrons from NADPH to oxygen (O_2) to form reactive oxygen species (ROS), which oxidize many molecules including proteins. Nox4 is expressed in skeletal muscles, including in the SR where it interacts with RyR1, resulting in its oxidation[25]. TGF-β treatment leads to higher expression of Nox4 (refs. 26–29). We found that skeletal muscle from mice with bone metastases had threefold higher *Nox4* mRNA levels than in non-tumor control mice, and S107 treatment had no effect on *Nox4* expression (**Fig. 5a**). Treatment with SD-208, ZA, SD-208 + ZA or 1D11 antibody lowered skeletal muscle *Nox4* mRNA expression as compared to that in appropriate vehicle-treated control mice (**Fig. 5a**). *Nox1* and *Nox2* mRNA were not altered in mice with MDA-MB-231 bone metastases as compared to non-tumor control mice (**Supplementary Fig. 7a**). Moreover, total protein oxidation (measured as carbonyl concentration in skeletal muscle lysates, as described in the Online Methods) was higher in skeletal muscle from mice and humans with cancer and bone metastases as compared to that from mice and humans without bone metastases. Inhibition of TGF-β signaling decreased protein oxidation in the mice with bone metastases as compared to that in vehicle-treated mice (**Fig. 5b**). Indeed, total protein oxidation (carbonyl concentration) was higher in skeletal muscle from all bone metastasis models associated with bone destruction, but not in skeletal muscle from mice with primary MDA-MB-231 breast cancer without bone metastases, or in those with osteoblastic ZR75-1 bone metastases as compared to non-tumor control mice. These data indicate that tumor-induced bone

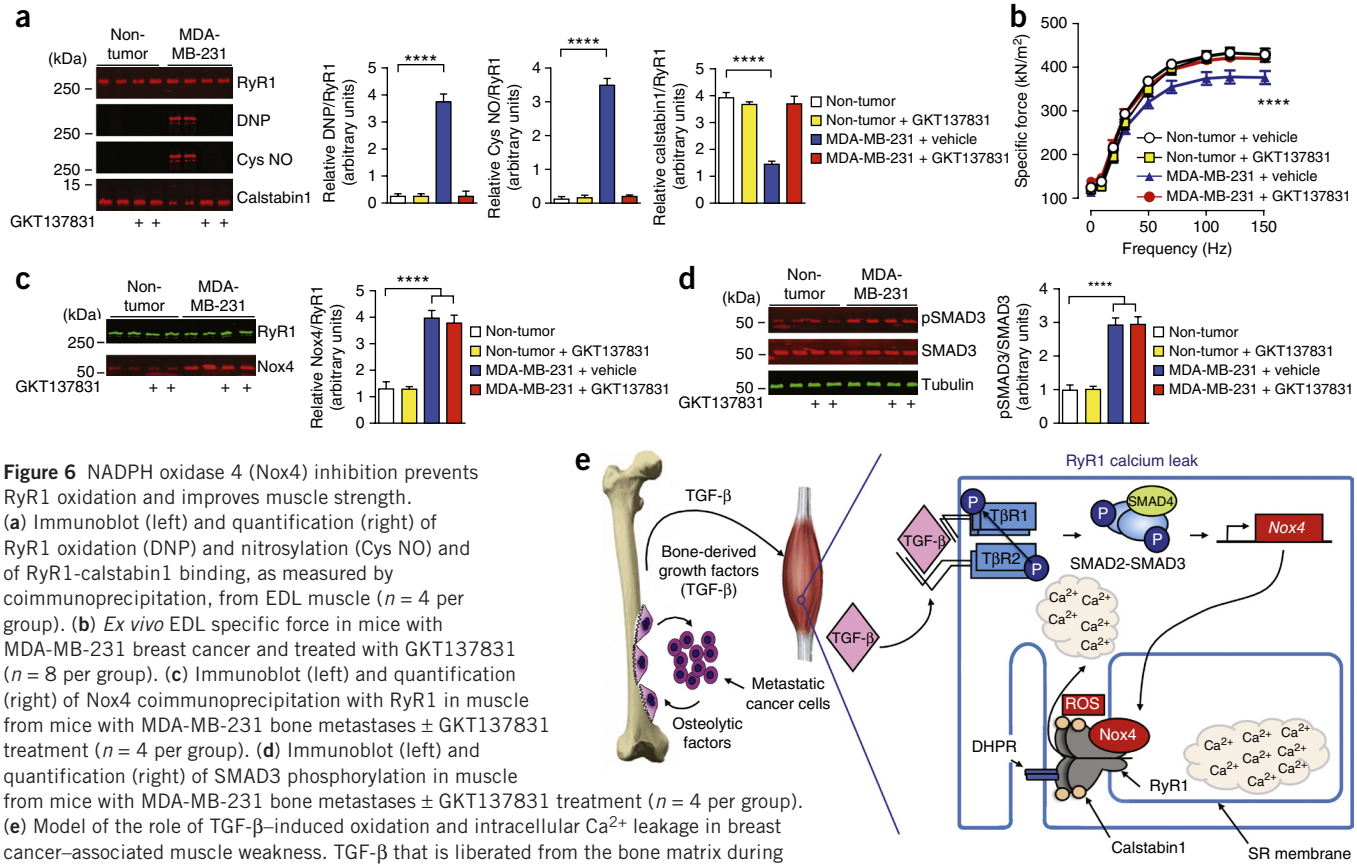

Figure 6 NADPH oxidase 4 (Nox4) inhibition prevents RyR1 oxidation and improves muscle strength. (**a**) Immunoblot (left) and quantification (right) of RyR1 oxidation (DNP) and nitrosylation (Cys NO) and of RyR1-calstabin1 binding, as measured by coimmunoprecipitation, from EDL muscle ($n = 4$ per group). (**b**) *Ex vivo* EDL specific force in mice with MDA-MB-231 breast cancer and treated with GKT137831 ($n = 8$ per group). (**c**) Immunoblot (left) and quantification (right) of Nox4 coimmunoprecipitation with RyR1 in muscle from mice with MDA-MB-231 bone metastases ± GKT137831 treatment ($n = 4$ per group). (**d**) Immunoblot (left) and quantification (right) of SMAD3 phosphorylation in muscle from mice with MDA-MB-231 bone metastases ± GKT137831 treatment ($n = 4$ per group). (**e**) Model of the role of TGF-β–induced oxidation and intracellular Ca^{2+} leakage in breast cancer–associated muscle weakness. TGF-β that is liberated from the bone matrix during osteolytic bone destruction drives the expression of *Nox4* in muscle via SMAD2-SMAD3 signaling, and Nox4 activity produces ROS. Oxidation of RyR1 leads to loss of calstabin1 binding and Ca^{2+} leakage from the sarcoplasmic reticulum, thereby depleting intracellular Ca^{2+} stores and causing decreased muscle-specific force. Inhibiting TGF-β release from the bone matrix, TGF-β signaling, Nox4 activity or RyR1-mediated SR Ca^{2+} leakage improved muscle strength. DHPR, dihydropyridine receptor; TβR1, TGF-β receptor 1; TβR2, TGF-β receptor 2. Data are mean ± s.e.m. Statistical analysis in **a**,**c**,**d** was by one-way ANOVA with multiple comparisons and in **b** was by two-way ANOVA. ****$P < 0.0001$.

destruction is associated with oxidation of skeletal muscle. Moreover, inhibiting TGF-β release, or signaling, or blocking Nox4 lowered the carbonyl concentration in skeletal muscle lysates from mice with tumors metastatic to bone (**Supplementary Table 3**), indicating the importance of TGF-β and Nox4 in the oxidation of skeletal muscle proteins in the setting of tumors metastatic to bone.

Nox4 coimmunoprecipitated with RyR1 specifically from skeletal muscle from mice with MDA-MB-231 breast cancer bone metastases (**Fig. 5c**) and from skeletal muscle samples from humans with breast cancer bone metastases or humans with lung cancer bone metastases (**Fig. 5d**,**e**). The amount of Nox4 that coimmunoprecipitated with RyR1 was higher in muscles from mice with breast cancer bone metastases (**Fig. 5c** and **Supplementary Fig. 7b**), from humans with breast cancer bone metastases (**Fig. 5d**), from mice with lung cancer bone metastases (**Supplementary Fig. 7b**), from humans with lung cancer bone metastases (**Fig. 5e**), from mice with PC-3 prostate cancer and from mice with JJN-3 multiple myeloma as compared to that in non-tumor controls. Skeletal muscle from mice with MDA-MB-231 primary breast cancer without bone metastases or mice with ZR75-1 osteoblastic breast cancer bone metastases that were not associated with RyR1 oxidation did not show RyR1 and Nox4 coimmunoprecipitation greater than that observed in non-tumor control mice (**Supplementary Fig. 7b**).

TGF-β treatment resulted in higher Nox4 protein expression in C2C12 myotubes as compared to that in C2C12 myotubes without TGF-β treatment, and this was blocked by treatment with SD-208, but not S107 (**Fig. 5f**,**g**). TGF-β treatment led to increased coimmunoprecipitation of Nox4 with RyR1 channels in myotubes (**Fig. 5h**). Moreover, *Nox4* knockdown in myotubes prevented TGF-β–induced RyR1 oxidation and loss of calstabin1 binding to RyR1 (**Fig. 5i**) and prevented TGF-β–induced ROS production compared to that observed in C2C12 myotubes without TGF-β treatment (**Fig. 5j**).

To test the *in vivo* effect of Nox4 inhibition, we treated mice with MDA-MB-231 breast cancer bone metastases with the Nox1 and Nox4 inhibitor GKT137831 (ref. 30) (60 mg/kg/d or vehicle (1.2% methylcellulose + 0.1% polysorbate 80), administered by daily oral gavage). GKT137831 treatment prevented skeletal muscle oxidation and nitrosylation of RyR1, restored calstabin1 binding (**Fig. 6a**) and improved EDL muscle–specific force (**Fig. 6b**). GKT137831 had no effect on the amount of skeletal muscle Nox4 associated with RyR1 (**Fig. 6c**), and it did not block upstream TGF-β signaling, as skeletal muscle SMAD3 phosphorylation was not affected in comparison to that in vehicle-treated mice (**Fig. 6d**). In mice with bone metastases, GKT137831 had no effect on osteolytic lesion size, muscle mass, body weight, body composition or grip strength, probably reflecting the high variability of the latter measurement, which also has a behavioral component (**Supplementary Fig. 7c–h**).

No contribution by non-bone sites or fibrosis to weakness

The tumor-bone microenvironment appears to be the most significant determinant of muscle weakness in this model, as the bisphosphonate

zoledronic acid prevented oxidation of RyR1 and muscle weakness by blocking release of TGF-β from bone. Consistent with this, tumor burden at other metastatic sites was insignificant. In mice with MDA-MB-231 breast cancer and bone metastases, the tumor burden in bone was at least 12-fold higher than in all other organs (**Supplementary Fig. 8a**). Further, there was no evidence of skeletal muscle fibrosis (**Supplementary Fig. 8b**), supporting the finding that muscle weakness is due to tumor-induced bone destruction.

To validate the role that higher bone resorption has in skeletal muscle weakness in the absence of cancer, we tested a mouse model of CED. This disease is an inherited human skeletal disease characterized by increased bone destruction and skeletal fragility and is often associated with TGF-β1 mutations that cause an increase in TGF-β activity by increased activation or secretion of TGF-β (refs. 31,32). In the mouse model of CED, a mutant TGF-β1 (H222D), identified from some humans with CED, is expressed under the control of the 2.3-kb type I collagen promoter. These mice show higher bone destruction and fractures that is abrogated by TGF-β signaling blockade using a TGF-β receptor I inhibitor. CED mice show higher concentrations of active TGF-β in the bone microenvironment and higher bone resorption as compared to littermate controls[8]. Radiography of the lower hindlimb of CED mice showed osteolysis and diaphyseal dysplasia, similarly to that observed in previous reports, as compared to littermate controls[8] (**Supplementary Fig. 8c**). Consistent with higher TGF-β signaling, skeletal muscle from CED mice had higher SMAD3 phosphorylation than that of littermate control mice (**Supplementary Fig. 8d**). CED mice also had lower *ex vivo* specific force of the EDL muscle as compared to that in non-affected littermate control mice (**Supplementary Fig. 8e**), consistent with previous reports in which treatment of mice with recombinant TGF-β resulted in lower skeletal muscle–specific force[33]. Skeletal muscle from CED mice also showed higher levels of RyR1 oxidation and nitrosylation, lower amounts of calstabin1 bound to RyR1 and higher levels of Nox4-RyR1 binding as compared to those in littermate control mice (**Supplementary Fig. 8f**). These results were similar to those we observed in mice with osteolytic bone metastases.

Taken together, our data in models of osteolytic bone metastases show that TGF-β, released from the bone matrix due to elevated catabolism of the tissue, upregulates *Nox4* and causes higher association of Nox4 protein with RyR1, resulting in oxidation of the channel. RyR1 oxidation causes an SR Ca^{2+} leak that lowers tetanic Ca^{2+}, impairs muscle force production and contributes to muscle weakness in cancer with bone metastases (**Fig. 6e**). Similar skeletal muscle dysfunction, higher skeletal muscle TGF-β activity and RyR1 oxidation via upregulation of Nox4 were observed in a nonmalignant bone disorder associated with increased bone destruction (CED mice).

DISCUSSION

The present study provides novel mechanistic insights into the causes of cancer-associated muscle weakness with potential therapeutic implications for the following reasons: (i) in addition to loss of muscle mass, we now show that there is a specific loss of muscle function in the setting of bone metastases and that muscle weakness can occur without the loss of muscle mass; (ii) an important determinant of muscle weakness in metastatic cancer is bone destruction; (iii) a key mediator of muscle weakness is TGF-β that is released from bone as a consequence of tumor-induced osteoclast activity in the tumor-bone microenvironment; (iv) TGF-β activates Nox4 in skeletal muscle, causing protein oxidation; (v) skeletal muscle RyR1 Ca^{2+}-release channels are a target of the oxidative stress that results from the upregulation of Nox4 by TGF-β; (vi) RyR1 oxidation results in intracellular Ca^{2+} leakage that lowers tetanic Ca^{2+} and weakens muscle force production; (vii) activation of TGF-β signaling, upregulation of Nox4 and the biochemical signature of oxidation-induced skeletal muscle RyR1 leakage were present in humans with breast or lung cancer metastatic to bone and in six out of seven mouse models of human osteolytic bone metastases, including those of breast, lung and prostate cancers, as well as that of multiple myeloma; and (viii) inhibition of RyR1-mediated SR Ca^{2+} leakage, inhibition of TGF-β activity, inhibition of TGF-β release from bone or inhibition of Nox4 improved muscle force production, suggesting that these processes could be potential therapeutic targets for cancer-associated muscle weakness in the setting of bone destruction due to metastases. Furthermore, this mechanism of muscle weakness was also observed in a nonmalignant bone disorder that is characterized by increased bone destruction and TGF-β activity. Thus, targeting skeletal muscle weakness caused by the TGF-β–Nox4–RyR1 axis represents a novel therapeutic approach to improving the quality of life in cancer patients with muscle weakness associated with increased bone destruction.

In addition to RyR1, other proteins involved in muscle contraction were oxidized in skeletal muscle from mice with bone metastases, suggesting that there may be other contributing factors to cancer-associated muscle weakness. Inhibition of the activin receptor reduces cachexia and cardiac atrophy and improves survival in mice with experimental colon cancer cachexia (C26 model)[34]. Another target under investigation for cachexia is myostatin, a negative regulator of muscle mass[35]. Myostatin antagonism with a myostatin-specific antibody improves the contractile properties of dystrophic muscle in the *mdx* mouse model of Duchenne muscular dystrophy[36]. However, myostatin-deficient mice show a decrease in muscle contractile force that is age, sex and muscle dependent[2,3]. Our data do not exclude the possibility that other bone-derived factor(s) released as a consequence of osteoclastic bone resorption may induce TGF-β production from other sources or that they may themselves contribute to skeletal muscle dysfunction or loss of muscle mass. Furthermore, the data do not indicate that the mechanism described herein is the exclusive one for cancer-associated muscle weakness but rather suggests that this is one such mechanism that may be operational in humans with bone metastases.

Taken together, our data provide a link between bone and skeletal muscle by showing that factors elaborated from bone can profoundly affect muscle function systemically. Our findings in mouse models of breast cancer, lung cancer, prostate cancer and multiple myeloma, and in humans with breast cancer or lung cancer that is associated with bone destruction, suggest a generalized but not exclusive role for the tumor-bone microenvironment in the generation of cancer-associated skeletal muscle weakness. Finally, the data indicate that muscle dysfunction can occur before the loss of muscle mass (cachexia) and suggest that a spectrum of muscle dysfunction, ranging from muscle weakness to profound cachexia, exists in humans with bone metastases. Indeed, muscle weakness may occur in states of increased bone destruction, even in the absence of cancer. Clinical studies to characterize this spectrum of muscle dysfunction are justified to allow for the development and testing of treatments to ameliorate the muscle weakness that is associated with cancer and associated bone disorders.

METHODS

Methods and any associated references are available in the online version of the paper.

Note: Any Supplementary Information and Source Data files are available in the online version of the paper.

ACKNOWLEDGMENTS

This work was supported by the US National Institutes of Health (NIH) (grant U01CA143057 (T.A.G.) from the National Cancer Institute (NCI) Tumor Microenvironment Network, NCI-R01CA69158 (T.A.G.), NCI-R21CA179017 (G.D.R.), NHLBI-R01HL061503 (A.R.M.), NHLBI-R01HL102040 (A.R.M.), NIAMS-R01AR060037 (A.R.M.), NIH T32 HL120826 (A.R.M.), NINDS-R25NS076445 (A.R.M.), NIH-NINDS R25NS076445 (A.H.), NIH-NIAMS R01AR063943 (X.C.), and NIH-NHLBI T35 HL110854-01 (S.C. and P.K.)), the Susan G. Komen Foundation (grant SAC110013; T.A.G.), the Indiana Economic Development Grant (T.A.G.), the Jerry and Peggy Throgmartin Endowment of the Indiana University Simon Cancer Center (T.A.G.), the Indiana University Simon Cancer Center Breast Cancer Program (T.A.G.), the American Cancer Society and Indiana University Simon Cancer Center (grant IRG-84-002-28; D.L.W.), the Indiana University Health Strategic Research Initiative in Oncology (D.L.W.), the VA Merit Review Award (G.D.R.), the Fondation Leducq (A.R.M.), the Ellison Foundation (A.R.M.), the Swedish Heart Lung Foundation and Stockholm County Council (D.C.A.) and a generous donation from the Withycombe family (T.A.G.). Camurati-Engelmann disease (CED) mice were previously described and provided by X. Cao (Johns Hopkins, Baltimore, MD).

AUTHOR CONTRIBUTIONS

All contributing authors have agreed to submission of this manuscript for publication. T.A.G. and A.R.M. conceived of the study. D.L.W., K.S.M., A.R.M. and T.A.G. designed and performed experiments, analyzed data and interpreted results. S.R., W.X., D.C.A., S.J., M.N., A.C., L.E.W., A.W., A.H., A.U., T.T., S.C., F.A.W. and P.K. performed experiments. M.S.B. analyzed data. G.D.R. and F.A.W. designed experiments and interpreted results. G.Z., X.W. and X.C. provided the CED mice and reviewed the results. D.L.W., K.S.M., A.R.M. and T.A.G. wrote the manuscript.

COMPETING FINANCIAL INTERESTS

The authors declare competing financial interests: details are available in the online version of the paper.

1. Fearon, K.C., Glass, D.J. & Guttridge, D.C. Cancer cachexia: mediators, signaling and metabolic pathways. *Cell Metab.* **16**, 153–166 (2012).
2. Gentry, B.A., Ferreira, J.A., Phillips, C.L. & Brown, M. Hindlimb skeletal muscle function in myostatin-deficient mice. *Muscle Nerve* **43**, 49–57 (2011).
3. Mendias, C.L., Marcin, J.E., Calerdon, D.R. & Faulkner, J.A. Contractile properties of EDL and soleus muscles of myostatin-deficient mice. *J. Appl. Physiol.* **101**, 898–905 (2006).
4. Weilbaecher, K.N., Guise, T.A. & McCauley, L.K. Cancer to bone: a fatal attraction. *Nat. Rev. Cancer* **11**, 411–425 (2011).
5. Coleman, R.E. *et al.* Metastasis and bone loss: advancing treatment and prevention. *Cancer Treat. Rev.* **36**, 615–620 (2010).
6. Kang, Y. *et al.* Breast cancer bone metastasis mediated by the Smad tumor suppressor pathway. *Proc. Natl. Acad. Sci. USA* **102**, 13909–13914 (2005).
7. Korpal, M. *et al.* Imaging transforming growth factor-β signaling dynamics and therapeutic response in breast cancer bone metastasis. *Nat. Med.* **15**, 960–966 (2009).
8. Tang, Y. *et al.* TGF-β1–induced migration of bone mesenchymal stem cells couples bone resorption with formation. *Nat. Med.* **15**, 757–765 (2009).
9. Zalk, R., Lehnart, S.E. & Marks, A.R. Modulation of the ryanodine receptor and intracellular calcium. *Annu. Rev. Biochem.* **76**, 367–385 (2007).
10. Andersson, D.C. *et al.* Ryanodine receptor oxidation causes intracellular calcium leak and muscle weakness in aging. *Cell Metab.* **14**, 196–207 (2011).
11. Guise, T.A. *et al.* Evidence for a causal role of parathyroid hormone–related protein in the pathogenesis of human breast cancer–mediated osteolysis. *J. Clin. Invest.* **98**, 1544–1549 (1996).
12. Vera-Ramirez, L. *et al.* Free radicals in breast carcinogenesis, breast cancer progression and cancer stem cells. Biological bases to develop oxidative-based therapies. *Crit. Rev. Oncol. Hematol.* **80**, 347–368 (2011).
13. Bellinger, A.M. *et al.* Hypernitrosylated ryanodine receptor calcium release channels are leaky in dystrophic muscle. *Nat. Med.* **15**, 325–330 (2009).
14. Lu, X. & Kang, Y. Efficient acquisition of dual metastasis organotropism to bone and lung through stable spontaneous fusion between MDA-MB-231 variants. *Proc. Natl. Acad. Sci. USA* **106**, 9385–9390 (2009).
15. Guise, T.A., Yoneda, T., Yates, A.J. & Mundy, G.R. The combined effect of tumor-produced parathyroid hormone–related protein and transforming growth factor-α enhance hypercalcemia *in vivo* and bone resorption *in vitro*. *J. Clin. Endocrinol. Metab.* **77**, 40–45 (1993).
16. Hjorth-Hansen, H. *et al.* Marked osteoblastopenia and reduced bone formation in a model of multiple myeloma bone disease in severe combined immunodeficiency mice. *J. Bone Miner. Res.* **14**, 256–263 (1999).
17. Bellinger, A.M. *et al.* Remodeling of ryanodine receptor complex causes 'leaky' channels: a molecular mechanism for decreased exercise capacity. *Proc. Natl. Acad. Sci. USA* **105**, 2198–2202 (2008).
18. Andersson, D.C. & Marks, A.R. Fixing ryanodine receptor Ca leak: a novel therapeutic strategy for contractile failure in heart and skeletal muscle. *Drug Discov. Today Dis. Mech.* **7**, e151–e157 (2010).
19. Dallas, S.L., Rosser, J.L., Mundy, G.R. & Bonewald, L.F. Proteolysis of latent transforming growth factor-β (TGF-β)-binding protein-1 by osteoclasts. A cellular mechanism for release of TGF-β from bone matrix. *J. Biol. Chem.* **277**, 21352–21360 (2002).
20. Kang, Y. *et al.* A multigenic program mediating breast cancer metastasis to bone. *Cancer Cell* **3**, 537–549 (2003).
21. Yin, J.J. *et al.* TGF-β signaling blockade inhibits PTHrP secretion by breast cancer cells and bone metastases development. *J. Clin. Invest.* **103**, 197–206 (1999).
22. Shi, Y. & Massagué, J. Mechanisms of TGF-β signaling from cell membrane to the nucleus. *Cell* **113**, 685–700 (2003).
23. Dasch, J.R., Pace, D.R., Waegell, W., Inenaga, D. & Ellingsworth, L. Monoclonal antibodies recognizing transforming growth factor–β. Bioactivity neutralization and transforming growth factor β2 affinity purification. *J. Immunol.* **142**, 1536–1541 (1989).
24. Biswas, S. *et al.* Anti–transforming growth factor ss antibody treatment rescues bone loss and prevents breast cancer metastasis to bone. *PLoS ONE* **6**, e27090 (2011).
25. Sun, Q.A. *et al.* Oxygen-coupled redox regulation of the skeletal muscle ryanodine receptor-Ca^{2+} release channel by NADPH oxidase 4. *Proc. Natl. Acad. Sci. USA* **108**, 16098–16103 (2011).
26. Carmona-Cuenca, I. *et al.* Upregulation of the NADPH oxidase NOX4 by TGF-β in hepatocytes is required for its pro-apoptotic activity. *J. Hepatol.* **49**, 965–976 (2008).
27. Hubackova, S., Krejcikova, K., Bartek, J. & Hodny, Z. IL1- and TGF-β–Nox4 signaling, oxidative stress and DNA damage response are shared features of replicative, oncogene-induced and drug-induced paracrine 'bystander senescence'. *Aging (Albany NY)* **4**, 932–951 (2012).
28. Michaeloudes, C., Sukkar, M.B., Khorasani, N.M., Bhavsar, P.K. & Chung, K.F. TGF-β regulates Nox4, MnSOD and catalase expression and IL-6 release in airway smooth muscle cells. *Am. J. Physiol. Lung Cell. Mol. Physiol.* **300**, L295–L304 (2011).
29. Yan, F. *et al.* Nox4 and redox signaling mediate TGF-β–induced endothelial cell apoptosis and phenotypic switch. *Cell Death Dis.* **5**, e1010 (2014).
30. Jiang, J.X. *et al.* Liver fibrosis and hepatocyte apoptosis are attenuated by GKT137831, a novel NOX4/NOX1 inhibitor *in vivo*. *Free Radic. Biol. Med.* **53**, 289–296 (2012).
31. Janssens, K. *et al.* Mutations in the gene encoding the latency-associated peptide of TGF-β1 cause Camurati-Engelmann disease. *Nat. Genet.* **26**, 273–275 (2000).
32. Janssens, K., ten Dijke, P., Ralston, S.H., Bergmann, C. & Van Hul, W. Transforming growth factor-β1 mutations in Camurati-Engelmann disease lead to increased signaling by altering either activation or secretion of the mutant protein. *J. Biol. Chem.* **278**, 7718–7724 (2003).
33. Mendias, C.L. *et al.* Transforming growth factor-β induces skeletal muscle atrophy and fibrosis through the induction of atrogin-1 and scleraxis. *Muscle Nerve* **45**, 55–59 (2012).
34. Zhou, X. *et al.* Reversal of cancer cachexia and muscle wasting by ActRIIB antagonism leads to prolonged survival. *Cell* **142**, 531–543 (2010).
35. McPherron, A.C., Lawler, A.M. & Lee, S.J. Regulation of skeletal muscle mass in mice by a new TGF-β superfamily member. *Nature* **387**, 83–90 (1997).
36. Bogdanovich, S. *et al.* Functional improvement of dystrophic muscle by myostatin blockade. *Nature* **420**, 418–421 (2002).

ONLINE METHODS

Animals. Female athymic nude mice were obtained from Harlan (Indianapolis, IN) and female CB.17 SCID mice were obtained from Charles River (Hollister, CA) at 5 weeks of age. 6-week-old male CED and littermate control animals were used for experiments. All experiments with animals were performed at Indiana University and approved by Indiana University's Institutional Animal Care and Use Committee (IACUC). Each animal experiment was performed once unless otherwise stated.

Ethics statement. In all studies, mice were handled and euthanized in accordance with approved institutional, national and international guidelines.

Materials. Recombinant human TGF-β1 was purchased from R&D Systems. SD-208 was obtained from Epichem Pty Ltd (Bentley, WA). Zoledronic acid (Zometa) was obtained from Novartis (Cambridge, MA). Rycal S107 (S107-HCl, FW 245.77) was synthesized as previously described[17,37]. Anti–TGF-β antibody clone 1D11.16.8 (1D11) and mouse IgG1 isotype control (MOPC-21; unknown specificity) were obtained from BioXCell (West Lebanon, NH). Nox4 inhibitor (GKT137831) was obtained from Ark Pharm, Inc. (Libertyville, IL). Antibodies: Anti-RyR (Affinity Bioreagents, cat. MA3-916, Golden, CO; 1:2,000), anti–Cys NO antibody (Sigma, cat. N0409, St. Louis, MO; 1:2,000), anti-calstabin antibody (Santa Cruz Biotechnology, cat. sc-6173, Santa Cruz, CA; 1:2,500), anti-DNP (Oxyblot, Millipore, Darmstadt, Germany; 1:250), anti-pSMAD3 (Abcam, cat. ab40854, Cambridge, UK; 1:1,000), anti-SMAD3 (Abcam, cat. 52903, Cambridge, UK; 1:1,000), anti-Nox4 (Abcam, cat. 109225, Cambridge, UK; 1:1,000), anti-GAPDH (Sigma, cat. G8795, St. Louis, MO; 1:500) and anti-tubulin (Sigma, cat. 8203, St. Louis, MO; 1:500 each). Fluo-4 a.m. and Fura-red were obtained from Invitrogen/Molecular probes (cat. F-14201 and cat. F-3020, Eugene, OR).

Cell culture. MDA-MB-231 breast cancer cells[38] (HTB-26, American Type Culture Collection (ATCC), Manassas, VA), MCF-7 breast cancer cells[39] (HTB-22, ATCC), ZR75-1 breast cancer cells[40] (CRL-1500, ATCC), PC-3 prostate cancer cells[41] (CRL-1435, ATCC) and RWGT2 lung cancer cells[15,42] (isolated from bone metastases by T.A.G. as reported[15]) were cultured in Dulbecco's modified Eagle's media (DMEM) (Hyclone, Logan, UT) containing 10% heat-inactivated FBS (FBS) (Hyclone). JJN-3 multiple myeloma cells[43] (ACC 541, Deutsche Sammlung von Mikroorganismen und Zellkulturen GmbH) were cultured in RPMI 1640 (Invitrogen, Grand Island, NY) containing 10% heat-inactivated FBS. A549 cancer cells (CCL-185, ATCC) were cultured in 1640 RPMI (Hyclone) containing 10% heat-inactivated FBS. C2C12 myoblast cells (CRL-1772, ATCC) were cultured subconfluently in DMEM containing 10% heat-inactivated FBS. C2C12 myoblasts were differentiated into myotubes by culture in DMEM containing 2% heat-inactivated horse serum (HS) (Hyclone). All cells were maintained at 37 °C with 5% CO_2 in a humidified chamber. All cells were verified to be free of mycoplasma contamination via routine PCR testing. No independent verification was completed. Cells treated with recombinant human TGF-β1 (R&D Systems, Minneapolis, MN) were starved in DMEM (no serum) for 16–20 h and 5 ng/ml TGF-β1 was added to cells in DMEM.

***In vivo* models.** Intracardiac inoculation of tumor cells was performed as previously described[11,38] into 4-week-old female athymic nude mice. Tumor cells (MDA-MB-231 and A549) were trypsinized, washed twice and resuspended in PBS to a final concentration of 10^5 cells in 100 µl. 100,000 cells were inoculated into each animal. Animals were anesthetized with ketamine and xylazine and positioned ventral side up. MDA-MB-231 or A549 cells were inoculated into the left ventricle by percutaneous injection using a 26-gauge needle. Visualization of bright red blood entering the hub of the needle in a pulsatile fashion indicated a correct position in the left cardiac ventricle. Animals were euthanized at 4 weeks after inoculation.

Mammary fat pad tumor inoculation was performed on 4-week-old female athymic nude mice. Tumor cells (MDA-MB-231) were trypsinized, washed twice and resuspended in PBS to a final concentration of 10^6 cells in 100 µl. 1,000,000 cells were inoculated into each animal. Mice were anesthetized with ketamine and xylazine and inoculated in the upper mammary fat pad using a 27-gauge needle. Animals were euthanized at 4 weeks after inoculation.

Intra-tibial inoculation of tumor cells was performed on 4-week-old female CB.17 SCID mice. Tumor cells (JJN-3) were trypsinized, washed twice and resuspended in PBS to a final concentration of 10^5 cells in 20 µl. 100,000 cells were inoculated into each animal. Mice were anesthetized with ketamine and xylazine and inoculated in the proximal tibia using a 27-gauge needle. Animals were euthanized at 34 d after inoculation.

Radiography. Osteolytic lesions were analyzed by radiography using a Kubtec digital X-ray imager (Kubtec, Milford, CT). Mice were imaged in a prone position at 2.7× magnification. Osteolytic lesion area was quantified using BioQuant software v14.1.6 (Bioquant Image Analysis Corporation, Nashville, TN). The investigators were blinded to treatment of subjects.

Bone histology and histomorphometry. Forelimbs, hindlimbs and spines of the mice were collected upon euthanasia and fixed in 10% neutral buffered formalin for 48 h and decalcified in 10% EDTA for 2 weeks. After decalcification, tissues were processed in a Shandon Excelsior automated tissue processor (Thermo Fisher Scientific, Grand Island, NY) and embedded in paraffin wax for sectioning. Longitudinal, mid-sagittal sections 3.5 µm in thickness from the tibia, femur, humerus and lumbar spines were cut using an automated Microm HM 355 S microtome (Thermo Fisher Scientific). Tissue sections were stained with hematoxylin and eosin (H&E) and prepared for histomorphometric analysis. All sections were viewed on a Leica DM2500 compound microscope (W. Nuhsbaum Inc., McHenry, IL) with Q-imaging micropublisher cooled CCD color digital camera. Images were captured and analyzed using BioQuant software v14.1.6 (Bioquant Image Analysis Corporation). Tumor burden per mouse, defined as the area of bone occupied by the cancer cells, was calculated at the tibia, femur and humerus at 50× magnification on H&E-stained sections, as previously described[38]. Osteoclast number at the tumor-bone interface (OCL/mm bone surface) in the femur, tibia and humerus was measured on tartrate-resistant acid phosphatase (TRAP)-stained slides at 200× magnification. The investigators were blinded to treatment of subjects.

Dual energy X-ray absorptiometry. Body composition was determined using a PIXImus mouse densitometer (GE Lunar II, Faxitron Corp., Tucson, AZ). The densitometer was calibrated with a plastic-embedded mouse phantom before use. Mice were anesthetized and placed on an adhesive tray in a prone position with limbs spread. Total body measurement was performed excluding the calvarium, mandible and teeth. Values were expressed as percentage change over baseline scan. The investigators were blinded to treatment of subjects.

Micro-computed tomography measurement of cross-sectional muscle area (muscle method). Mouse legs from control and tumor-inoculated mice were scanned using a VIVACT40 (SCANCO Medical, Wayne, PA) to measure muscle cross-sectional area. Both the tumor inoculated and the contralateral legs were scanned starting at the level of the tibio-fibular joint for 4–5-mm length under general inhalation anesthesia. Scanning parameters of 45 kVp, 133 µA and 620-ms integration time were used as a standard setting to optimize the contrast between muscle and fat tissue. Lower muscle cross-sectional area was reported as the difference between the inoculated versus the contralateral control. The investigators were blinded to treatment of subjects.

Micro-computed tomography (micro-CT) (bone method). microCT imaging was performed on the distal femur and the proximal tibia using a VIVACT-40 (Scanco Medical). Scans were acquired using a 17.5-μm^3 isotropic voxel size, 55-kVp peak X-ray tube potential, 200-ms integration time and were subjected to Gaussian filtration. Total bone volume was evaluated at the distal epiphysis and metaphysis of the femur in a region that spanned 3.5 mm and at the proximal epiphysis and metaphysis of the tibia in a region that spanned 2.8 mm. A threshold of 160 was used to manually delineate bone from surrounding soft tissue. The investigators were blinded to treatment of subjects.

Grip strength. Forelimb grip strength was assessed by allowing each mouse to grab a wire mesh attached to a force transducer (Bioseb, Vitrolles, France) that records the peak force generated as the mouse is pulled by the tail horizontally

away from the mesh[13,44]. We performed three consecutive pulls separated by 5-s pauses between each pull. We calculated the absolute grip strength (in grams) as the average of the peak forces recorded from the three pulls. The investigators were blinded to treatment of subjects.

Muscle function. *Ex vivo* contractility of the extensor digitorum longus (EDL) muscles was determined as previously described[10,44]. EDL were dissected from the hind limbs and stainless-steel hooks were tied to the tendons of the muscles using 4-0 silk sutures and the muscles were mounted between a force transducer (Aurora Scientific, Aurora, ON, Canada) and an adjustable hook. The muscles were immersed in a stimulation chamber containing O_2/CO_2 (95/5%) bubbled Tyrode solution (121 mM NaCl, 5.0 mM KCl, 1.8 mM $CaCl_2$, 0.5 mM $MgCl_2$, 0.4 mM NaH_2PO_4, 24 mM $NaHCO_3$, 0.1 mM EDTA, 5.5 mM glucose). The muscle was stimulated to contract using a supramaximal stimulus between two platinum electrodes. Data was collected via Dynamic Muscle Control/Data Acquisition (DMC) and Dynamic Muscle Control Data Analysis (DMA) programs (Aurora Scientific). At the start of each experiment the muscle length was adjusted to yield the maximum force. The force-frequency relationships were determined by triggering contraction using incremental stimulation frequencies (0.5-ms pulses at 1–150 Hz for 350 ms at supramaximal voltage). Between stimulations the muscle was allowed to rest for 3 min. At the end of the force measurement, the length (L_0) and weight of the muscle were measured and the muscle was snap frozen in liquid N_2. To quantify the specific force, the absolute force was normalized to the muscle size, specifically the cross-sectional area, calculated as the muscle weight divided by the length using a muscle density constant of 1.056 kg/m^3 (ref. 45). The investigators were blinded to treatment of subjects.

Calcium imaging in muscle fibers. Single flexor digitorum brevis (FDB) fibers were isolated by enzymatic dissociation as previously described[46]. FDB muscles from the hind limb were incubated for 2 h at 37 °C in Dulbecco's Modified Eagles Medium (DMEM) containing 0.3% collagenase 1 (Sigma) and 10% FBS. The muscles were transferred to fresh DMEM and gently triturated using a 1,000 µl pipette until the muscles were dissociated. The cell suspension was stored in an incubator at 37 °C and 5% CO_2 until the start of the experiment. FDB fibers were loaded with the fluorescent Ca^{2+} indicator Fluo-4 AM (5 µM, Invitrogen/Molecular probes) for 15 min in room temperature (RT). The cells were allowed to attach to a laminin-coated glass cover slip that formed the bottom of a perfusion chamber. The cells were then superfused with tyrode solution (121 mM NaCl, 5.0 mM KCl, 1.8 mM $CaCl_2$, 0.5 mM $MgCl_2$, 0.4 mM NaH_2PO_4, 24 mM $NaHCO_3$, 0.1 mM EDTA, 5.5 mM glucose) bubbled with O_2/CO_2 (95/5%). The fibers were triggered to tetanic contraction using electrical field stimulation (pulses of 0.5 ms at supra-threshold voltage, at 70 Hz for 350 ms) and Fluo-4 fluorescence was monitored using confocal microscopy (Zeiss LSM 5 Live, 40× oil immersion lens, excitation wavelength was 488 nm and the emitted fluorescence was recorded between 495 nm and 525 nm) in line-scan mode. Only cells that were firmly attached to the glass bottom dish throughout the tetanic stimulation were included in the analysis. After subtraction of background fluorescence, the change in fluorescent signal during the tetanus (peak–resting (ΔF)) was divided by the resting signal ($\Delta F/F_0$). All experiments were performed at RT (approximately 20 °C).

Alternatively, basal Ca^{2+} was measured simultaneously with tetanic Ca^{2+}, using ratiometric imaging with Fluo-4 (excited at 488 nm and emission collected at 505–530 nm) and Fura-red (Invitrogen/Molecular probes, excited at 488 nm and emission collected at >650 nm) imaging in cells ($F_{650\ nm}/F_{515\ nm}$). For this method basal Ca^{2+} concentration is shown with tetanic Ca^{2+} concentration. The investigators were blinded to treatment of subjects.

Proteomics. Skeletal muscle samples (tibialis anterior) were solubilized by ground glass homogenization and brief sonication in lysis buffer (8 M urea, 10 mM DTT solution freshly prepared). The homogenates were centrifuged at 150,000*g* for 20 min at 4 °C to remove insoluble materials. Protein concentration was determined by the Bradford Protein Assay. Protein reduction, alkylation and tryptic digestion were carried out using a conventional method previously published[47]. The proteolyzed protein samples were injected onto a C18 reversed-phase column and analyzed using a Thermo-Finnigan linear ion-trap (LTQ) mass spectrometer coupled with a Surveyor autosampler and a MS-HPLC system (Thermo-Finnigan). The acquired data were searched against the UniProt mouse protein sequence database containing 55,191 protein sequences (released on April 18, 2012) using SEQUEST (v. 28 rev. 12) algorithms in Bioworks (v. 3.3). Differential and post-translational modification on cysteine of +29 a.m.u. was included to identify the site of nitrosylation (C-NO) or oxidation (C-O3H). Identified peptides and proteins and their modification were validated by PeptideProphet, and ProteinProphet, in the Trans-Proteomic Pipeline (TPP, v. 3.3.0) (http://tools.proteomecenter.org/software.php)[48,49]. Only proteins with probability ≥ 0.9000 and peptides with probability ≥ 0.8000 were reported. Protein quantification was performed using IdentiQuantXL software as described[50].

Measurement of protein oxidation and ROS production. To determine channel oxidation the carbonyl groups on the protein side chains were derivatized to 2,4-dinitrophenylhydrazone (DNP-hydrazone) by reaction with 2,4-dinitrophenylhydrazine (DNPH) (Oxyblot, Millipore, Darmstadt, Germany). The DNP signal on RyR1 was detected by immunoblotting with an antibody specific to DNP (Millipore, Darmstadt, Germany). Protein carbonyl concentration in tissue lysates was determined using the OxiSelect Protein Carbonyl ELISA Kit (Cell BioLabs, Inc., San Diego, CA). Briefly, 0.5 mg of EDL lysate was added to a 96-well protein-binding plate, which was incubated overnight at 4 °C. After washing the plate three times with PBS, the protein carbonyl groups were derivatized with DNPH for 45 min at room temperature (in the dark). Plates were developed with a DNP-specific antibody followed by a HRP-conjugated secondary antibody. Protein carbonyl concentration was determined by comparison with a standard curve of oxidized BSA. ROS production was determined in C2C12 myotubes using the OxiSelect *in vitro* ROS/RNS Assay kit (Cell BioLabs, Inc.). ROS production was measured using 0.25 mg of cell lysate according to the manufacturer's recommendations. For H_2O_2-treated cells, cells were incubated with 1 mM H_2O_2 for 30 min before lysis. The investigators were blinded to treatment of subjects.

RyR1 immunoprecipitation and immunoblotting. RyR1 oxidation and nitrosylation and calstabin1 binding was determined as previously described[10]. Extensor digitorum longus (EDL) muscles were isotonically lysed in 0.5 ml of a buffer containing 50 mM Tris-HCl (pH 7.4), 150 mM NaCl, 20 mM NaF, 1.0 mM Na_3VO_4, and protease inhibitors. C2C12 cells were lysed in NP-40 lysis buffer containing 50 mM Tris-HCl (pH 8.0) 150 mM NaCl, 1.0% NP-40 and protease inhibitors. An anti-RyR antibody (4 µg anti-RyR1 antibody 5029 (ref. 10), a custom antibody against the last nine amino acids (CRKQYEDQLS; a cysteine was added at the N terminus) of the rabbit skeletal muscle RyR1) was used to immunoprecipitate RyR1 from 250 µg of tissue homogenate. Samples were incubated with antibody in 0.75 ml of a modified RIPA buffer (50 mM Tris–HCl pH 7.4, 0.9% NaCl, 5.0 mM NaF, 1.0 mM Na_3VO_4, 1% Triton-X100 and protease inhibitors) for 1 h at 4 °C. The immune complexes were incubated with protein A–sepharose beads (Sigma) overnight at 4 °C and the beads were washed twice with modified RIPA buffer. Proteins were separated on 4–12% Bis-Tris gels (Life Technologies) and transferred to nitrocellulose for 1 h at 100 V (Bio-Rad, Hercules, CA). After incubation with blocking solution to prevent nonspecific antibody binding, immunoblots were developed with anti-RyR (Affinity Bioreagents, cat. MA3-916, Golden, CO; 1:2,000) and anti-Cys-NO antibody (Sigma, cat. N0409, St. Louis, MO; 1:2,000) or an anti-calstabin antibody (Santa Cruz Biotechnology, cat. sc-6173, Santa Cruz, CA; 1:2,500). Immunoblots were developed and quantified using the Odyssey Infrared Imaging System (LICOR Biosystems, Lincoln, NE) and infrared-labeled secondary antibodies. Detection of pSMAD3, SMAD3, Nox4 (Abcam, Cambridge, UK; 1:1,000 each), GAPDH and tubulin (Sigma; 1:500 each) from mouse muscle, human biopsies and C2C12 cells was via lysis in NP-40 buffer and detection and quantification of immobilized proteins either using the Odyssey Infrared Imaging System or GE ImageQuant LAS4000 Imaging System (GE Healthcare Bio-sciences, Pittsburgh, PA). The investigators were blinded to treatment of subjects.

Human samples. Muscle biopsies from humans with breast and lung cancer and non-oncologic controls were obtained with consent under a research exempt waiver (IRB# 1403849213) approved by the institutional review board (IRB)

doi:10.1038/nm.3961

of Indiana University School of Medicine from the clinical research laboratory of P. Picci at the Istituto Ortopedico Rizzoli, Bologna, Italy. Control muscle samples were from humans with non–cancer-related musculoskeletal conditions. Humans with breast and lung cancer all had bone metastases and had not received chemotherapy at the time of tissue collection. Of the breast cancer patients, one also had lung metastases and one had tumor cells in the thyroid. Of the lung cancer patients, one also had cancer in the lymph nodes. This study was conducted under protocol approval from the IRB of Indiana University School of Medicine.

Drug treatments. All drug treatments were initiated 48 h before tumor cell inoculation with the exception of Rycal S107, which was initiated at the time of tumor cell inoculation.

SD-208. As described, SD-208 is a specific inhibitor of the TGF-β type I receptor[51]. SD-208 (60 mg/kg/d) or vehicle (1% methylcellulose) was administered by daily gavage and continued daily for the duration of each study.

Zoledronic acid. Zoledronic acid (ZA), an anti-resorptive bisphosphonate with FDA approval for use in humans with bone metastases, or vehicle (PBS) was administered by subcutaneous injection (5 μg/kg) three times per week for the duration of each study.

TGF-β–specific antibody. Antibody clone 1D11.16.8 (1D11) is a neutralizing antibody to all three subtypes of TGF-β (TGF-β1, TGF-β2 and TGF-β3). 1D11 (10 mg/kg) or isotype control (MOPC-21; 10 mg/kg) was administered by intraperitoneal injection three times per week for the duration of each study[24].

Rycal (S107). S107 is a benzothiazepine derivative that binds the RyR1 channel and enhances the binding affinity of calstabin1 (ref. 13). S107 was administered via osmotic infusion pump (Azlet) for continuous delivery. The mini-pump was implanted subcutaneously and the opening sutured and glued. Wounds were monitored for healing.

Nox4 inhibitor (GKT137831). GKT137831 (60 mg/kg/day) or vehicle (1.2% methylcellulose + 0.1% Polysorbate 80) was administered by daily gavage for the duration of the study.

Single-channel measurements. Muscles were homogenized using a Tissuemizer (Fisher Scientific) at the highest speed for 1 min with 2 volumes of: 20 mM Tris-maleate (pH 7.4), 1 mM EDTA and protease inhibitors (Roche). Homogenate was centrifuged at 4,000*g* for 15 min at 4 °C and the supernatant was centrifuged at 40,000*g* for 30 min at 4 °C. The final pellet, containing the SR fractions, was resuspended and aliquoted in 250 mM sucrose, 10 mM MOPS (pH 7.4), 1 mM EDTA and protease inhibitors. Samples were frozen in liquid nitrogen and stored at –80 °C. SR vesicles containing RyR1 were fused to planar lipid bilayers formed by painting a lipid mixture of phosphatidylethanolamine and phosphatidylcholine (Avanti Polar Lipids, Alabaster, AL) in a 3:1 ratio in decane across a 200-μm hole in polysulfonate cups (Warner Instruments, Hamden, CT) separating two chambers. The *trans* chamber (1.0 ml), representing the intra-SR (luminal) compartment, was connected to the head stage input of a bilayer voltage clamp amplifier. The *cis* chamber (1.0 ml), representing the cytoplasmic compartment, was held at virtual ground. Symmetrical solutions used were as follows: 1 mM EGTA, 250 mM HEPES, 125 mM Tris-HCl, 50 mM KCl, 0.64 mM $CaCl_2$ (pH 7.35) as *cis* solution and 53 mM $Ca(OH)_2$, 50 mM KCl, 250 mM HEPES (pH 7.35) as *trans* solution. The concentration of free Ca^{2+} in the *cis* chamber was calculated with WinMaxC program (version 2.50; http://www.stanford.edu/~cpatton/maxc.html). SR vesicles were added to the *cis* side and fusion with the lipid bilayer was induced by making the *cis* side hyperosmotic by the addition of 400–500 mM KCl. After the appearance of potassium and chloride channels, the *cis* side was perfused with the *cis* solution. Single-channel currents were recorded at 0 mV by using a Bilayer Clamp BC-525C (Warner Instruments), filtered at 1 kHz using a Low-Pass Bessel Filter 8 Pole (Warner Instruments) and digitized at 4 kHz. All experiments were performed at room temperature (23 °C). Data acquisition was performed by using Digidata 1322A and Axoscope 10.1 software (Axon Instruments, Sunnyvale, CA). The recordings were analyzed by using Clampfit 10.1 (Molecular Devices, Sunnyvale, CA) and Origin software (ver. 6.0, Microcal Software). The investigators were blinded to the genotype, age and treatment of the groups. Single-channel currents were measured at 150 nM cytosolic [Ca^{2+}] using Ca^{2+} as a charge carrier at 0 mV. Channel openings are shown as upward deflections; the closed (c-) state of the channel is indicated by horizontal bars in the beginning of each trace. P_o, open probability; T_o, average open time; T_c, average closed time. The activity of the channel, indicated by the thick black bar, is shown on the expanded time scale. The investigators were blinded to treatment of subjects.

SERCA activity. SERCA activity was measured using the malachite green procedure for phosphate determination, adapted to the microscale as previously described[52]. The reaction was started by the addition of 50 μg of EDL microsomes to 150 μl of reaction mixture (20 mM MOPS, Tris-HCl, pH 6.8, 100 mM KCl, 5 mM $MgCl_2$, 5 mM ATP, 1 mM EGTA, 0.350 mM $CaCl_2$ (free Ca^{2+} concentration of approximately 500 nM as calculated using the CHELATOR program). After 5 min, the reaction was stopped by the transfer of 120 μl of reaction mixture to 80 μl of malachite green reagent mixture in a 96-well microplate. The malachite green reagent mixture was made by mixing 0.122% malachite green hydrochloride in 6.2 N H_2SO_4, 5.76% ammonium paramolybdate tetrahydrate and 11% Tween-20 in a volume ratio of 100:66:2. Color development was quenched after 10 s by the addition of 45 μl of 15.1% sodium citrate dihydrate. Inorganic phosphate liberated in the ATPase reaction was quantified by comparison of absorbance at 570 nm with standard curves generated with known amounts of Na_2HPO_4 in the reaction buffer. The investigators were blinded to treatment of subjects.

Enzyme-linked immunosorbent assay (ELISA). ELISA assay for TGF-β quantification from mouse serum was performed using Quantikine human TGF-β1 (R&D Systems; Minneapolis, MN; USA) according to manufacturer's guidelines. Serum samples were diluted 1:20. ELISA plates were analyzed by absorbance reading using a microplate reader set to 450 nm with wavelength correction set to 540 nm. Investigators were blinded to sample identity.

Caloric restriction. Caloric restriction was determined by measuring food intake by mice with MDA-MB-231 breast cancer bone metastases as an average amount of food in grams (calculated by per cage basis; $n = 5$ mice per cage). Food was restricted to healthy animals ($n = 10$ per group; strain, age and sex matched to bone metastasis model) for 1 week following 3 weeks of *ad libitum* feeding to maintain consistency with previous animal studies. Calculated feedings (30–40% reduction of normal intact) and body weight measurements were completed at the same time each day. The investigators were blinded to treatment of subjects.

Calcium sparks measurements. C2C12 cells were incubated in a relaxing solution (140 mM potassium glutamate, 10 mM HEPES, 10 mM $MgCl_2$, 0.1 mM EGTA, pH 7.0). Cells were permeabilized in relaxing solution containing 0.01% saponin for ~30 s. After washing the sample with a saponin-free solution, the solution was changed to an internal medium (140 mM potassium glutamate, 5 mM Na_2ATP, 10 mM glucose, 10 mM HEPES, 4.4 mM $MgCl_2$, 1.1 mM EGTA, 0.3 mM $CaCl_2$, Fluo-3 (pentapotassium salt, Invitrogen/Molecular probes, pH 7.0)) for Ca^{2+} sparks acquisition as previously reported[13]. Fluorescence images were acquired with a Zeiss LSM 5 Live confocal system (63× oil immersion, NA = 1.4) operated in line-scan mode (x versus t, 1.5 ms/line, 3,000 lines per scan) along the longitudinal axis of the fibers. Each location was scanned at most twice before moving the line location. Fluo-3 was excited with an Argon laser at 488 nm, and the emitted fluorescence was recorded between 495 and 555 nm. Image analysis was performed using custom made routines compiled in IDL (v7.1, ITT). Potential Ca^{2+} spark areas were empirically identified using an autodetection algorithm[53]. The mean F value for the image was calculated by summing and averaging the temporal F at each spatial location while ignoring potential spark areas. This F value was then used to create a F/F image pixel by pixel. Statistical comparisons were performed using the ANOVA test with a significance level set at $P < 0.05$. The investigators were blinded to the treatment of subjects.

Semi-quantitative RT-PCR. Tibialis anterior (TA) muscle was lysed by Dounce homogenization in Trizol (Invitrogen) for RNA extraction. One-fifth volume of chloroform was added to the lysates, which were then vortexed vigorously for 15 s and incubated at room temperature for 3 min. Samples were centrifuged (12,000*g*, 15 min, 4 °C) and the upper aqueous phase was collected and loaded

onto a GenElute mammalian total RNA mini column (Sigma). Total RNA was isolated according to the manufacturer's instructions. DNase I treatment was performed to remove genomic DNA contamination (Qiagen), and RNA integrity was assessed on agarose gels. RNA (500 ng per sample) was reverse-transcribed using Superscript II (Invitrogen) according to the manufacturer's instructions with anchored oligo(dT) (Promega) for priming. The resulting cDNAs were prepared for semiquantitative real-time PCR using HotStart-IT SYBR Green PCR Kit (Affymetrix) and analyzed in a CFX96 Real-Time PCR Detection System (BioRad) for 40 cycles (95 °C for 15 s, 58 °C 30 s, 72 °C for 30 s) after an initial 2 min incubation at 95 °C. Primers were optimized for real-time PCR (amplification efficiency 100 ± 5%). Target gene expression (*Nox1*, *Nox2* and *Nox4*) was normalized against the housekeeping gene β2-microglobulin (*B2m*), and data were analyzed using the ΔΔ*Ct* method.

Primers: *B2m* forward: 5′-CTGACCGGCCTGTATGCTAT-3′; *B2m* reverse 5′-CAGTCTCAGTGGGGGTGAAT-3′; *Nox1* forward 5′-AATGCCCA GGATCGAGGT-3′; *Nox1* reverse 5′-GATGGAAGCAAAGGGAGTGA-3′; *Nox2* forward 5′-CCCTTTGGTACAGCCAGTGAAGAT-3′; *Nox2* reverse 5′-CAATC CCGGCTCCCACTAACATCA-3′; *Nox4* forward 5′-GGATCACAGAAGGT CCCTAGCAG-3′; *Nox4* reverse 5′-GCGGCTACATGCACACCTGAGAA-3′.

Statistical analyses. The data are presented as mean ± s.e.m. The group size for *in vivo* experiments was determined by power analyses using previous muscle-specific force data to achieve statistical significance with the fewest mice. The mean difference in muscle-specific force in mice with breast cancer versus non-tumor was 42% (275 kN/m^2 versus 390 kN/m^2; s.d. = 64; **Fig. 1b**). Assuming α error rate = 0.05 and β = 0.20 and a conservative 30% mean difference (275 to 360), the minimum number of animals per group is $n = 10$. Differences among experimental groups were analyzed by *t*-tests or analysis of variance (ANOVA) with appropriate post hoc and multiple comparison tests. For single-timepoint measures of any sample size, a two-sided Student's *t*-test was used[54]. When more than two groups were compared simultaneously, analysis of variance (ANOVA) followed by Tukey's post hoc tests were used (e.g., comparison between control, tumor bearing and tumor bearing + S107 groups). In some experiments measurements in a group were repeated over time (e.g., forelimb grip). These experiments were analyzed by repeated measures ANOVA followed by Tukey's post hoc tests. *P* values less than 0.05 were considered significant ($^*P < 0.05$; $^{**}P < 0.01$; $^{***}P < 0.0005$; $^{****}P < 0.0001$). Statistical analyses were performed with Prism 6.0 software (GraphPad Prism, La Jolla, CA). Samples for semi-quantitative RT-PCR were analyzed with a minimum of three biological replicates. Samples for western blotting and RT-PCR were analyzed in biological triplicate (minimum). All sample sizes reported in study are minimum values. Assumptions for ANOVA analyses were met (i.e., normal distribution) with the exception of data in **Figures 1c**, **2e**, **4f** and **5a**,**b**. For these analyses, we used a nonparametric (Kruskal-Wallis) ANOVA and Dunn's multiple comparisons. Variation between groups being compared was not measured due to variability in tumor progression in mice. Exclusion plan: EDL specific force data was excluded in cases in which there was evidence of damage to the muscle fibers. Forelimb grip strength data was excluded when there was evidence of forearm bone lesions as pain is likely to have a role in forelimb grip strength and animal compliance. This exclusion plan was pre-established. Female athymic nude mice obtained from Harlan and female CB.17 SCID mice obtained from Charles River were randomized into groups upon arrival. All statistical tests use biological replicates and are indicated by group size (n) in figure legends. Investigators were blinded to the identity of subjects.

37. Wehrens, X.H. *et al.* Protection from cardiac arrhythmia through ryanodine receptor-stabilizing protein calstabin2. *Science* **304**, 292–296 (2004).
38. Dunn, L.K. *et al.* Hypoxia and TGF-β drive breast cancer bone metastases through parallel signaling pathways in tumor cells and the bone microenvironment. *PLoS ONE* **4**, e6896 (2009).
39. Soule, H.D., Vazguez, J., Long, A., Albert, S. & Brennan, M. A human cell line from a pleural effusion derived from a breast carcinoma. *J. Natl. Cancer Inst.* **51**, 1409–1416 (1973).
40. Yin, J.J. *et al.* A causal role for endothelin-1 in the pathogenesis of osteoblastic bone metastases. *Proc. Natl. Acad. Sci. USA* **100**, 10954–10959 (2003).
41. Hu, Z. *et al.* Systemic delivery of oncolytic adenoviruses targeting transforming growth factor-β inhibits established bone metastasis in a prostate cancer mouse model. *Hum. Gene Ther.* **23**, 871–882 (2012).
42. Johnson, R.W. *et al.* Wnt signaling induces gene expression of factors associated with bone destruction in lung and breast cancer. *Clin. Exp. Metastasis* **31**, 945–959 (2014).
43. Jackson, N. *et al.* Two new IgA1-κ plasma cell leukaemia cell lines (JJN-1 & JJN-2) which proliferate in response to B cell stimulatory factor 2. *Clin. Exp. Immunol.* **75**, 93–99 (1989).
44. Bonetto, A., Andersson, D.C. & Waning, D.L. Assessment of muscle mass and strength in mice. *Bonekey Rep.* **4**, 732 (2015).
45. Yamada, T. *et al.* Impaired myofibrillar function in the soleus muscle of mice with collagen-induced arthritis. *Arthritis Rheum.* **60**, 3280–3289 (2009).
46. Aydin, J. *et al.* Increased mitochondrial Ca^{2+} and decreased sarcoplasmic reticulum Ca^{2+} in mitochondrial myopathy. *Hum. Mol. Genet.* **18**, 278–288 (2009).
47. Lai, X. *et al.* Characterization of the renal cyst fluid proteome in autosomal dominant polycystic kidney disease (ADPKD) patients. *Proteomics Clin. Appl.* **2**, 1140–1152 (2008).
48. Keller, A., Nesvizhskii, A.I., Kolker, E. & Aebersold, R. Empirical statistical model to estimate the accuracy of peptide identifications made by MS/MS and database search. *Anal. Chem.* **74**, 5383–5392 (2002).
49. Nesvizhskii, A.I., Keller, A., Kolker, E. & Aebersold, R. A statistical model for identifying proteins by tandem mass spectrometry. *Anal. Chem.* **75**, 4646–4658 (2003).
50. Lai, X., Wang, L., Tang, H. & Witzmann, F.A. A novel alignment method and multiple filters for exclusion of unqualified peptides to enhance label-free quantification using peptide intensity in LC-MS/MS. *J. Proteome Res.* **10**, 4799–4812 (2011).
51. Mohammad, K.S. *et al.* Pharmacologic inhibition of the TGF-β type I receptor kinase has anabolic and anti-catabolic effects on bone. *PLoS ONE* **4**, e5275 (2009).
52. Kimura, Y., Kurzydlowski, K., Tada, M. & MacLennan, D.H. Phospholamban regulates the Ca^{2+}-ATPase through intramembrane interactions. *J. Biol. Chem.* **271**, 21726–21731 (1996).
53. Cheng, H. *et al.* Amplitude distribution of calcium sparks in confocal images: theory and studies with an automatic detection method. *Biophys. J.* **76**, 606–617 (1999).
54. de Winter, J.C.F. Using the Student's *t*-test with extremely small sample sizes. *Pract. Assess., Res. Eval.* **18**, 1–12 (2013).